UNIVERSITY OF CALIFORNIA
RIVERSIDE

Intracellular Delivery of Exogenous Molecules Via an Ultrahigh Throughput Mechanoporation Microdevice

A Dissertation submitted in partial satisfaction
of the requirements for the degree of

Doctor of Philosophy

in

Bioengineering

by

Harish Girish Dixit

September 2018

Dissertation Committee:
Dr. Masaru P. Rao, Chairperson
Dr. Hideaki Tsutsui
Dr. William Grover

The Dissertation of Harish Girish Dixit is approved:

_____

_____

_____

Committee Chairperson

University of California, Riverside

ACKNOWLEDGEMENTS

First and foremost, I would like to thank my advisor, Dr. Masaru P. Rao, for his guidance and support throughout my tenure as a graduate student researcher. Your constant willingness to discuss new ideas, results, and questions that I've had during the development of my research has been invaluable and has made me into an independent and strong engineer. I don't think I would be half the person I am today were it not for your guidance and patience whenever I dropped into your office to talk about anything project related that was on my mind.

I would like to thank Dr. Tsutsui, not only for his participation as a member of my dissertation defense committee, but also as an ever-present source of advice in regard to my research project. Our meetings throughout the years always gave me fresh perspectives when tackling problems during my experiments and allowed me to become a detail-oriented and thorough engineer. The use of your laboratory and its resources during the formative years of the UHT mechanoporation project were critical and I firmly believe that this device would not be where it is today being it not for those early experiments in Bourns B156. I would also thank Dr. Grover for his participation as a committee member along with his insightful ideas regarding future device development.

As most everyone will attest, a Ph.D. is one of the most grueling and challenging times of a student's life. I was lucky enough to be blessed with some of the most caring lab mates a graduate student could ask for in the biomedical microdevices laboratory (BML). Shannon Gott, Omid Khandan, Ryan Peck, Duncan Ashby, Bryan Woo, Samantha Corber,

your friendship over these years helped to keep me sane during the days where I felt lowest. I look back on our shared meals, rock-climbing adventures, movie premieres, and Labsgivings with such fondness because I know that without them, my successes during the Ph.D. would have numbered far fewer.

City of Hope, specifically Dr. Stephen J. Forman's T-Cell Therapeutics Research Laboratory (TCTRL), was the location where my project flowered to its fullest potential. I want to extend my sincerest gratitude to the entire lab for welcoming me, allowing me to use your resources to accomplish my objectives, and for making me feel as if I truly belonged there. Thank you specifically to Renate Starr and Cindy Yang, who would graciously set aside time from their very busy schedules to work with me whenever I experienced problems with my project. Your enthusiasm and altruistic natures made this collaboration between BML and TCTRL a success.

Without the skill and knowledge of the individuals working at the facilities in UCR, UCI, UCSB, and City of Hope, my research would never have even begun. Thank you to the UC Riverside Machine Shop (Robert J. Wright), the Center for Nanoscale Science and Engineering – UC Riverside (Dr. Dong Yan, Dexter Humphrey, Mark Heiden), the Integrated Nanosystems Research Facility – UC Irvine (Vu Phan, Jake Hes), Nanotech – UC Santa Barbara (Tom Reynolds), and the Microscope Core – City of Hope (Loren Quintanar, Dr. Brian Armstrong) for making the UHT mechanoporation device a reality.

Finally, I would like to thank my family. Words cannot begin to describe the feelings of gratitude I hold for my parents, who made every single opportunity for me possible. The Ph.D., and everything else prior to it would merely have been an abstract

concept were it not for the efforts put forth by my father, Girish A. Dixit and mother, Sarojini G. Dixit to allow me to focus solely on my education and in so doing, create a bright future for myself. I hope that the years which follow the completion of this doctorate allow me to demonstrate the respect and appreciation I hold for these two people. Such gratitude also extends to my wife, Payal Dixit. I firmly believe that everything happens for a reason. I knew when I started at UCR, that I was here to accomplish a lofty goal of attaining a doctorate in Bioengineering. What I didn't know is that I was also meant to be here so that I would meet you. You are my anchor and have been the single constant during this challenging time of my life. Payal, you have always been exactly what I've needed every day since I met you, and without your love and support, this Ph.D. would never have been possible. Thank you, for helping me achieve my dream.

DEDICATION

I dedicate this work to:

My Master, my guiding North Star who never lead me astray.

My parents, my compass and telescope who helped keep my bearings in unknown waters.

My wife, my first mate and constant companion through calm seas and turmoiled storms.

ABSTRACT OF THE DISSERTATION

Intracellular Delivery of Exogenous Molecules Via an Ultrahigh Throughput Mechanoporation Microdevice

by

Harish Girish Dixit

Doctor of Philosophy, Graduate Program in Bioengineering
University of California, Riverside, September 2018
Dr. Masaru P. Rao, Chairperson

Cancer immunotherapies using adoptive cell transfer (ACT) train a patient's immune system to fight against cancer. This growing field of research has demonstrated promising results as an alternative treatment to current therapies, such as chemotherapy or radiation. However, the methods used to genetically engineer the anti-cancer functionalities into the required cell types (T lymphocytes), such as viral vector transduction, possess certain drawbacks that limit them in scalability, automation, and cost. There is a critical need for the development of a new cell modification strategy that addresses these shortcomings. We have looked towards the application of non-biological delivery methods as a potential means of addressing these limitations, namely microinjection.

Microinjection physically creates a transient membrane pore for the delivery of exogenous payloads. The gold standard of this technology consists of a human operator

porating and injecting an exogenous payload through a linear "one-cell-at-a-time" scheme. This results in throughputs of ~3 cells/min, a rate that cannot feasibly produce the required number of treated cells for immunotherapies at an appreciable time scale. Thus, though this method has the advantage of safety and precision, it requires significant improvement to be competitive against current techniques for T-cell genetic modification.

We outline preliminary efforts to develop a new form of microinjection using silicon microfabrication. To simplify fabrication procedures, and demonstrate a proof-of-concept technology, we have created a device for ultrahigh (UHT) cellular manipulation via mechanical membrane poration, i.e. UHT mechanoporation. Such a device represents an interim step towards our microinjection concept.

The fundamental nature of the device stems from a microelectromechanical systems (MEMS) functional core composed of cell capture sites with monolithically integrated, sub-micrometer scale solid penetrators. Negative flow through aspiration vias at the bottom of the capture sites pulls cells onto the penetrators thus causing membrane poration. Cells are then released by reversing flow through the aspiration vias. The transient nature of membrane disruption enables transfection via diffusion-driven influx of exogenous molecules from the surrounding suspension, while massive parallelization provides for UHT operation (e.g. 10k capture sites in the current device).

We report successful fabrication of a first-generation UHT mechanoporation device capable of multiplexed cell manipulation. However, the preliminary studies reported by our collaborators indicated low cell delivery efficiencies (8%). We discuss our efforts to further optimize the operational parameters associated with our mechanoporation device.

Through detailed device characterization, and implementation of precise, high-resolution experimental techniques, we have increased our device efficiencies by 10-fold. The delivery efficiencies for recovered, treated cells at the 30-minute time point and 12-hour time point were 90% and 97% respectively. Our overall device yields were 96% at the 12-hour time point, far higher than those reported by competing techniques, such as electroporation.

The results from our optimization studies demonstrate effective molecular delivery to cells using the UHT mechanoporation device. They indicate high delivery efficiencies across our parameter window. However, we observed a low efficiency of cell recovery from the device. Our results thus identify directions for future development of the UHT mechanoporation device, and collectively demonstrate the feasibility of an active injection system that can address limitations in engineered T-cell production.

TABLE OF CONTENTS

LIST OF FIGURES

1. INTRODUCTION

1.1. Cancer and Current Methods of Treatment

Cancer is defined as the uncontrolled growth of cells, which can begin to affect the normal biological processes of a patient. These cells typically grow well beyond their own boundaries, and thus can spread to other regions of the body (metastasis).[1] A group of these rapidly growing cells is known as a tumor, which has the capability of becoming enervated and vascularized.[2] Tumors are a typical symptom of most cancers; however, in certain cases like leukemia, cancer cells flow freely through the bloodstream and do not form tumors.[2] Unlike most healthy cells, cancer cells lack specialization or any specified function. This characteristic arises from the unstoppable cell division inherent to these cells. Cancer cells are also able to bypass the common signals for ceasing of cell division, apoptosis, and the body's immune response.[2]

Typically, genetic mutations within a cell are the source of cancer. The WHO reports three primary categories associated with the deteriorative alterations to a patient's genome: physical carcinogens, chemical carcinogens, and biological carcinogens.[1] These carcinogens play a role in affecting the natural functions of proto-oncogenes, tumor suppressor genes, and DNA repair genes. Proto-oncogenes and tumor suppressor genes are involved in the control of cell proliferation and growth.[2] Mutations in these genes can lead to a loss in control of cell proliferation, resulting in the generation of cancerous cells. DNA repair genes are responsible for ensuring that the prevalence of mutations arising from damage to the patient's genome through the various forms of carcinogens is minimized.[2] These repair genes are subcategorized via three methods of repair: base excision repair (BER), nucleotide excision repair (NER), and mismatch repair (MMR).[3] Cells that contain

mutations within these genes are more likely to develop mutations in other regions of their genome. This compounding of mutations may drive the occurrence of cancer.

The WHO has reported that cancer is the second leading cause of death in the United States (~8.8 million deaths in 2015), with lung cancer representing the highest percentage of estimated deaths among all patients and prostate cancer representing the highest percentage of estimated new cases in 2018.[4] In addition, it is expected that the number of new cancer cases will increase by 70% over the next 20 years.[1] Globally ~17% of all deaths are from cancer. The WHO also reports an increasing economic impact from cancer with the calculated annual cost for treatment in 2010 to be $1.16 trillion in total.[1]

There are several methods of treatment available for cancer, the most common—and gold standards—being chemotherapy, radiation, surgery, and hormone therapy.[5] Chemotherapy uses a combination of various drug/chemical agents to destroy tumors in a patient. Such a treatment is non-specific and instead relies on the rapid division factor of cancer cells as the basis for targeting. In most cases, chemotherapeutic agents target the DNA replication/synthesis stage of dividing cells.[5] For example, a common chemotherapy agent, methotrexate, interferes with a cell's pathway of thymine production, a necessary nucleotide base for DNA synthesis.[6] As cancer cells divide much faster than normal cells, they have a higher need for the generation of thymine. Methotrexate competitively inhibits substrate binding of dihydrofolate to dihydrofolate reductase (DHFR). DHFR is responsible for activating folate, which is subsequently used in the synthesis of thymine. Because methotrexate now blocks the active site of DHFR, thymine production is halted. This leads to incorrect incorporation of bases during DNA synthesis, leading to cell death.[5]

Though chemotherapy is one of the standards for cancer treatments, it has several disadvantages. Firstly, cancer cells can often be immune to drugs that target their DNA synthesis pathways, such a methotrexate, reducing the effectiveness of this chemical. Secondly, chemotherapy has a slew of toxic side effects that can decrease the quality of life of the patient: hair loss, nausea, vomiting, anemia, infections, and immune system ablation to name a few. Thirdly, this treatment scheme is almost always used in conjunction with other therapies, most notably radiation, to cure the patient thus involving high treatment complexity.[5]

Radiation therapy uses a focused beam of radiation aimed at the location of the tumor to kill cancer cells. This therapy is second in effectiveness only to surgery and is limited by the location of the tumor within the patient, and the risk to any adjacent organs due to breakdown of the beam at the point of entry.[5] Radiation can be applied externally using a beam but can also be an implantable treatment wherein a radioactive object is placed within the tumor (i.e. brachytherapy). Surgery uses a physical means to remove the patient's tumor; however, is significantly limited by the location of the tumor and is not effective if the cancer has already metastasized. In addition, surgery involves a risk of leaving behind cancer cells if the tumor is nicked during extraction.[5] Hormone therapy involves manipulating the levels of certain hormones within the patient—either by surgical removal of hormone glands or drugs that inhibit hormone production—to slow the progress of tumor growth. By using this therapy to block trophic factors, the pathways that are responsible for regulating cell apoptosis are blocked. As such, the cancer cells are killed. However, over time tumor cells can become resistant to hormonal therapy.[5] In addition,

this treatment is limited to only differentiated cancer cells, and is ineffective against the stem cells that generate the tumor cells.

Recently, a great deal of research has gone into the development of technologies to address many of the limitations inherent in bulk therapies such as surgery, radiation therapy, and chemotherapy. As these treatments are non-specific the risk of adversely affecting healthy tissue within a cancer patient is high. Significant developments have been seen in the past decade that show how using antibodies, nanoparticles and a more sophisticated understanding of the biochemical pathways involved in cancer occurrence can be used to generate targeted therapies for tumor destruction.[7-9] These therapies typically involve the conjugation of an antibody or nanoparticle to an otherwise highly toxic chemotherapeutic agent to confer tumor-specific binding. However, the disadvantage still remains that these therapies rely on agents that only treat detectable tumors. A patient in remission may still possess the risk of re-exhibiting cancer at a later stage in life. With the mortality rate of cancer increasing, along with the economic cost associated with its treatment, a need exists to develop new treatments that can offer a more permanent solution for patients.

1.2. T-Cell Immunotherapy as a New Cancer Treatment

An increasingly effective, and promising strategy for cancer treatment is that of adoptive T-cell immunotherapy or adoptive cell therapy (ACT). This strategy uses the extraction and *ex vivo* expansion of a patient's T lymphocytes to target and battle an outbreak of cancer. More specifically, during this *ex vivo* expansion, these T-cells can be

stimulated to express antigen specificity, namely through one of many forms of genetic engineering.[10] In addition, a simpler method of T-cell therapy has arisen through the observation that when T-cells in melanoma patients encounter their complementary activating antigens on tumor cells, they lose their ability to migrate through the tumor.[11,12] Such a loss not only reduces their efficacy in battling the cancer, but also localizes them within the tumor mass itself. By excising the tumor from the patient, these tumor-infiltrating lymphocytes (TILs) can be expanded through dissociation and addition of the growth factor, interleukin-2 (IL-2).[11] Re-introduction of the expanded cells into the patient, along with temporary immune system ablation and administration of IL-2, has shown a prolonged destruction of tumor cells within patients exhibiting varied cancer histologies.[11,13-18] Such astounding results serve to indicate that adoptive cell transfer, may pose not only a potential treatment for cancer, but also a true "cure".

Though T-cells expanded *ex vivo* are quite effective at melanoma tumor eradication, it is noted that such eradication is not as apparent in other tumor histologies, despite presence of T-cells within the tumor itself. Through several studies, it has been shown that the presence of several external factors, many of which are immunosuppressive, inhibit the natural function of these T-cells.[19] Such factors include T-cell immunoglobulin and mucin domain-containing protein 3 (TIM3), lymphocyte activation gene 3 protein (LAG3), programmed cell death protein 1 (PD1), and cytotoxic T lymphocyte antigen 4 (CTLA4).[19,20] What is interesting to note is that once these T-cells are removed from the *in vivo* tumor environment, their activation and function becomes much more pronounced. By allowing the T-cells to expand in a non-tumor environment, any remaining cancerous

cells in the culture medium are rapidly destroyed by these cells. Such a phenomenon is explained by the fact that immunosuppressive factors, or immunosuppressive cell populations (i.e. myeloid-derived suppressor cells: MDSCs) are absent from this culture environment. Several studies have gone on to show that the immunosuppressive nature of a tumor's interior may significantly counteract the effectiveness of ACT, and that removal of these factors, such as MDSCs and endogenous cells activated by the same cytokines, leads to higher tumor eradication.[11,21-23] As a result, many researchers believe that a combination of ACT along with targeted therapies, which include immunodepletion may lead to higher efficiencies for this technique.

1.3. T-Cell Engineering for Cancer Immunity

Along with the "standard" technique of tumor excision and T-cell expansion, which only applies to patients exhibiting myeloma, engineering of T-cells to target tumor specific antigens has paved the way to the application of ACT across various cancer histologies. However, the difficulty of this technique lies in engineering T-cells to identify the appropriate antigen, as a means to reduce any risk associated with recognition of non-tumor cells.[11,24,25] Typically, the most unique antigens presented by a tumor are those that are translated from a mutated gene.

In general, T-cells recognize two forms of antigens: MHC class I (intracellular antigens) and MHC class II (extracellular antigens) molecules. An advantage inherent to MHC class I recognition is that these molecules are expressed in nearly every cell type. As a result, T-cells that target for MHC class I antigens specific to tumors could potentially

recognize several different forms of T-cells. However, neoplastic cells (i.e. cancerous cells) can downregulate MHC I expression, thus circumventing the T-cells in the therapy.[11] Alternatively, antigen presenting cells (APCs), are capable of presenting MHC II molecules as both class I and class II antigens, from the perspective of a T-cell. Consequently, engineering T-cells to recognize MHC class II molecules may prove to be a more effective form of ACT as opposed to MHC class I based treatment. There are 3 primary methods to generate antigen specific T-cells for ACT (figure 1.1): (a) Tumor specific T-cell receptors (TCRs) cloned from patients with good antitumor response, and engineered into the actual patient's T-cells; (b) Chimeric antigen receptors (CARs), which are expressed in the patient's T-cells; (c) Mice immunized with human tumor antigens allowing for human MHC I & II expression; the associated TCRs are cloned into human cells.[11] Of these three different strategies, CAR T-cell therapy may be the most effective due to its versatility in recognition. Chimeric antigen receptors possess the specificity similar to that of an antibody, and are not restricted to only MHC structures or presentation pathways.[26] The entire CAR is engineered to have a single-chain structure, part of which is fused to the intracellular region of a T-cell, and can also activate the cell.

1.4. Gene Transduction for Immunotherapies

In the process of generating T-cells for ACT, we can observe that one of the most challenging steps is in transducing the patient's T-cells with the necessary genes coding for specific tumor antigens. This genetic modification can be accomplished through several strategies, some of which include viral transduction, DNA electro-transfer, and sleeping

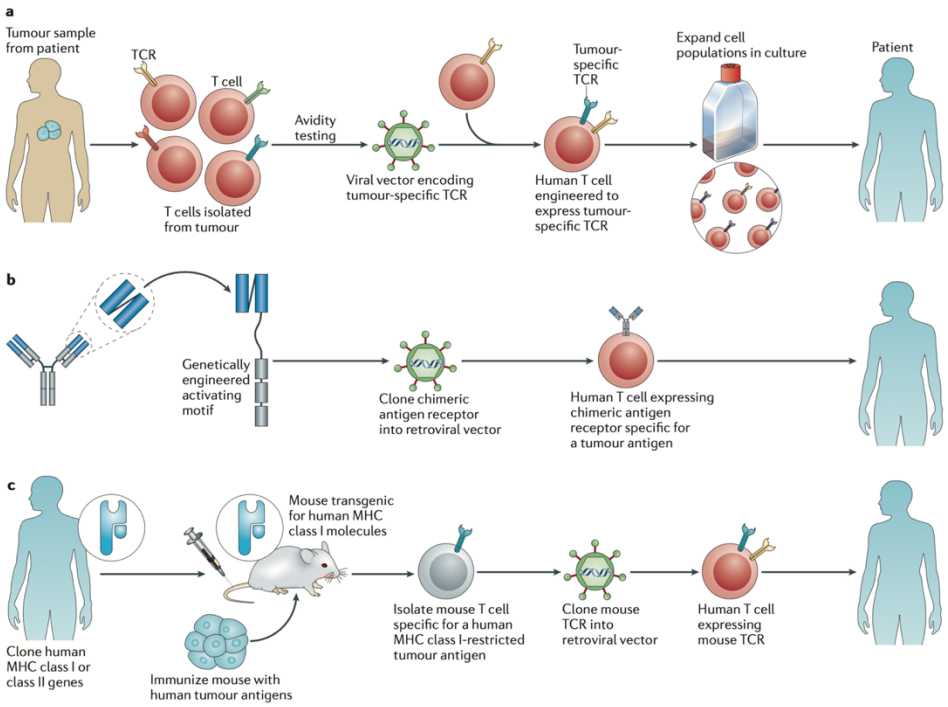

Figure 1.1. Visual representation of the various methods by which tumour-specific T-cells can be engineered. (a) T-cells with tumour specificity can be created by isolating tumour specific TCR genes from patients with particularly strong antitumour responses. Those genes are transduced into the patient's T-cell host genome and expanded. (b) Tumour specificity can also be created by transducing a coding sequence for a chimeric antigen receptor. This receptor does not require MHC class molecules for target recognition. (c) Finally, antitumour functionality can also be achieved through the application of mouse models. In this technique, TCRs from mice expressing human MHC complexes for tumours can be isolated and transduced into the patient's T-cells.[11]

beauty transposition.[10,26-29] Despite that many of these techniques currently act as the gold standard for ACT T-cell production, they do have their list of shortcomings. Viral transduction for example, is limited by production capacities, and scalability. In addition, it can become expensive to manufacture clinical-grade material and is highly dependent on the size of DNA that can be included in the vectors. Moreover, because viral vectors are not target specific when incorporating DNA into the host genome, this strategy poses the risk of insertional oncogenesis.[10,26] Similarly, DNA electro-transfer has been shown to be inefficient due to its inherent need for extended cell culture times, which can be destructive to cell activity and render the T-cells immunogenic.[27] In summary, though ACT has proven to be a promising treatment for cancer, its limitations in technicality of cell product manufacturing, scalability, and expense necessitates development of a new form of genetic modification that addresses these shortcomings.[30,31]

1.5. Non-Biological Methods of Intracellular Delivery

Concerns regarding the shortcomings of viral mediated gene delivery has motivated the development of non-biological transfection methods for engineered cell products and cellular manipulation applications.[27,30,31] Several methods exist to transiently generate pores within a plasma membrane. Understanding the various forms of cellular manipulation will give insight into how they can be applied to ACT.

Logically, the primary objective behind a compelling cell delivery system is reversible plasma membrane poration. This focus exists due to the inherent impermeability of a plasma membrane. An extensive number of techniques exist to achieve membrane

poration, and all exhibit 3 essential themes behind their delivery mechanisms. 1) There must be some form of cellular targeting, 2) the mechanism must achieve a reversible and transient poration of the cell's membrane while maintaining both viability and ample introduction of the delivery molecule, 3) the cells must be recaptured in order to examine system efficiency. In addition, one of the most important secondary objectives is high throughput, particularly one that exceeds that of the current gold standard.

Electroporation, sonoporation, and optoporation encompass most of the cell manipulation techniques focused on cell delivery. Electroporation, in its most classical sense, achieves cellular poration using short timed pulses of high voltage.[32] These pulses generate a transient electric field that is propagated through a conductive buffer in which the target cells are immersed. Once subjected to such fields, a number of pores are created within the cell's membrane, allowing for transfection of a delivery molecule (genes, drugs, proteins, etc.). In the past 2 decades, electroporation has been significantly optimized and developed into a commercially available technique for cellular poration.[32] Currently, efforts are being made to add a higher degree of precision and control on a single cell level, with a potential for high throughput.[33-36] Such advances in electroporation provide the benefit of higher cell viability as well as a better understanding behind the mechanics of membrane poration.

Classical sonoporation porates cells in a similar fashion to electroporation, however with the use of transient acoustic fields, as opposed to electric fields. The application of these acoustic fields normally leads to two unique outcomes depending on the energy of the acoustic field.[37] High intensity focused ultra sound (HIFU) leads to heating from

absorption of the acoustic energy by surrounding tissue (i.e. thermal effect). The non-thermal effect arises from the application of a low intensity acoustic field and manifests itself through radiation forces leading to mechanical streaming (enhancing transfection efficiencies of delivery molecules into a cells cytoplasm), or through the production of gaseous bubbles. Strategic placement and collapse of these gaseous bubbles can transiently porate the cellular membrane, allowing for passive delivery into the cell's cytosol.[37] By combining low acoustic fields with microfluidics, a recent study was able to further optimize sonoporation through precise control of microbubble nucleation, and cell positioning.[38]

A more recent, yet growing field of poration has been optoporation. This technique applies femto or nanosecond lasers to transiently disrupt a cell's membrane. Such disruption and eventual poration occurs from the generation of a low-density plasma on the cell's surface. These lasers can also be used to generate cavitation bubbles, which then collapse to achieve poration (similar to sonoporation techniques).[39,40] In addition to standalone poration systems, laser based manipulation devices have been applied in conjunction with electroporation as a means of better localizing electric fields for generation of membrane pores.[34] This method of combining multiple techniques of poration has also been achieved with sonoporation and electroporation. Application of orthogonal acoustic and electrical fields has resulted in higher transfection efficiencies and cellular viability when compared to stand alone sonoporation or electroporation methods.[35]

In addition to optical, electrical, and acoustic forms, there exist physical methods by which cells can be porated.[41-43] Recently, approaches based on mechanical poration (i.e.

mechanoporation) via shear-based deformation have shown considerable promise for non-viral transfection, because of the opportunities they provide for transfection without the need for external energy, thus allowing for a highly simplified cellular poration technique.[44,45] However, though these devices are currently one of the gold standards for high throughput cell delivery, they have exhibited low delivery efficiencies for an asynchronous population.[46]

Despite the breath of methodologies currently available for cellular delivery, there still exists a need for techniques that allow for deterministic, single site poration, with integrated ultrahigh throughput. Stochastic poration reliant on passive diffusion of payload leads to an unknown quantity of material being delivered and increases the risk of cellular damage due to the number of pores being created per cell. In addition, for most methods of mechanoporation, few studies have demonstrated realization of high throughput functionality, rather implying the capability of scaling the presented technology. We look towards solid penetrator methods to address many of the shortcomings inherent to engineered T-cell production.

1.6. Microinjection as a Concept for ACT, Current Gold Standard

When applied to gene delivery for CAR T-cell therapy, solid penetrator poration methods may simplify screening of novel constructs, antigen targets, and other molecules. This is due in part to their deterministic poration scheme, uniformity of delivery, cargo versatility, and controlled co-expression of multiple genes. Overall, this will allow for reduced *ex vivo* expansion times as well as increased antitumor efficacy for engineered T-

cells. With research indicating that proper design and optimized operational parameters can greatly reduce mechanical damage to cell membranes, there is great interest in creating the next leap forward in solid penetrator poration technology.[47]

Microinjection, the procedure of introducing exogenous material through a physically created pore in a cell's plasma membrane, may be the basis of such a solution to some of the difficulties associated with genetic modification for ACT. This technique offers a greater deal of delivery precision because it can accurately create only a single pore. By optimizing the delivery of the genes of choice (i.e. number of constructs, ratio of each construct), the expression of such constructs will be naturally optimized. Moreover, the innate nature of microinjection also lends uniformity of delivery across every cell in the population. In addition, because microinjection function is independent of payload— merely creating a direct pathway for intracellular delivery— we can take advantage of its cargo versatility. This will allow for controlled co-expression of multiple genes, and will simplify screening of novel constructs, antigen targets, and other molecules. Overall, microinjection's potential to increase transfection efficiency and uniformity for ACT T-cell production will allow for reduced *ex vivo* expansion time as well as increased antitumor efficacy.

Nonetheless, the gold standard for microinjection possesses its own shortcomings. Currently, this method relies on a trained human operator to manually capture, puncture, and inject cells in a serial format. While this provides opportunity for safely and precisely delivering a wide variety of materials into cells, even with extensive 6-month training most skilled operators are capable of only treating 3 cells/min. CAR T-cell production for

therapeutic purposes require more than 10^6 treated cells. As a result, in its current state microinjection is inadequate to efficiently produce engineered products for ACT.

Most poration technologies utilize microneedle-based injection for bulk delivery, but few systems exist to efficiently manipulate individual cells.[48] Recent efforts to automate the active injection process by replacing the operator with robotics have shown promise for improving success rates; however, this has come at the expense of instrument complexity.[49-52] Moreover, only modest gains in throughput have been achieved (≤35 cells/min). Complementary efforts have sought to use microelectromechanical systems (MEMS) fabrication techniques to create devices that improve injection reproducibility, or facilitate cell capture in ordered arrays for rapid identification and alignment.[49-51,53,54] However, many of these technologies are limited not only in function (i.e. cell capture only), but also throughput (i.e. a reliance upon serialized injection methodologies) and cell type (i.e. only adherent cells).[37,39,40,55-60]

We can conclude that currently, most efforts to optimize solid penetrator poration methods have not been able to consolidate high throughput with a scalable and efficient delivery system. Herein, we report the development of a new approach for cell manipulation that was first reported in 2012, and has now been further optimized to yield substantially higher device efficiencies compared to original data (Appendix A) and similar technologies over comparable time scales.[61] In addition, our current design is capable of treating suspended cells, a function mimicked by few other studies. Using an arrayed scheme and a Si-platform, this device is capable of bulk fabrication using existing microfabrication technologies, indicating the potential for cost-effective production.

Furthermore, due to our choice of material and the well-understood nature of the associated fabrication technology, we can reproduce devices with great accuracy, and tailor device design to the cell type of choice. Basic chip function stems from fluidic aspiration into single cell capture sites with central solid penetrators that concurrently puncture membranes as each cell settles into its respective site. Device efficiency is characterized by assaying for multiple fluorescent stains, which indicate successful delivery and subsequent viability after puncture. This design represents our interim step towards an UHT microinjection concept, with identical operational parameters that can be optimized with the current mechanoporation device. Overall, we believe that this device represents significant development towards a new platform technology for cellular manipulation, and progress towards a new standard for cell-based therapeutics.

2. METHODS

2.1. Introduction

Various methods and materials were applied throughout every study conducted for the UHT mechanoporation device project. The majority of these methods and materials were chosen based on precedent set by prior studies of similar devices. The cell types chosen to experiment on with our device were based on specific requirements set forth from the device qualities, and again via precedence from current literary sources. This chapter will give an overview of the primary techniques utilized to characterize the UHT mechanoporation device, as well as the importance of these techniques. Any specific recipes, concentrations, or experimental details can be found in the appendices of this dissertation.

2.2. Silicon

Silicon is one of the most heavily utilized materials in the semiconductor industry.[62] The relative ease associated with micromachining, its high flatness, and its low cost are some of the key reasons that silicon lends itself as an ideal material on which to create MEMS devices.[63] Moreover, there is a breadth of scientific literature that has been focused on the varying ways by which silicon can be etched to realize different geometrical structures. Finally, Si's low surface roughness (R_a ~ 0.2 nm RMS) allows it to produce high resolution features through photolithography.[64] These advantages, along with the literature precedent set by other research groups in regard to cellular manipulation devices using Si as the primary substrate, made this material the obvious choice to utilize in the fabrication of the UHT mechanoporation device.[65]

2.3. Lithography

Lithography was one of the primary processes by which we were able to realize the key functional features of our UHT mechanoporation device. More specifically, we utilized *photolithography*, which uses near-UV light (350-500 nm) to crosslink photosensitive polymer resist to generate patterns upon our silicon substrate for subsequent microfabrication. Several other research groups have reported the use of lithography to achieve patterned features similar in size and design to those of our UHT mechanoporation device [65]

In short, the primary steps associated with photolithography involve wafer cleaning, thermal oxidation of a SiO_2 layer to serve as both a surface on which the photoresist can properly anneal and as a potential shadow mask for subsequent processing steps, spin coating the photoresist, post-baking, exposing the resist to the mask pattern using a form of UV-exposure, and finally developing the resist to realize the final pattern.[62,66] The type of photoresist used during the lithography process is an important factor when beginning a fabrication process. For the fabrication of the UHT mechanoporation device, we utilized two positive photoresists. Positive photoresists become weakened when exposed to UV-light, and so are solubilized when developed in solution. This project used SPR 955 CM-0.9 and SPR 220-3.0 to realize the device layer features (aspiration vias), and the handle layer features (backside aspiration ports), respectively. SPR 955 CM-0.9 was applied for its high-resolution capabilities, while SPR 220-3.0 was used for its ability to spin thick films for deep mask etches. Specific

photolithography recipes for the UHT mechanoporation device can be found in Appendix C.

2.3.1 Contact Lithography

Contact lithography uses a mask in hard contact with the photoresist coated substrate, with contact pressures in a typical range of 0.05 to 0.3 atm.[63] A UV light source then exposes the substrate/photoresist for a user-defined amount of time. Depending on the exposure requirements, the force of contact and exposure time can be varied to alter the chemistry of the photoresist. This will then vary the developing step and subsequent results. Contact lithography's primary advantage is its simplicity of use and fidelity for large feature sizes. We used film masks for the realization of our backside aspiration ports, which were minimal in cost, and could be rapidly prototyped. More so, contact lithography allowed us to align the features on the handle layer of the device with those of the device layer with super-precision.

The resolution associated with contact lithography follows the equation below:

$$R = b_{min} = \frac{3}{2}\sqrt{\frac{\lambda z}{2}}$$

Where R is the theoretical resolution, b_{min} is the half grating period and the minimum size of a feature that can be exposed, λ is the wavelength of the exposing UV light, and z is the thickness of the photoresist.[63] The equation theoretically allows us to reach resolutions under 1 μm using contact lithography with short wavelengths and thin resist thicknesses. However, the major drawback from this lithography system is its lack of resolution due to other factors. Wafer flatness, edge diffraction, micro masking from debris, and wafer-to-

mask alignment all contribute to difficulties in generating small feature sizes.[63] For the realization of our device layer aspiration vias, with a feature size of roughly five microns, contact lithography was not an adequate method. As a result, we turned to projection lithography for the realization of our aspiration vias.

2.3.2. Projection Lithography

Projection lithography uses a series of lenses combined with the mask and light source to project an image of the pattern onto the photoresist coated wafer. The limiting resolution (R) of a projection lithography device is given by the following equation:

$$R = \frac{k_1 \lambda}{NA}$$

Where k_1 is a constant experimentally derived from resist parameters, mask aligner optics, and process conditions, λ is the wavelength of the exposing UV light source, and NA is the numerical aperture of the lens.[63] The high-resolution lenses allow for lithography with critical dimensions near 3 μm, exactly the range for the device layer of the UHT mechanoporation chip. Projection lithography systems also allow for an accurate depth of focus ($\pm$ 6 μm) and high overlay accuracy ($\pm$ 0.25 μm).[63] Specifically, the UHT mechanoporation project used a step-and-scan stepper system. In this system, the machine exposes a single portion of the wafer to the pattern desired, then moves a user defined increment to the next area and exposes again. This process is repeated until the entire wafer has been exposed to the pattern.

Because step-and-scan systems have independent control over each plane of movement (x, y, rotations, focus, and tilt), these machines are capable of precise alignment.

The stepper projection systems use reduction lenses to expose the photoresist. These lenses can reduce the image on the mask by a 10:1 or 5:1 scale.[63] This aspect of the step-and-scan technique allows for high resolution lithography through minimization of reticle inaccuracies. Such lenses also allowed us to create a chrome mask with a device array pattern significantly larger than the actual size of the aspiration vias, reducing the complexities associated with mask generation. Overall, the projection stepper system proved to be the most adequate technique to realize the patterns necessary for the device layer of our chip.

2.4. Deposition

Deposition was the first process that we applied to our silicon wafer during the fabrication of the UHT mechanoporation device. This methodology uses physical or chemical process to deposit thin layers of a user-defined material upon the substrate. In most cases, this additive process is used to realize three-dimensional structures upon the initial substrate wafer. Moreover, deposition can be utilized as a means of generating robust and permanent masks for subsequent etching of the substrate. In the context of the UHT mechanoporation chip, we utilized deposition to create SiO_2 masks that would serve to house the aspiration via patterns for our device layer, and the large backside aspiration port patterns on the device layer. Unlike photoresist, SiO_2 masks do not degrade over time, and are superior for extended fabrication protocols, as was the case with this project.

There are two forms of deposition, physical and chemical. Physical vapor deposition is a line of sight technique that uses a condensable vapor generated through non-

chemical processes within a vacuum that then deposits on the surface of the substrate. Evaporation and sputter coating are two well-known examples of PVD.[64] In contrast, chemical vapor deposition (CVD) uses the chemical reaction between a vaporous material with a heated substrate that leads to the deposition of a solid thin film upon the wafer. With plasma enhanced vapor deposition (PECVD), a plasma produces radicals that then provide energy for the chemical reaction through bombardment with the substrate. This provides for production of a thin film through chemical means, but at a much lower temperature.[64] Other advantages of CVD over PVD include a non-limitation to line-of-sight deposition, high throwing power for coverage of high aspect ratio features, thick coatings, and non-necessity of vacuums.[64] A CVD based process typically produces a better-quality film (higher density, lower etch rates) compared to its PECVD counterpart. As such we utilized thermal oxidation to produce our SiO_2 thin films that would later act as masks throughout the UHT mechanoporation chip fabrication process.

2.5. Etching

To realize the bulk of our features for the UHT mechanoporation device, we relied on subtractive processes applied to our wafer. These processes remove, or etch, material from the substrate and lead to the realization of features within the surface of the wafer. Several forms of etching are available for microfabrication processes and are typically grouped into two primary methods: dry etching, and wet etching. Dry etching applies a plasma to remove material from the substrate, while wet etching uses chemical (i.e. HF,

H_2SO_4, etc.). In most cases, directionality and high aspect ratio structures is achieved through dry etching techniques.

2.5.1. Reactive Ion Etching (RIE)

This technique applies a radio frequency (usually 13.56 Mhz in frequencey) to ignite the plasma used for etching.[64] Appendix figure B.1 demonstrates the two-diode setup for a RIE device. A radio frequency is applied between the cathode and anode, which causes oscillations of free electrons between the electrodes. These electrons then collide with the user specified gas in the system and produces the plasma. The plasma's constituents include cations, anions, radicals, and photons.[62] Placement of the wafer to be etched on the anode in combination with the active plasma leads to etching of the substrate through sputtering of reactive ions. The large voltage drop created by the presence of the cathode and anode leads to movement of the positively charged ions towards the anode. At this point these ions impact the surface of the exposed wafer, which leads to removal of substrate material (via chemical reaction or kinetic collision).[64]

RIE was primarily useful due to its capability of isotropic etching. We used RIE for the simultaneous realization of both the hemispherical capture wells and the preliminary form of the solid central penetrators in the UHT mechanoporation device. Such a step significantly simplified fabrication challenges, especially in regard to the sub-micron tip diameters necessary for the solid penetrators.

2.5.2. Deep Reactive Ion Etching (DRIE)

Deep reactive ion etching (DRIE) is a method by which we can achieve high aspect ratio structures for specific device applications. For the UHT mechanoporation chip, these high aspect ratio structures included the aspiration vias necessary for capture and release functionalities, and the back-side aspiration ports that allowed for identical control of every capture well during device operation.

This etching technique uses an inductively coupled plasma source that is created by a helical resonator and an electrostatic shield. Typically, the power source for DRIE is 12.56 MHz, which produces a high density, low-pressure, and low-energy plasma. The most common form of DRIE is the Bosch process (Appendix figure B.2).[62]

The Bosch processes uses cyclical passivation and etching steps to allow for deep, and high aspect ratio structures to be etched into the substrate. Glow discharge has the tendency of generating polymer species via chemical crosslinking during its process.[62] These species then deposit themselves in exposed areas of the substrate (non-PR coated or masked). Because this deposition rate is faster than the rate at which the polymers are re-etched away, we can use this system as a form of "protection" to achieve deep etches while maintaining anisotropy. By alternating rounds of etching and passivation, the Bosch process can protect isotropic etching of side walls while creating deep trench etches by preferentially etching only the bottom of the trench.[62] As seen in Appendix figure B.2, we start with an etch process using SF_6 gas plasma. From there, we switch to a passivation step using C_4F_8 that creates the passivation layer which coats the etched area. Because sidewalls run parallel to the movement of the bombarding etching ions, the polymer is

removed with a bias from the bottom of the trench, which is then further etched using SF_6 plasma. The resulting features exhibit a scalloped side wall profile due to this cyclic etching-passivation method.[62] This process was a highly effective and repeatable method by which we could achieve the deeply etched features of our UHT mechanoporation device.

2.6. Characterization

Throughout the fabrication process and device testing, two primary methods of characterization were applied to either measure the fidelity of each fabrication step or observe device operation in real time. Scanning electron microscopy (SEM), due to its high-resolution capabilities was used to assess the outcome of each fabrication step, and to determine the relative sharpness of the completed solid central penetrators. Fluorescence microscopy was used to address one of the limitations inherent to studying live cells under a microscope. As most cells are transparent, a bright field filter was not adequate to measure cell movement and capture well occupation during chip testing. The cell types were thus stained with fluorescent viability markers to reduce the ambiguity associated with cell position and cell density on the capture arrays under a bright field filter.

2.6.1. Scanning Electron Microscopy

Scanning electron microscopy (SEM) is a technique by which we exploit the interactions of electron beams with our object of interest to produce high-magnification and high-resolution images far beyond the capabilities standard optical microscopy. In

SEM, a focused beam of accelerated electrons scans the surface of an object. These electrons are then scattered in various directions and produce a range of different signals from their loss in energy through interaction with the object. Such signals result from elastic scattering, inelastic scattering, and electromagnetic radiation.[64] Inelastic scattering, which occurs when electrons reflect off the surface to be imaged and hit one of the detectors of the system, is the most common imaging method used in SEM. Depending on the angle of incidence of the electrons, varying numbers will hit the detector. This variation allows for differences in brightness across the area that is imaged.[64] Brighter areas denote higher angles of incidence, while dimmer areas denote lower angles of incidence. This subsequently results in a 3D-like rendering of the sample's surface. Because the wavelength of light is the limiting factor in resolving the details of a sample, the relatively small wavelengths of electrons ($\sim 10^{-12}$ m) allows us to achieve sub-micron resolution of our UHT mechanoporation device.[64] This capability was a key element in understanding the fidelity of our etching processes, as well as roughly measuring the tips of the solid central penetrators, which directly contribute to overall device efficiency.

2.6.2. Fluorescence Microscopy

This form of microscopy uses the phenomenon of fluorescence to visualize an object of interest. Orbital electrons in a molecule are capable of absorbing specific wavelengths of light. When this event occurs, these electrons are excited from their ground state into a higher orbital (excited state).[67] As this excitation cannot last for long, the electrons eventually return to their ground state and release energy, typically in the form

of light. Since energy is lost in the process of excitation to relaxation, the wavelength of light released is always of lower energy than the wavelength of light used to excite the electrons.[67] For example, an excitation wavelength in the blue spectrum will result in fluorescence in the green spectrum by the molecule. Fluorescence microscopes have allowed us to visualize cells stained with molecules capable of emitting certain wavelengths of light after excitation with a filtered light source. The microscope uses an excitation filter to remove all, but the wavelength of light used to excite the fluorescent moiety. This light is then reflected by a dichroic mirror through the objective, and shines on the subject.[67] The subject then fluoresces, and the resultant emitted light passes back through the objective and into the dichroic mirror, which transmits the light through a view finder or attached camera. It is important to note that the dichroic mirror only transmits the emitted wavelength of light into the viewfinder/camera not the bright excitation light.[67]

This imaging system was the primary means by which we were able to visualize the UHT mechanoporation device operation. All cell models that were used for our experiments were nearly colorless and transparent when imaged under bright field. To allow for more accurate tracking and capture efficiency calculations, we stained each of our cell models with either a Calcein AM stain, or a CellTracker CMFDA dye. These dyes localize within live cell cytoplasms, and exhibit very little background or extracellular fluorescence. Therefore, fluorescence microscopy allowed us to monitor the location and movement of our cell population down to a single cell resolution when introduced into the cell reservoir during chip testing.

2.7. Methods to Assay cells

2.7.1. Hemocytometry

The hemocytometer was first invented by the French anatomist Louis-Charles Malassez in the 19th century as a means of calculating cellular concentration in solution. We applied this technique to initially assess the efficiency of our UHT mechanoporation device due to its extended use historically for cell counting.[68]

A hemocytometer relies on a set of laser-cut grids and a precise volume between the cover slip and the surface of the grid to allow for an accurate calculation of cell concentration. The cover slip rests at a height of 0.1 mm above the surface of the grid. Each hemocytometer contains two chambers capable of containing 10 μL, each with a set of grids. Above the four 1 mm^2 counting squares, we attain a total volume of 400 nL.[69] Cells are counted on all four of these square grids, with the right and bottom edges excluding cells on the boundaries and top and left edges including cells on the boundaries. The total number of cells counted per square is then averaged. Because each square grid represents a total volume of 100 nL, or 10^{-4} cm^3, and 1 cm^3 roughly equals 1 mL, we can multiply the average number of cells by 10^4 to generate a concentration of cells per mL.[69] In most cases, a dilution factor is also multiplied when calculating the concentration.[69]

Following a mechanoporation procedure, we added an aliquot of mechanoporated cells to each chamber of a hemocytometer to assess for delivery efficiency and viability for each experiment. While studies have been conducted that confirm the accuracy of hemocytometry for calculating cell concentrations (in comparison to automated cell counting and flow cytometry), there were several shortcomings associated with this

method.[70,71] The necessity of manual counting and fluorescence microscopy resulted in a high degree of subjectivity when deciding the signal of a cell. Several images required post processing to boost the fluorescence signal and thus introduced ambiguity as to whether the observed fluorescence was from the cell background or from the fluorescent molecule. More so, as the hemocytometer yields cell concentration, true cell counts were impossible to ascertain, along with accurate release percentages. Though this method of cell assaying successfully indicated the proof of concept for the UHT mechanoporation device, it was ultimately inadequate for the high single cell fluorescence resolution required to calculate device efficiencies.

2.7.2. Flow Cytometry

Flow cytometry can be summarized as a technique of studying how cells interact on an individual level with a laser, which allows the user to glean conclusions about the cell population (i.e. viability, size, granularity, presence of a fluorescent molecule, etc.). This technique was of importance to our project due to the similarity in concept of our device and the flow cytometer. The UHT mechanoporation device treats large masses of cells on an individual level. As such, we required a form of cell assaying capable of finding the efficiency of the device in a similar fashion. The flow cytometer allows us to draw general conclusions of bulk cell populations by assaying each cell individually. Thus, flow cytometry became the primary form of calculating device efficiencies following hemocytometry.

Typically, most flow cytometers share four common elements: 1) a source of focused light that interacts with the physical components of a cell, or excite fluorescent moieties either within the cell cytoplasm or the cell surface; 2) fluidic circuitry responsible for uptake of the cell sample solution into the flow cytometer and precise guiding of the cell solution through the light source; 3) a network of photodiodes and photomultiplier tubes to detect the light that has interacted with the cell sample and generate electrical signals that represent the light intensity; and 4) a computer system to log each interaction and allow for analysis of the data.[72]

A combination of various lenses within the flow cytometer are used to focus the source light down to a micron scale (just large enough to ideally excite a single cell). However, the classical setup of simple spherical lenses leads a shortcoming of the system. These spherical lenses result in a Gaussian profile of the excitation light source. Thus, if a cell strays too far from the center of the point light, it will be exposed to a significantly lower light intensity. To alleviate this flaw, most flow cytometers use combinations cylindrical lenses that result in an elliptical light spot with the major axis of the ellipse orthogonal to the flow of cells. This allows for a higher tolerance for even illumination if the cell happens to stray from the center of the light point. In addition, a narrow minor axis provides for increased temporal resolution of the cells. Because the beam is so narrow in the direction parallel to flow, the instrumentation will be able to resolve individual cells with higher fidelity compared to a circular excitation point (i.e. each cell will pass through the ellipse much more quickly). This reduces instances where two cells will be simultaneously excited and result in a single point of data. Multi-laser flow cytometry

systems have several elliptical light points in succession to one another. Each cell will sequentially pass through every light point.[72]

To accurately align a single row of cells and pass them through the illuminating light source, the flow cytometer uses a sheath fluid (typically phosphate buffered saline solution) combined with hydrodynamic focusing. In most instruments a motorized syringe removes the cell sample from the test tube and transports it into a chamber known as the flow cell. The flow cell is directly upstream of the analysis point, and it is here that the cell sample solution and sheath fluid meet. Using filtered and pressurized ambient air, the flow cytometer combines the sheath fluid with the cell sample solution and creates a coaxial flow condition. The sheath fluid acts as a protective and guiding stream for the cell sample in the core of the fluid flow. This coaxial flow then passes through the illuminating point wherein cells are assessed for various attributes by the instrument.[72]

One of the primary factors that influence the accuracy of the flow cytometer is the sheath flow, which is determined by the amount of pressure applied to drive the sample and sheath fluid through the illuminating point. Though higher pressures may allow for faster data acquisition times, they may lead to perturbation in the uniformity of flow. This deviation from flow uniformity will lead to inconsistencies in data generation. On the opposite end, too low of a pressure will substantially increase the time for complete cell assaying. Reasonably increasing the sample cell concentration prior to flow cytometry helps to reduce sampling times, but too high of a concentration will result in two particles being measured at once. Qualitatively, it has been found that a rate of 1000 cells per second is an optimal rate for most flow cytometers.[72]

As cells flow through the chamber exposed to the point light (i.e. the analysis, observation, or interrogation point), an array of various lenses and detectors surround the area to generate different forms of data per assayed cell. The lenses first collect the light that has interacted with the cells, constituting the "signal". These lenses then focus the light onto either the photodiodes or photodetectors, which then generate an electrical impulse that is fed into the connected computer. Each electrical impulse is proportionally related in intensity to the impinging light. There are primarily two orientations of detectors for data acquisition. One detector is oriented in a direct line to the illuminating point source. This detector contains a metal strip across its center. As such, light that hits only the edges of the detector generates a signal. This constitutes the data known as forward scatter (FSC) or forward-angle light scatter (FALS), and pertains to the size, volume, and refractive index characteristics of the cell (more accurately, the cross-sectional area). The remaining detectors are oriented around the point light at right angles. Some are responsible for sensing light that has been emitted by the cell through fluorescence, and others that pick-up light that has been reflected to the side by the cell. In most cases, the more granular a cell is, or the more surface irregularities it may have, the more light that will be reflected to the side. These signals constitute the side scatter (SSC) data and indicate details about the texture of the cell as well as its internal structures.[72]

Each point signal generated by the detectors appears as a single point on a plot via the flow cytometer's analysis software. This point is known as an event. The most subjective portion of flow cytometry, gating, is what allows us to generate data about UHT mechanoporation efficiencies. By gating on control cells, a sample of high population

density, we defined the boundaries of our FSC/SSC, and fluorescence channels with minimal subjectivity. Our gates were always first drawn from our forward and side scatter data to encompass all events that exhibited characteristics akin to Jurkat cells. This allowed us to ensure that all Jurkats would be initially included in the calculations of our device efficiencies. This subpopulation would then be assayed for viability on a fluorescence channel. We gated for viability prior to delivery because the efficiency of the UHT mechanoporation device rested on cells that survived the procedure over the number of non-viable cells exhibiting fluorescence from our delivery molecule. Our final gate was then to check how many viable cells were successfully delivered with our exogenous payload. This procedure largely encompasses how we calculated the capabilities of our device.[72]

Flow cytometry, via its concept and operation, holds several advantages over hemocytometry when applied to analysis of the UHT mechanoporation device. Unlike hemocytometry, flow cytometry can assay the entire sample of cells recovered from a mechanoporation experiment. This not only allowed us to calculate efficiencies of delivery and viability from a whole population (rather than inferring it based on ratios), it also allowed us to assess a third factor of the device, that of release. Flow cytometry has given us an insight into how many cells we can recover in total and demonstrates avenues to further improve the design of the mechanoporation chip. Finally, there is a substantial basis in the literature to using flow cytometry to assay Jurkat and K562 cells, with several studies using this method to find varying details ranging from apoptosis to single cell functional staining.[73,74]

3. DESIGN AND FABRICATION OF AN ULTRAHIGH THROUGHPUT (UHT) MECHANOPORATION DEVICE

3.1. Introduction

This chapter outlines the fabrication and rudimentary testing of the UHT mechanoporation device. We outline the processes used to generate a massively parallel array of hemispherical capture sites that are capable of individually puncturing the plasma membranes of each cell allowing for transient membrane poration and resultant passive diffusion of our exogenous payload. In addition, we describe the results of microbead and mouse embryo fibroblast (MEF) testing to confirm desired capture, penetration, and release functionalities of our chip. The results from this study were used as the fundamental basis for all subsequent

3.1.2. Ultrahigh Throughput Mechanoporation Device Concept

Figure 3.1 illustrates the functional concept for our MEMS-based approach to achieving ultrahigh throughput mechanoporation. In this design, cells are captured into sites by negative flow through aspiration vias situated at the bottom of the wells [figure 3.1(a)]. As cells are captured, they are drawn onto fixed solid microneedles within the wells and held in place by an immobilization flow [figure 3.1(b)]. Once poration is completed, cells are released by positive aspiration, and recollected by the operator. Upon release, the transient mechanical membrane disruption enables transfection via diffusive influx of exogenous molecules from the surrounding suspension [figure 3.1(c)].

The UHT mechanoporation device consists of a 100 x 100 array of capture wells fabricated using bulk silicon micromachining (figure 3.2). Each unit cell within the device is composed of a 15 μm diameter capture well with a monolithically integrated solid

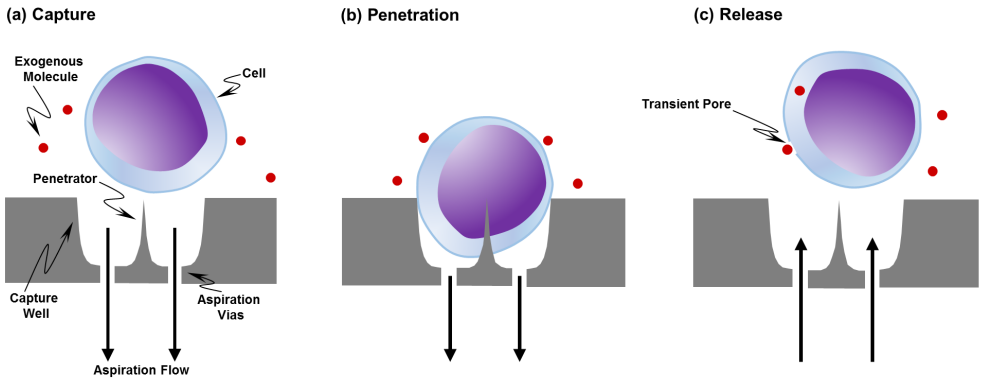

Figure 3.1. Mechanoporation device operation concept (illustrated for a single capture site within a larger array). Each capture site consists of a hemispherical capture well with a centrally-located solid penetrator and a multiplicity of aspiration vias situated at the bottom of the well. Mechanoporation is achieved through: (a) Use of negative flow through aspiration vias for cell capture; (b) Poration of the plasma membrane by the penetrator; and (c) Reversal of aspiration flow to release the cell. Intracellular delivery is achieved upon release of the cell, via passive diffusion of exogenous molecules through the transient pore produced by the penetrator.

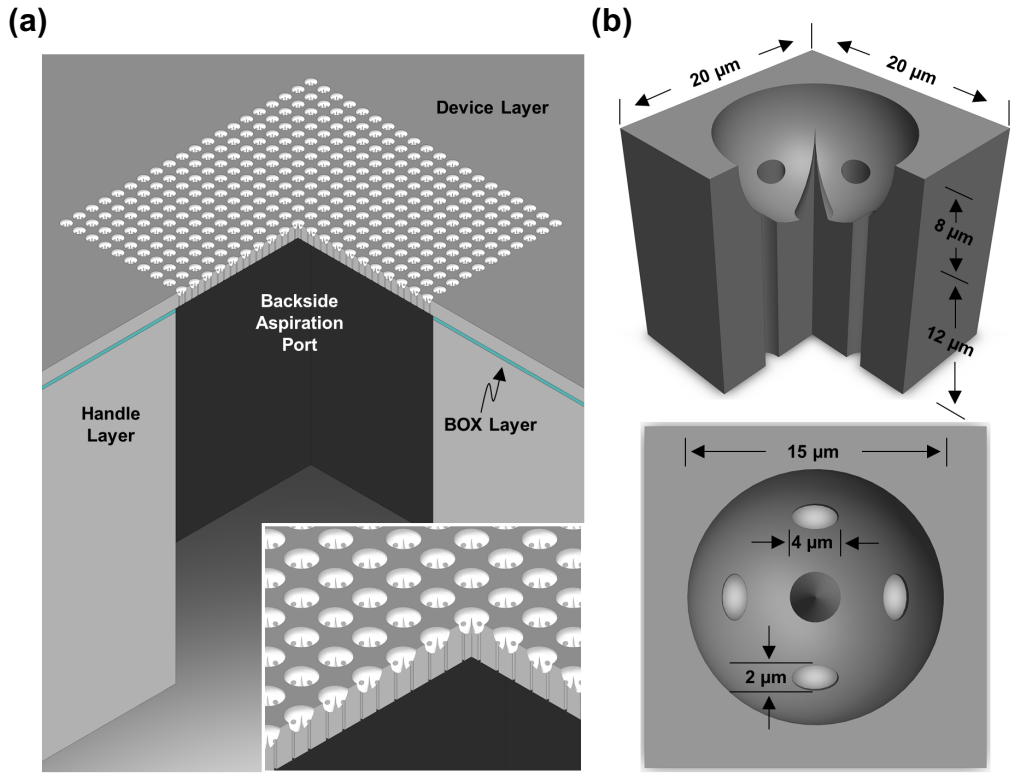

Figure 3.2. Schematic illustrations of the mechanoporation device, whose design is based upon use of a silicon-on-insulator (SOI) substrate. (a) Isometric view of the device chip with a quarter-section removed to allow visualization of the backside aspiration port underlying the capture site array. The inset shows a higher magnification view of the capture site array with a quarter-section removed to illustrate the connection of all aspiration vias to the backside aspiration port. Note: A 20 x 20 capture site array is pictured for the sake of clarity; however, actual devices contain a 100 x 100 array. (b) Isometric and plane views of a single capture site, with a quarter-section removed from the former to allow visualization of the capture well, penetrator, and aspiration via geometry.

penetrator and 4 elliptical aspiration vias (4 μm major axis; 2 μm minor axis). The aspiration vias provide connection to a common backside port to ensure uniformity of flow across the array [figure 3.2(a)]. Elliptically shaped vias are chosen to yield the desired well geometry and simplify fabrication. Use of multiple vias in each well provides uniform tension on the cell to facilitate penetration. The penetrators are roughly conical with a 1 – 2 μm base tapering to a sub-μm tip [figure 3.2(b)]. When coupled with the high strength of silicon, this maximizes reliability and minimizes penetration force, thus minimizing stress on the cell. Recent studies show that comparable structures produce minimal membrane deformation, thus enhancing the viability and reducing the potential for mechanotransduction-induced artefacts.[75,76] In addition, proper design and optimized operational parameters can greatly reduce mechanical damage to cell membranes.[47]

3.2. Materials and Methods

3.2.1. Wafer Cleaning and Deposition of SiO_2 Device and Handle Layers

Fabrication of our UHT mechanoporation chip began with a multi-cycle cleaning process of a 4-inch silicon-on-insulator (SOI) wafer (Ultrasil Corporation). We applied a combination of Piranha, HF, and an RCA2 clean to strip the wafer of any contaminating agents. All specific processing steps can be found in Appendix C of this dissertation and were completed in collaboration with the prior doctorate student on this project (cite Clara's dissertation). The SOI wafer used in our device fabrication was composed of a 20 μm Si device layer, a 500 μm Si handle layer, and a buried 2 μm SiO_2 BOX layer. Wet oxidation was performed using a low pressure chemical vapor deposition system to deposit

1 μm of SiO_2 on both the device and handle layers of our substrate. An additional 2 μm of SiO_2 film was deposited on the handle layer of our wafer using plasma enhanced chemical vapor deposition. These processing steps established necessary SiO_2 films, which became our oxide masks [figure 3.3(a)].

3.2.2. Substrate Patterning and Lithography of Device Layer, and Mask Pattern Transfer

We then proceeded to define the aspiration via features on the device layer of the wafer using high-resolution projection (stepper) lithography. In addition to delineation of aspiration via features, this lithography step defined the boundaries of individual device chips, which were diced at a later fabrication stage. As such, each SOI wafer produced 21 UHT mechanoporation chips. Once the aspiration via features had been defined and developed on photoresist, with a film thickness of 1 μm, they were transferred into the SiO2 mask via reactive ion etching [figure 3.3(b) & (h)].

3.2.3. Substrate Patterning and Lithography of Handle Layer, and Mask Pattern Transfer

To create the large aspiration ports on the handle layer of our substrate, we first utilized lower resolution contact lithography to define these features in our photoresist. The film thickness was 3 μm. These backside ports were transferred into the SiO2 mask, again by reactive ion etching [figure 3.3(c)].

The fidelity of dry etching of both the device layer and handle layer features thus far were characterized using a surface profilometer. Before continuing on with device fabrication, the SOI wafer was diced into its 21 single dye pieces using a diamond scribe.

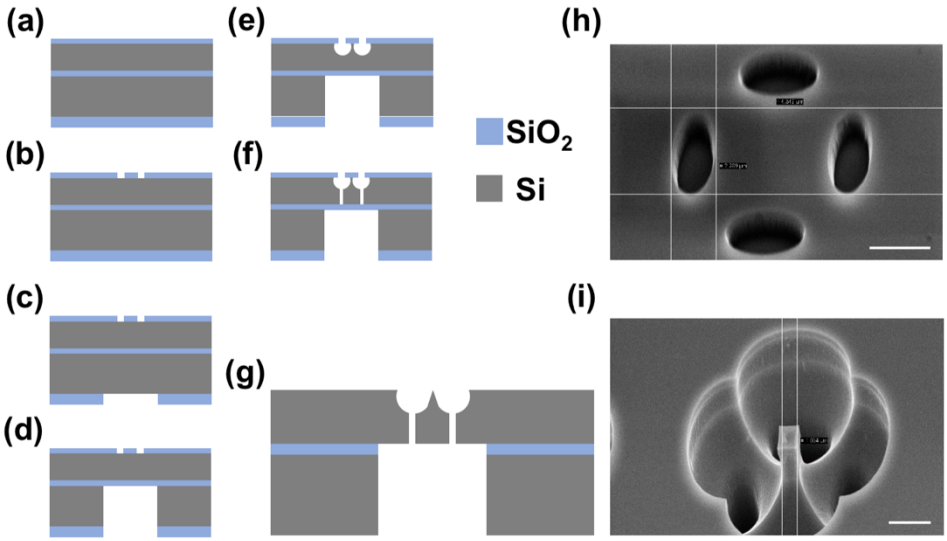

Figure 3.3. Mechanoporation device fabrication process. Note: Only a single capture site is pictured for the sake of clarity; actual devices contain 10^4 capture sites. (a) Front and backside mask oxide deposition on the SOI substrate. (b) Frontside mask oxide dry etch for patterning of the aspiration vias. (c) Backside mask oxide dry etch for patterning of the aspiration port. (d) Backside Si DRIE for definition of the aspiration port. (e) Frontside isotropic Si dry etch for simultaneous definition of the capture wells and penetrators. (f) Frontside shadow-masked Si DRIE for definition of the aspiration vias. (g) Frontside dry etch to remove the residual mask oxide, followed by Si dry etch to refine the penetrator tips, and backside BOX dry etch to open the bottoms of the aspiration vias. (h) Scanning electron micrograph of aspiration via etch into the SiO_2 device layer (scale bar: 3 μm). (i) Scanning electron micrograph following the isotropic etch of the aspiration vias on the device layer to realize the hemispherical capture well geometry (scale bar: 3 μm).

3.2.4. Realization of Device and Handle Layer Features in the Si Substrate

Silicon deep reaction ion etching (DRIE) was then performed on the handle layer up to the BOX layer to define the large, backside aspiration ports [figure 3.3(d)].

The chip then underwent silicon isotropic etching to simultaneously produce the capture wells and the solid microneedles on the device layer. This isotropic etch step was chosen to reduce fabrication time by concatenating the production of both the capture well and the solid central penetrator. Isotropic etching was then followed by Si DRIE on the device layer to produce the frontside aspiration ports [figure 3.3(e)/(f)/(i)].

3.2.5. Removal of SiO_2 Shadow Mask Layer, Penetrator Refinement, and Final Device Cleaning

With etching of the major chip features now complete, the SiO2 mask on the device layer was removed using RIE, and the microneedle tips were refined using Cl2 anisotropic etching. These tips were further refined through the passivation removal via reactive ion etching [figure 3.3(g)].

Our final fabrication step involved SiO2 mask removal of the chip handle layer, and removal of the SiO2 BOX layer by reactive ion etching. Both device layer and handle layer features were verified using SEM imaging. The completed UHT mechanoporation chips were thoroughly stripped of organic contaminants using an alternating process of piranha cleans and O_2 ashing.

3.2.6. Design of a Polycarbonate Housing for Device Testing

Due to the nature of the device design, manual cell introduction over the array was required prior to any mechanoporation procedures. As such, an experimental apparatus was fabricated from a single polycarbonate block (McMaster-Carr; design: SolidWorks 2013; fabrication: Department of Mechanical Engineering Machine Shop, UC Riverside) [figure 3.4]. This apparatus was critical to properly test the UHT mechanoporation devices. Engineering drawings of this fixture set can be found in Appendix C of this dissertation (figure C.1 and C.2). The device chip was sandwiched between two 250 μm polydimethylsiloxane (PDMS) gaskets (McMaster-Carr), and was then clamped between the two parts of the polycarbonate fixture. The top section of this fixture provided an open reservoir above the chip for micropipette-based cell introduction and recovery, while the bottom section of the fixture contained a large port beneath the device array to provide for fluidic access.

The fixture set would then be placed on the stage of a fluorescent microscope equipped with a digital camera allowing for recording of the experiment (fluorescent imaging & video). An external high intensity lamp (Leica) provided for cell visualization, while the built-in backside microscope lamp allowed for visualization of the mechanoporation array. Finally, a syringe pump and a 10 ml glass, gastight syringe (Hamilton) was connected to the fixture set's aspiration inlet using finger tight fittings (IDEX Health and Sciences) and LC tubing (IDEX Health and Sciences). This would render a completed aspiration circuit. In some experimental setups, a digital pressure transducer (Omega DPG 4000-15) was connected between the syringe pump and fixture

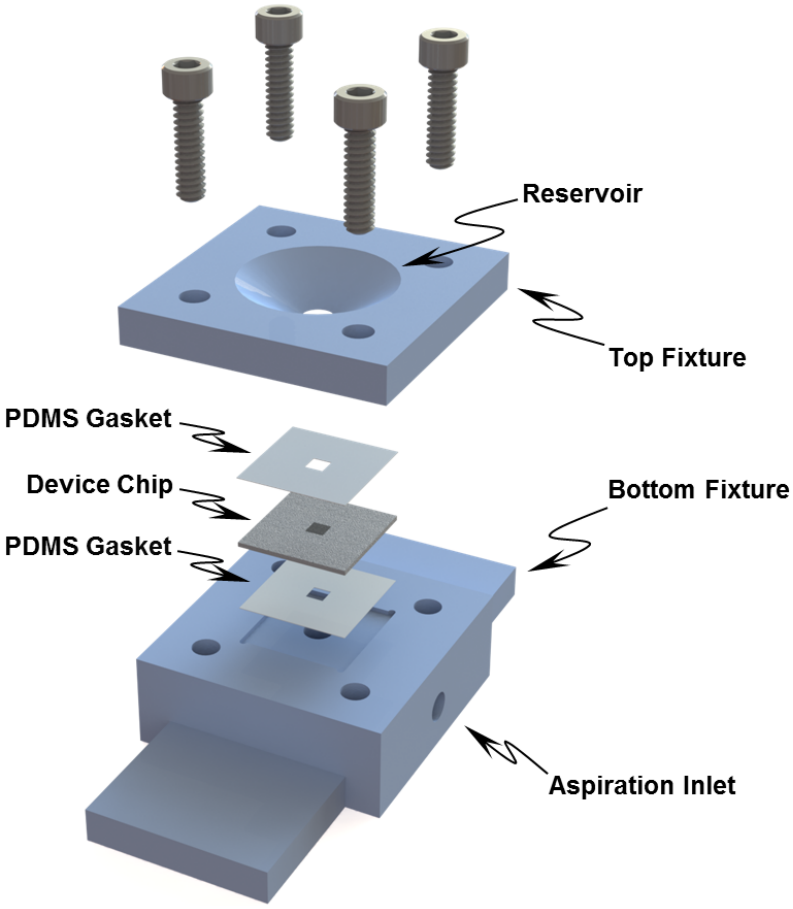

Figure 3.4. Exploded view of the fixture used for packaging of the device chip. The open nature of the reservoir in the upper portion of the fixture provides a simplified means for introducing the cell suspension to the device chip, as well as collecting the cells after the mechanoporation procedure. The aspiration inlet in the bottom portion of the fixture provides fluidic connection to a syringe pump (not shown) for actuation of the aspiration circuit.

set to record pressure drops during device testing. Product information about the experimental hardware can be found in Appendix C.

3.2.7. Preparation of Fluorescent Polystyrene Microbeads and Mouse Embryo Fibroblasts (MEF cells) for Rudimentary Device Testing

For the preliminary characterization of the UHT mechanoporation device, we used 2 experimental setups: one involving fluorescent polystyrene microbeads of varying diameters, and the other involving fluorescently stained mouse embryo fibroblasts. The fluorescent microbeads measured either 7.5 μm in diameter [PS/DVB·(540,600); Bangs Laboratories] or 15 μm in diameter [PS/DVB·(480,520); Bangs Laboratories]. Following chip experimental setup, the beads were diluted to a concentration of 3500 beads/μL in PBS, with a total of 70,000 beads added in a single pipette step (20 μL total volume). A total of 3 capture rates were applied during fluorescent beads testing: 10, 20, and 40 μL/min. As these beads are rigid and incapable of puncture, the preliminary tests were primarily applied to confirm fluidic connection between the device and handle layer of the UHT mechanoporation chip.[77]

Subsequent testing of the UHT mechanoporation chip involved the use of mouse embryo fibroblasts (MEFs) [cultured at 37˚C, 5% CO_2]. Prior to device testing, the MEF cells were trypsinized from the culture plates and stained with live/dead staining (calcein AM green/ethidium homodimer-1, Thermo-Fisher Scientific) at a concentration of 2 μM and 4 μM respectively for 30 minutes. The cell sample was then washed of the live/dead staining solution using a standard centrifugation process with subsequent aspiration of the

supernatant. The MEF cell sample was then resuspended in PBS at a concentration of 2500 cells/μL. The UHT mechanoporation device experimental setup was constructed along with an in-line pressure transducer to monitor pressure drops as introduced cells successively began to occupy the device array. A total of 50,000 cells were added to the cell reservoir with an applied capture flow rate of 10 μL/min. Excess cells were washed away during the capture step, and a flow rate of 70 μL/min was then applied for the puncture stage. Images of the punctured cells were acquired using the attached CCD camera (Imagingsource). Capture efficiency was assessed visually. Similar to the studies involving polystyrene microbeads, these MEF cell studies were conducted to assess the basic capture functionalities of the mechanoporation device, but now with non-rigid bodies that could properly localize over a capture well.

3.3 Results and Discussion

3.3.1 Characterization of Device Features

Both device layer and handle layer features were verified using SEM imaging (Leo Supra 55). Scanning electron micrographs of a fabricated device are shown in figure 3.5(a). Realization of high-aspect ratio, sub-μm tip diameter penetrators is clearly evidenced.[77] However, capture well geometry deviates from the desired hemispherical profile due to transport limitations during the isotropic etching step. This deviation from optimal geometry may adversely affect cellular viability due to the sharp edges of the "cloverleaf" profile, though no studies have been conducted to confirm this theory. Nevertheless, good uniformity of the capture wells is observed across the array.

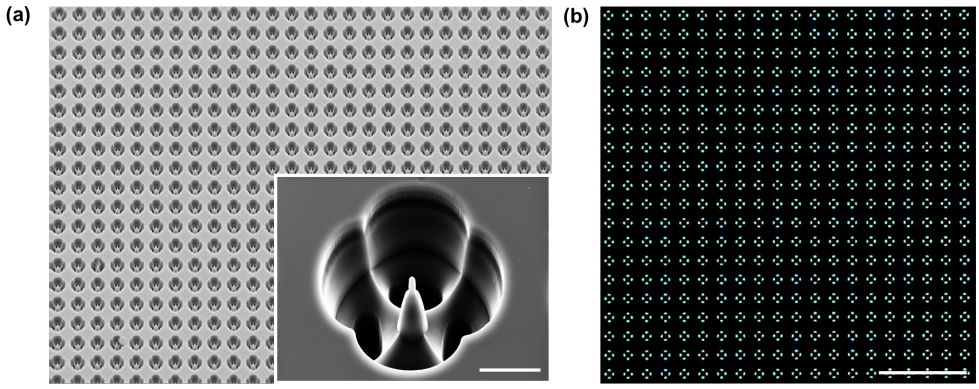

Figure 3.5. Device fabrication results. (a) Scanning electron micrograph of a subsection of the capture site array with an inset showing a higher magnification image of a single capture site (scale bar: 10 μm). (b) Optical micrograph of a subsection of the capture site array illuminated from the backside to demonstrate the patency of the aspiration vias (scale bar: 100 μm).

Completed deep etch of the aspiration vias, as well as successful connection of these vias to the backside aspiration ports is confirmed through backlight microscope verification, as can be seen in figure 3.5(b). We observe uniformity of this fluidic circuitry across the entire device.

3.3.2 Characterization of Device Functionality with Polystyrene Microbeads

The primary goal of testing with the polystyrene microbeads was to confirm the successful fabrication and aspiration functionalities of the UHT mechanoporation device. As can be seen from figure 3.6(a), we can observe substantial localization of the 7.5 μm beads over the capture well space, with even and non-specific spreading of beads over the "dead" or the non-functional areas of the device array (not pictured). This indicates a generally successful alignment of the aspiration vias on the device layer to the large backside aspiration ports on the handle layer. Moreover, it is important to observe that no discernable pattern or ordered arrangement of beads can be found across any of the four device arrays. Also, it is quite apparent that the distribution of captured beads is not even across the functional space of the device, but rather exhibits a highly "clumped" phenotype.

This can be explained from two primary principles. First, because the polystyrene beads are rigid spheres, they are incapable of deforming in such a way as to cover all four aspiration vias, especially due to the presence of the solid central penetrators. This results in capture of these beads in the area between the central penetrator and the capture site wall, better observed via the brightfield image [figure 3.6(b)]. Second, because the beads are undersized relative to the capture well, when a single bead settles into the site, it is

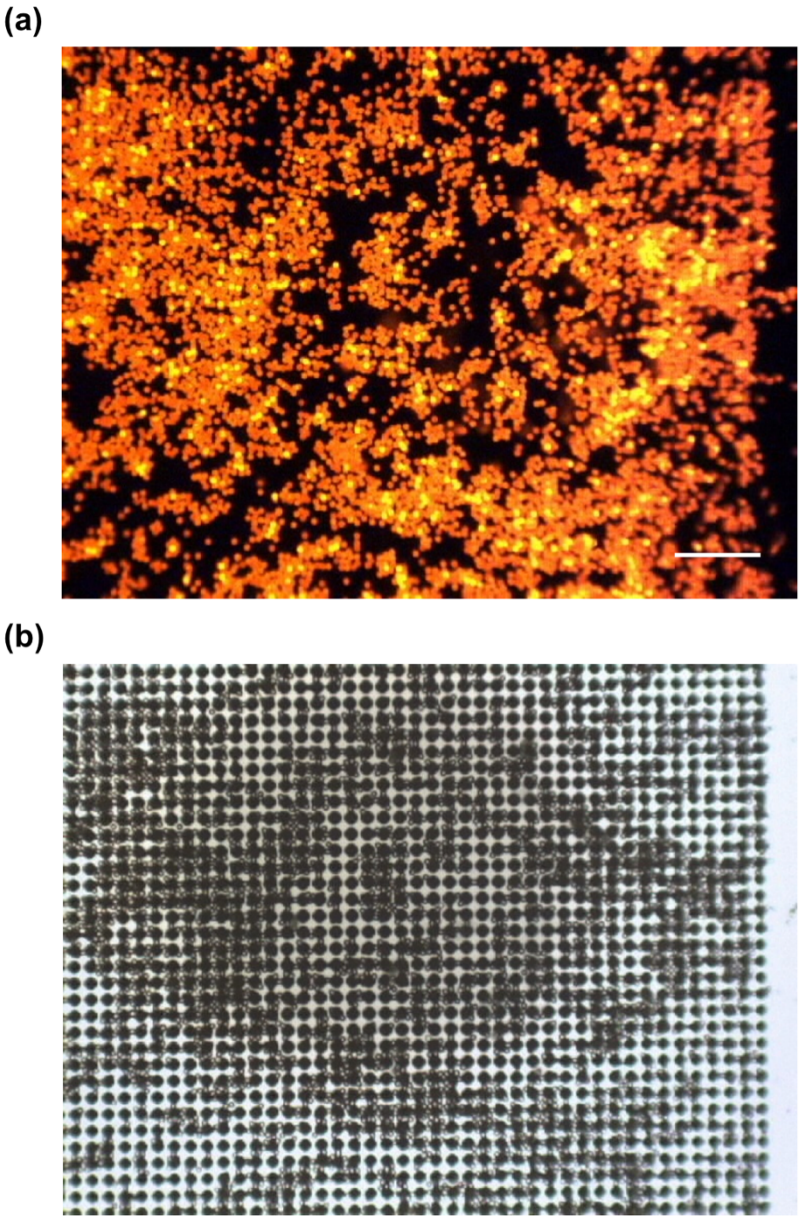

Figure 3.6. Cell testing images taken using 7.5 μm fluorescent polystyrene microbeads to confirm chip functionality. Only a subsection of the device array is shown for better visualization of bead localization. (a) Fluorescent image of the polystyrene microbeads atop the capture array (scale bar: 100 μm). (b) Brightfield image of the same array area in part (a) to allow for clearer visualization of bead placement vs. capture well location.

incapable of covering all four vias simultaneously. As a result, a leakage flow arises from partially occupied capture wells. This leakage flow attracts free beads in solution, causing them to also settle into what is already an occupied capture site. Until the site is fully covered, we hypothesize that the leakage flow is never stopped. This causes the clumping seen in the arrays.

Following successful confirmation of chip fluidic functionalities, we moved on towards the use of polystyrene microbeads with a size similar to our ideal cell diameters (15 μm). We applied the identical capture flow rate conditions as those utilized in our previous experiment with the 7.5 μm diameter beads, and also introduced the same number of 15 μm beads into the fixture reservoir (70,000 in 20 μL). Figure 3.7 illustrates the results of the capture study over the three flow rates applied: 10 μL/min, 20 μL/min, and 40 μL/min.[77] After addressing the issue of bubbles below the capture array, which impeded optimum bead capture, we can observe increasing capture efficiencies with larger flow rates and extended capture times. However, with better capture site occupation from increased flow rates comes a higher degree of cell clumping. It is thus apparent that capture efficiencies can be optimized through a balance between the applied flow rate for capture, the time allotted for the capture step, and the means by which beads, or cells, are introduced into the reservoir. Though we introduced the polystyrene beads in a single step for this proof of concept study, we hypothesized that introduction of cells through "bursts" or smaller volumes may further improve capture efficiency and modulate the degree of clumping associated with higher capture flow rates.

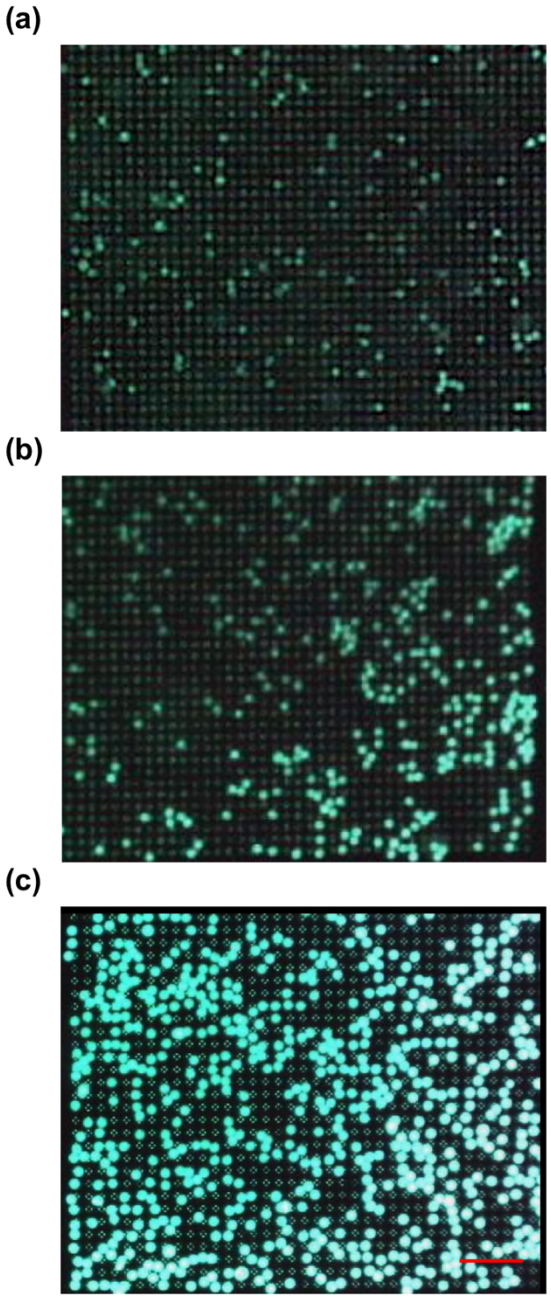

Figure 3.7. Fluorescent micrographs of array sections during capture studies using 15 μm polystyrene microbeads. (a) Bead localization after a 10 μL/min capture flow rate. (b) Bead localization after a 20 μL/min capture flow rate. (c) Bead localization after a 40 μL/min capture flow rate (scale bar: 100 μm).

3.3.3 Characterization of Device Functionality with Mouse Embryo Fibroblasts

These experiments served to further confirm device functionality, but now with a biological sample capable of interacting much more effectively with the device than rigid polystyrene microbeads. To better visualize MEF cells during the mechanoporation process, we stained our sample with a live/dead solution. This served a dual purpose of allowing optimum imaging of cell movement during chip operation and helped to negate any dead cells from being counted in our capture efficiency estimates. Only live cells would be capable of enzymatically cleaving the calcein AM green molecule, thus conferring green fluorescence. As a result, dead cells would not fluoresce green, and thus would not be counted in the capture efficiency even if occupying a capture well.

Figure 3.8 illustrates the results of such a study at different time points. [77] We can observe that over the course of 60 seconds, a capture flow rate of 10 μL/min only served to marginally contribute to a high capture efficiency [figure 3.8(a)]. We estimate an efficiency of 8-10% solely from the gentle capture flow rate. It is important to note that only 60 seconds of capture was allotted prior to the application of a puncture flow rate of 70 μL/min. We can surmise that capture efficiency may have increased with an extended time given for the flow rate of 10 μL/min. Looking at figure 3.8(b) we also observe no change in efficiency during the wash step, which sought to remove any excess uncaptured cells in suspension over the chip or settled on the non-functional areas of the device. The low aspiration force applied by a 10 μL/min flow rate may not have been strong enough to retain successfully captured cells in the wells. As a result, the efficiency appears

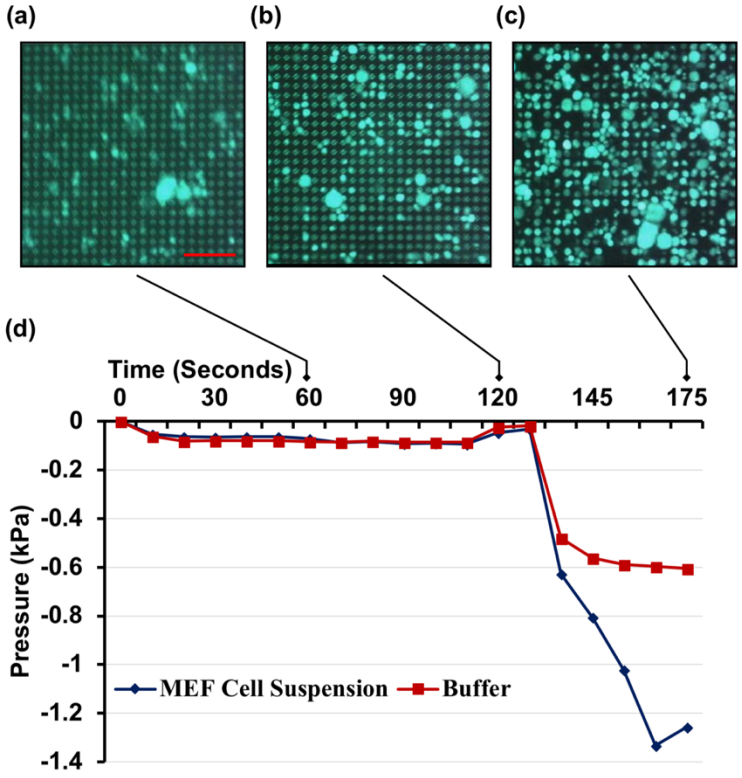

Figure 3.8. Results from preliminary cells testing of the UHT mechanoporation device using MEF cells. (a) Fluorescent micrograph of an array subset taken after the cell introduction stage, using a flow rate of 10 µL/min (scale bar: 100 µm). This image corresponds to the 60 second time point on the pressure vs. time plot. (b) Fluorescent micrograph of an array subset taken after the wash stage at the 120 second time point (flow rate: 10 µL/min). (c) Fluorescent micrograph of an array subset taken after the puncture stage at the 175 second time point (flow rate: 70 µL/min). (d) Comparison of the pressure drop during device operation after the introduction of an MEF cell suspension to standard PBS solution as a means to roughly characterize how the pressure drop during testing may affect cellular viability post-mechanoporation.

to have been maintained at 8-10%, or likely reduced due to unintended dislodging of some captured cells.

Figure 3.8(c) demonstrates the array area after application of a higher flow rate, meant to puncture captured cell membranes, which would allow for delivery of an exogenous payload. We can see a substantially higher capture percentage following this puncture stage, roughly translating to a 75% efficiency. This indicates that the capture and puncture efficiencies, though separate stages in device operation, are inherently dependent on one another. Thus, by optimizing the capture efficiency, we will naturally improve the puncture stage. The large spike in successfully captured cells following the application of the puncture flow rate again confirms the necessity of a more detailed approached towards device parameter optimization. In addition, we hypothesize that initiating a flow rate of such high magnitude prior to adequate capture may expose cells to a higher than necessary puncture force. Cells floating in suspension above the capture array may settle into a site with such high velocity that their subsequent viability may be impacted.

In addition to preliminary confirmation of device functionality using a biological sample, the pressure behavior of the chip was also characterized during this test. With the pressure transducer connected in line to the experimental setup, we were able to record real-time pressure data from the start of the experiment to the end of the puncture stage. Figure 3.8(d) describes the pressure behavior of the mechanoporation device when exposed to MEF cells, and when exposed to control PBS solution. We can see that the chip exhibited similar behavior until the 120-second time point between the cell testing scenario and the control scenario. This can be explained by the relatively low flow rate applied for capture.

The number of cells successfully occupying the capture wells was not at a level where the pressure drop would be significantly different from that of an empty array. Such a result serves to indicate that a 10 μL/min flow rate is not sufficiently strong enough to aspirate a significant number of cells onto the capture wells.

The application of the subsequent puncture flow rate at the 125 second time point led to a substantial deviation between the pressure behaviors of the cell testing scenario and the control scenario. This is explained by the fact that at a flow rate of 70 μL/min, a higher number of cells were now settling into the capture wells, causing a difference in observed pressure. However, rather than observing a flat line of the pressure during the cell test, we see a continual increase. This is due to one of the inherent design limitations of the UHT mechanoporation device: that of a flow rate-based operation, as opposed to pressure-based operation. As more cells begin to occupy the capture wells during the puncture stage, the empty sites exhibit an increase in flow rate due to conservation of mass and the necessity to meet the constant flow rate condition applied on the fluidic circuit. Consequently, not only do cells in suspension impact an open well at a higher velocity, but already captured cells are exposed to larger pressures. We hypothesize that this will increase the potential for cell lysis and reduce cellular viability post-mechanoporation. The implementation of a pressure-based control system that actively modulates the flow rate at the syringe pump to maintain a set pressure point during cell capture may address this limitation in the UHT mechanoporation device.

4. PRELIMINARY FUNCTIONAL CHARACTERIZATION OF THE UHT MECHANOPORATION DEVICE – EL4 CELLS

4.1. Introduction

Following our initial functional confirmation studies in chapter 3, primary objective behind this study was to identify and characterize the main operational parameters associated with UHT mechanoporation device function. We created a rudimentary, and repeatable experimental protocol that would allow us to modularize each stage of device operation: chip preparation, capture, cell introduction, puncture, and release/incubation. This modular scheme of chip testing would lend itself towards partitioned optimization through the variation of a single parameter: the applied flow rate at the syringe pump. With a varied flow rate, we expected changes in capture efficiencies, cell viabilities, and overall device efficiencies. This study applied the minimum capture flow rate of our parameter window, and the maximum puncture flow rate to establish baseline efficiencies. Our conclusions from this data guided us towards areas where we could further optimize device operation and increase the efficacy of the UHT mechanoporation device.

4.2. Materials and Methods

4.2.1. Device Preparation

As described in prior chapters, the UHT mechanoporation device was thoroughly cleaned in Piranha solution (1:1 H_2SO_4:H_2O_2) for one hour. The chip was then rinsed with acetone, isopropanol, and deionized water, and dried with N_2. Following the cleaning step, two PDMS gaskets were laid on each side of the device, and the chip was then coated with gel slick and dried under vacuum. This step was completed to reduce the formation of bubbles beneath the capture array after assembly in the fixture set. The experimental circuit was flushed with 10 ml of 70% ethanol to remove any bacterial contamination using a PhD

Ultra Syringe pump (Harvard Apparatus) operating at a flow rate of 3 ml/min. To remove residual ethanol, the circuit was infused with 10 ml of ultrapure DI water at 3 ml/min. Following this step, the circuit was infused with 5 ml of phosphate buffer saline (PBS), and allowed to soak for the duration of EL4 preparation and staining. For cell capture and release studies, we used a DM2000 fluorescent microscope (Leica) for EL4 visualization and a D5100 digital SLR (Nikon) for imaging.

4.2.2. Cell Preparation and Device Validation Studies

EL4 cells were cultured in DMEM supplemented with 10% fetal bovine serum (FBS) at 36°C and 5% CO_2. Cell concentration per milliliter was found through manual counting using a hemocytometer. An aliquot of cells was removed from the culture flask, centrifuged and resuspended in one mL of PBS prior to cell testing. Cells were stained with 2 μM calcein AM green (Thermo Fisher Scientific) for 30 minutes before the start of capture studies. Cells were then resuspended at a concentration of 1000 cells/μL and captured at a 10 μL/min negative aspiration for three minutes. Prior to the completion of this phase, excess, uncaptured cells were washed and recollected using manual reservoir purging and aspiration. The negative aspiration was maintained during this wash step to ensure that any successfully captured cells would not be dislodged. Using the attached Nikon DSLR, images were taken of all cells captured by each array following the capture stage. To increase the chances of penetration, we applied a 70 μL/min negative flow rate at the syringe pump for 15 seconds. Cells were then released by the application of a positive flow rate of 1000 μL/min for one minute, with images taken over the course of this stage

to illustrate decreasing cell occupation of the capture site arrays. Capture efficiencies were established through visual estimation of the acquired images.

For assessment of device efficiency and delivery efficiency, a similar protocol to that of the capture studies was applied; however, with two key differences. First, the EL4 cells were not pre-stained with calcein green AM. This was done to allow for the use of the green color channel on flow cytometry to calculate delivery efficiency of 4kDa FITC-dextran (Sigma-Aldrich) into punctured cells. The FITC-dextran was diluted to a concentration of 1 mg/ml in 2% FBS/PBS solution, and infused into the experimental circuit. Following the mechanoporation protocol, the recollected cells were washed three times via centrifugation and resuspended in fresh 2% FBS/PBS to remove any remaining dextran in solution. Second, propidium iodide (PI) was added into the cell suspension after the wash stage to assess for cellular viability following mechanoporation. The propidium iodide was incubated with the mechanoporated cell suspension for 15 minutes at a concentration of 1 μg/ml, and the sample was then run through flow cytometry (Cell Lab Quanta SC; Beckman-Coulter).

In addition, three controls were prepared during this test: 1) background – cells aliquoted from the culture flask, resuspended in 2% FBS/PBS and exposed to PI; 2) positive control – cells exposed to FITC-dextran for 30 minutes after plasma membrane permeabilization with saponin; 3) negative control – cells aliquoted from the culture flask, resuspended in 2% FBS/PBS and FITC-dextran for one hour. All three controls were run through flow cytometry to provide a basis of comparison and calculation for UHT mechanoporation device efficiency.

4.3. Results and Discussion

4.3.1. Assessment of Capture Efficiencies and Device Efficiencies

Figure 4.1 illustrates sequential images generated by the DSLR throughout the capture studies. Figure 4.1(a) demonstrates the captured cells along with excess cells prior to manual pipette washing. We can estimate that the chip reached a 60% capture efficiency at this stage of testing. Following manual washing, that efficiency appears to have increased to 75% [figure 4.1(b)]. This can be explained by the fact that any cells washed towards the proximity of vacant sites may have likely been captured, thus adding to the overall efficiency. Figure 4.1(c) illustrates a subset of the capture array 15 seconds after the beginning of the release phase. We can observe a significant decrease in capture site occupancy (~30%) at this point, with the minimum capture percentage reached (~2%) two minutes following the release stage [figure 4.1(d)]. In order for capture efficiency to be truly optimized, a more quantitative method of understanding the number of cells successfully captured by the device is necessary. This method will naturally improve the overall device efficiency.

Though there is clearly apparent localization of cells over the functionally active areas of the UHT mechanoporation chip, it is important to note that no obvious ordered arrangement of cells is discernable. This can be attributed to the low negative aspiration (10 μL/min) applied during the initial capture stage. This flow rate may have been capable of attracting cells down to the surface of the capture array but may not have exerted enough of a force to discretely localize single cells directly above each hemispherical site. As a result, we observe clumped and disordered arrangements of cells on the arrays. In addition,

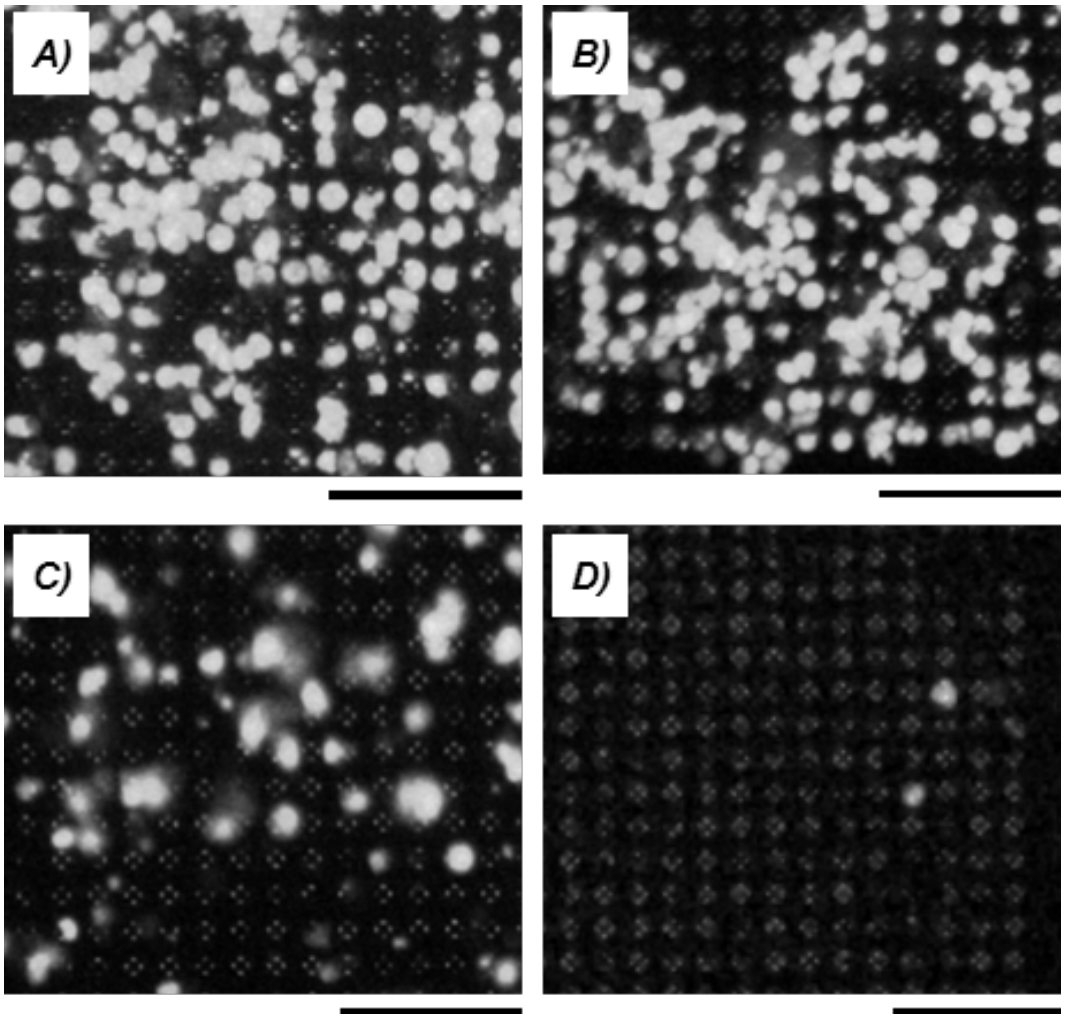

Figure 4.1. Capture testing of EL4 cells. Images taken over the course of a single experiment. (a) Cell capture prior to washing, ~60% site occupancy; (b) Cell penetration step, ~75% occupancy; (c) Beginning of release phase, ~30% occupancy; and (d) End of release phase, ~2% occupancy. Scale bars = 100 μm. Note: backside illumination allowed for visualization of capture wells, while top down illumination allowed for visualization of captured cells (bright white spots).

due to the relative undersizing of the EL4 cells compared to the diameters of the capture wells (i.e. 13.92 $\pm$ 1.54 μm average diameter $\pm$ standard deviation vs. 15 μm capture well diameter), there may have been an occurrence of insufficient cell sealing over a single well. This would result in a leakage flow developed by partially exposed vias, resulting in hydrodynamic drag, and thus cell clumping.

Figure D.1 in appendix D illustrates the flow cytometry results of several of our control studies taken for device efficiency calculations and comparisons with our mechanoporation results. We can see that the background control exhibits negligible auto-fluorescence of cells in both the FITC-dextran regime (Q1) and the PI regime (Q2). This control allowed us to set the boundaries of each quadrant during gating. In addition, our secondary background control with PI [figure B.1(b)] illustrates that the EL4 cells are healthy and exhibit minimal loss in viability prior to mechanoporation (i.e. Q3, PI+, ~1%). The positive control [figure B.1(c)]—cells exposed to saponin and incubated in FITC-dextran for 30 minutes—confirms the capability of our delivery molecule to pass across a permeabilized membrane with high efficiency. We can see little to no shift of cells into any quadrants other than Q1. This control also aided in establishing the vertical axis of our flow cytometry gates.

We were able to calculate the device efficiency of our UHT mechanoporation chip through comparison of Q1 with that of Q1 from our negative control (figure 4.2). Q1 in the context of our mechanoporation data describes cells that have been successfully mechanoporated, exhibit FITC-dextran fluorescence, and are still viable: having excluded the PI that was also in solution. Subtracting the mechanoporation Q1 percentage (14.9%)

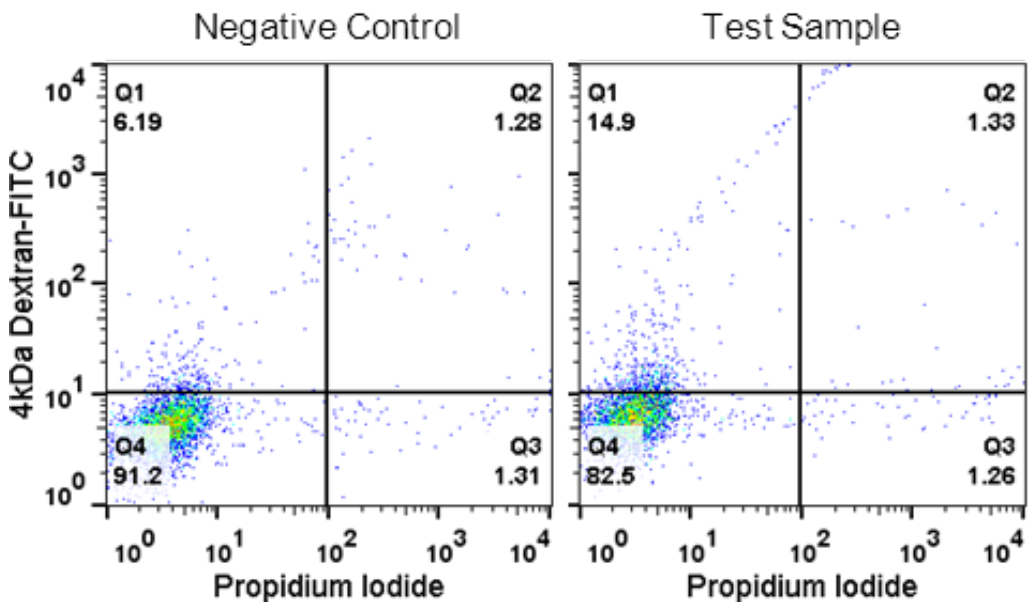

Figure 4.2. Flow cytometry plots for negative control (left) and UHT mechanoporated sample (right). Device efficiency was calculated by subtracting the percentage of events in Q1 of the negative control from Q1 of the test sample. We calculated a total poration efficiency of 8.71%. A minimal effect on viability was also observed, as can be seen from the differences in event percentages in Q4 between the negative control and the test sample.

from the percentage in Q1 of our negative control (6.19%), which accounts for any passive diffusion of FITC-dextran into the EL4 cells over the 1-hour incubation period, we observe an 8.71% device efficiency. While such an efficiency is much lower than desired, it further validates the UHT mechanoporation concept, and follows the results of previous studies at the University of Indiana (appendix A). Moreover, the similar percentages of Q2 and Q3 (PI+/FITC+ and PI+/FITC-, respectively) in both the negative control and mechanoporation sample serve to indicate that the viability of the EL4 cells is unaffected to a significant degree after exposure to the device. As such we hypothesize that further optimization of operational parameters is needed in order to increase the number of cells that have been successfully porated by the device. This points to further study of the capture and penetration flow rates applied during device testing, along with higher efficiency washing steps. Finally, we surmise that a more ideal cell type for testing may be necessary due to the aforementioned sizing inadequacies of the EL4 line.

5. SECONDARY FUNCTIONAL CHARACTERIZATION OF THE UHT MECHANOPORATION DEVICE – K562 CELLS

5.1. Introduction

Based on the results generated from the preliminary EL4 cell studies outlined in chapter 4, we began to further explore various methods to optimize the operational parameters of the UHT mechanoporation device. As previously described, our experimental protocol modularized several key parameters of device operation. Looking at the data from the EL4 studies, we found a necessity to generate a flow rate parameter window that would allow for a more discrete and focused optimization of the capture and puncture functionalities. The parameter window would consist of 5 flow rates, stepped by 10 μL/min. Our capture efficiency would be optimized separately from the puncture efficiency by utilizing one flow rate for each step. In addition, the puncture flow rate would serve to immobilize successfully captured cells during the wash step. This separation of capture and puncture/immobilization flow rates was hypothesized to yield higher efficiencies. In addition, application of other techniques, such as a repeatable method of counting to assess cell capture also aided in improving device operation. This secondary functional characterization significantly aided in better understanding device operation to yield ideal efficiencies.

5.2. Materials and Methods

5.2.1. Chip Assembly

The UHT mechanoporation was first cleaned of all organic matter using a Piranha bath (1:1 H_2SO_4 and H_2O_2) for 3 hours. The device chip was then prepared for testing per the process outlined in chapter 3 (figure 3.2).

The fixture set was placed on the stage of a DM2000 fluorescent microscope (Leica) equipped with a CCD video camera (Imagingsource), and an external high intensity lamp (Leica) [figure 5.1(b)]. This ensured adequate illumination of the UHT mechanoporation device from both sides during cell testing. A PhD Ultra syringe pump (Harvard Apparatus) and a 10 mL glass, gastight syringe (Hamilton), connected via finger tight fittings (IDEX Health and Sciences) and LC tubing (IDEX Health and Sciences) to the fixture set, ultimately completed the aspiration circuit [figure 5.1(a)].

To further ensure the cleanliness of the chip as well as the microfluidic circuitry responsible for device functionality, we manually flushed the system with 10 mL of 70% ethanol to solubilize any contaminants. 10 mL of Nanopure DI water followed by 10 mL of PBS was then used to remove any remaining ethanol within the system. The aspiration circuit was then infused with 3 mL of 30 μg/mL propidium iodide (PI; Sigma-Aldrich) with 1% FBS, and allowed to soak during the time that the cells were prepared for testing. The open reservoir was filled with a starting volume of 350 μL of the PI/FBS/PBS solution. The PI in this solution serves as the delivery molecule for cell poration validation. Propidium iodide classically acts as a cell viability dye. As such, it is incapable of traversing a live cellular membrane, requiring physical membrane perturbation to enter the cytosol. Once inside the cell, it binds to nucleic acids and fluoresces in the red color range. Thus, a successfully punctured cell appeared red.

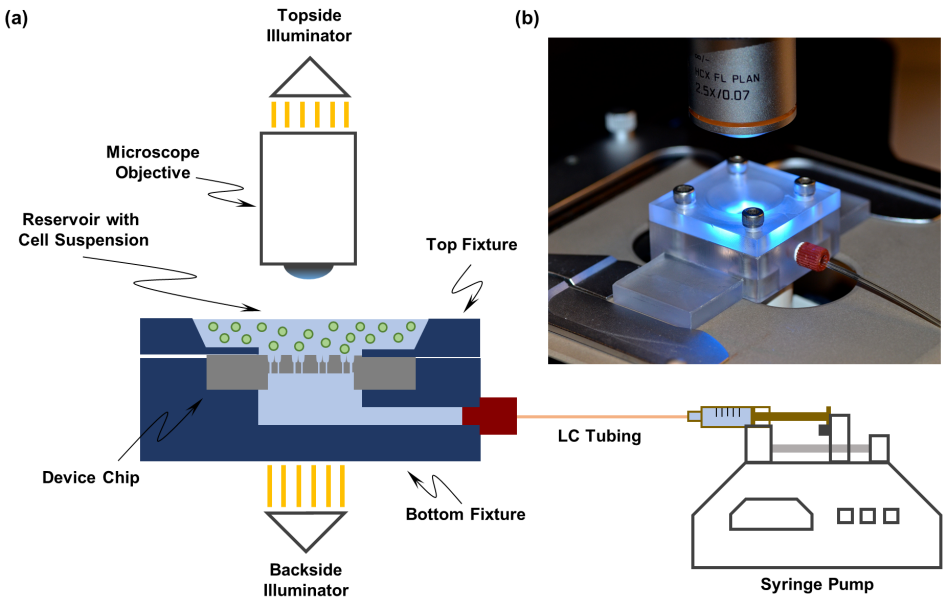

Figure 5.1. Experimental apparatus used for the mechanoporation studies. (a) Schematic illustrating the packaging of the device chip within the fixture, its placement upon the stage of a fluorescent microscope, and its connection to a syringe pump for fluidic actuation of the aspiration circuit. (b) Digital photograph of the packaged device on the microscope stage with the topside illuminator lit.

5.2.2. K562 Cell Culture and Preparation

K562 human leukemia cells (ATCC) were cultured in an upright 50 mL flask at 37˚C and 5% CO2 conditions. We used Dulbecco's Modified Eagle Medium (DMEM; Life Technologies, Gibco) with 10% fetal bovine serum (FBS; Life Technologies, Gibco) and 1% penicillin-streptomycin antibiotic (Life Technologies) as the culture media. Cells were cultured in incubator conditions for 48 hours before refreshing the media. In addition, the population density reached ~$1*10^6$ cells/mL before passaging.

Following initial population counting using a hemocytometer (Fisher Scientific), the K562 cells were stained with 1 mL of 4 μM CellTracker Green CMFDA Dye (Life Technologies) in PBS for 30 minutes. This dye is capable of freely passing through a cell's membrane. Once it has entered the cytosol the dye undergoes enzymatic cleavage, leaving it membrane impermeant, and fluorescent in the green color spectrum. As this dye requires enzymatic cleavage to activate, it classically functions as a live cell stain. Consequently, this staining step allowed for both cell visualization during chip testing and served to negate the effect of dead cells on chip efficiency calculations. Following the 30-minute incubation period, the cells were centrifuged and resuspended in fresh PBS to a concentration of roughly 1000 cells/μL.

5.2.3 K562 Capture Efficiency Optimization

For this series of studies, cells were stained with 4 μM of CellTracker Green CMFDA Dye in PBS for 30 minutes, as described in the previous section. The syringe pump was set to the capture flow rate of choice (at the withdrawal setting) and allowed to

"prime" for 2 minutes. Following this period, cells were added to the array in "bursts" of 5 μL, which converts to roughly 5000 cells per burst. Between 6-7 "bursts" were used for each capture study (30,000-35,000 cells). With the pump still running at the capture flow rate, excess cells were manually washed off with 600 μL of PI/FBS/PBS solution using the open reservoir, and subsequently recollected. On chip imaging was conducted to allow for capture efficiency calculations (imaging conditions: 0.2 second exposure, 750 gain at 5x objective; 1/11 second exposure, 750 gain at 10x objective). Example figures of counted arrays can be found in Appendix E (figure E.1).

To find the capture efficiency for each flow rate study, 10x10 sections of the array were sampled wherein we observed either an occupied well or an empty well for each capture position. Capture data was analyzed on ImageJ. A total of 12 sections of the array were sampled, giving 1200 data points per study. The number of occupied wells was thereby divided by 1200 to give the capture percentage.

5.2.4. Device Efficiency Optimization

Figure 5.2 describes the experimental flow used to optimize the UHT chip efficiency. For this series of studies, cells were again stained with 4 μM of CellTracker Green CMFDA Dye in PBS for 30 minutes, as described in the previous sections [figure 5.2(a)]. The syringe pump was set to the optimized capture flow rate (at the withdrawal setting) and allowed to "prime" for 2 minutes. Following this period, cells were again added to the array in "bursts" of 5 μL [figure 5.2(b)]. Once the array was sufficiently populated (~6-7 bursts), the pump was stopped. The flow rate was then changed to the

"immobilization/puncture" flow rate of choice. Excess cells were washed with 600 μL of PI/FBS/PBS solution using the open reservoir and recollected from the array. Concurrently, successfully captured cells were punctured and kept in place via the "immobilization/ puncture" flow rate.

Punctured cells were released and recollected in PI/FBS/PBS solution, and incubated for 30 minutes [figure 5.2(c)]. The cells were then centrifuged and resuspended in 1 mL of 10 μM Calcein Blue AM (Life Technologies) in PBS and incubated for 30 minutes [figure 5.2(d)]. Similar to the CellTracker Green CMFDA Dye, Calcein Blue AM is capable of freely diffusing across a cell membrane, whereupon enzymatic cleavage will activate its fluorescence and cause it to become membrane impermeant. Only live cells are capable of cleaving Calcein Blue AM rendering this dye a live cell stain.

Lastly, the cells were centrifuged, resuspended in 20 μL of fresh PBS, and added to the hemocytometer for fluorescence imaging [figure 5.2(e)]. The brightfield image acquired after the plating of cells on the hemocytometer served to establish the initial population of recovered cells.

5.2.5. Device Efficiency Imaging and Calculations

To ensure reliable efficiency calculations for the UHT mechanoporation chip, a set of four images were taken per quadrant of the hemocytometer for every "immobilization/ puncture" flow rate studied (figure 5.3). The first image was taken under bright field (imaging conditions: auto exposure, 5x objective), which established the initial cell population density. The second image was taken under green field (imaging conditions:

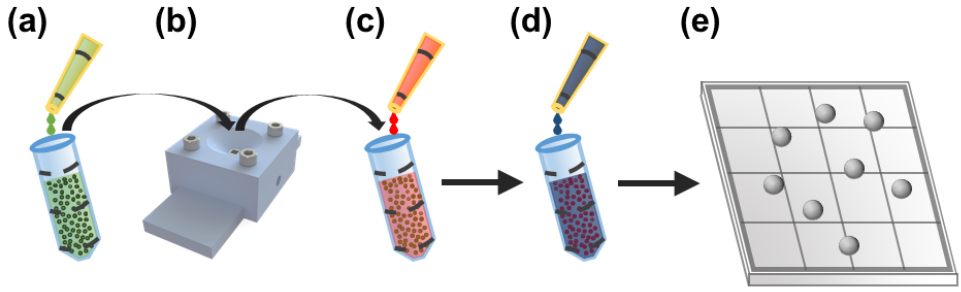

Figure 5.2. Schematic illustration of the multi-color cell staining and counting protocol used for the mechanoporation studies. (a) 30-minute cellular stain with CellTracker Green CMFDA Dye. (b) Cells were then introduced into the device and subjected to the mechanoporation procedure. (c) Incubation in PI solution for 30 minutes following mechanoporation. (d) The cells were then washed, resuspended in Calcein Blue AM, and incubated for 30 min. (e) Finally, the cells were washed, resuspended in culture medium, and counted using a hemocytometer.

1.5 second exposure, 750 gain, 5x objective), which establishes the cell population that was alive prior to the mechanoporation procedure [figure 5.3(a)]. This second image negated any dead cells that may have been captured and punctured from skewing efficiency calculations. The third image was taken under red field (imaging conditions: 1.5 second exposure, 750 gain; 5x objective), establishing the population of live cells (prior to mechanoporation) successfully punctured with sufficient uptake of PI [figure 5.3(b)]. The fourth and final image was taken under blue field (imaging conditions: 2 second exposure, 750 gain; 5x objective), indicating the cell population that remained viable after the mechanoporation procedure [figure 5.3(c)]. To calculate device efficiencies, we counted cells that fluoresce all 3 colors indicating positive initial viability, successful puncture and delivery, and positive viability after the mechanoporation procedure. We divided this number of cells by the initial green population of cells to give the UHT mechanoporation device efficiency.

5.3. Results and Discussion

5.3.1. Optimization of Cell Capture Efficiency

This set of experiments were primarily accomplished to maximize the number of cells that were ideally positioned above each capture well of the chip. From prior studies run using EL4 cells, we concluded that one of the primary limitations in achieving high device efficiency was a low capture efficiency. Three in-line steps were applied in the operation of our UHT mechanoporation device: capture, immobilization/puncture, and release. Optimizing capture to a high efficiency would obviate the need for highly detailed

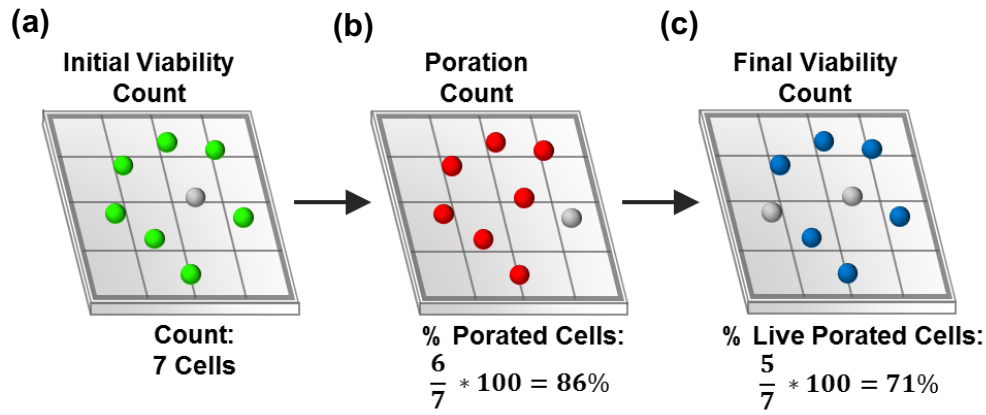

Figure 5.3. Schematic representation of device efficiency calculations. (a) Using the same field of view for all imaging, the initial viability count was first performed by tallying the number of cells stained green (i.e. CellTracker Green positive), to identify only those cells that were viable prior to their introduction into the device. (b) Next, the poration count was performed by tallying the number of cells that were stained both green and red (i.e. both CellTracker Green & PI positive), to identify the subset of initially viable cells that were porated (or killed) during the mechanoporation procedure. Normalization by the initial viability count yielded the % Porated Cells. (c) Lastly, the final viability count was performed by tallying the number of cells that were simultaneously stained green, red, and blue (i.e., CellTracker Green, PI, & Calcein Blue AM positive), to identify the subset of initially viable cells that were porated and maintained their viability afterwards. Normalization by the initial viability count yielded the % Live Porated Cells, which represents the overall device efficiency.

optimization of latter steps. Since manual counting was used to approximate capture efficiency, we applied a condition that no capture well be host to two or more cells occupying the same site. We sought to achieve a high number of individually captured cells, minimal cell clumping, and the lowest possible capture flow rate to ensure maximum cell viability prior to the immobilization/puncture step. As such, we chose to optimize cell capture using the parameters associated with manual cell introduction, variable flow rates, and initial starting reservoir volume.

Over the course of experimental optimization, we were able to establish an optimum starting reservoir volume of 350 μL. Such a volume not only ensured sustained immersion of the UHT mechanoporation device chip over the course of its operation, but also allowed for enough submerged area above the chip to ensure adequate cell dispersion during the capture stage. This dispersion was a necessary factor in reducing the degree of clumping around a single well. Moreover, the cell type chosen (K562 Leukemia cells) furthered increased capture efficiency due to their tight distribution in diameter (~15 μm), as opposed to the slightly undersized nature of the EL4 cells used in previous studies. Such near exact dimensions in comparison to the capture well helped to reduce chances of leakage flow once a cell occupied a capture site. Low leakage flow allowed for uncaptured cells to more likely populate empty capture sites, rather than settle over already occupied wells.

Following an adequate optimization of cell type parameters, maximum capture percentages were now only limited by the capture flow rates applied, and the methods by which the cells were manually introduced into the system. We found that short “bursts” of

a small volume of cells (~5000/5μL) helped to improve the UHT mechanoporation capture efficiency. This technique reduced the number of cells that settled over the "dead space", or non-functional area of the chip. By ensuring sufficient cell coverage in early stage bursts, the effective flow rates of unoccupied wells would increase (by conservation of mass), and naturally lend towards better capture in late stage cell introduction. Finally, by using a cell density nearly 3 times greater than the capacity of the chip, we maximized the odds of population of every capture site. The absence of leakage flow from adequate cell sizing ensured that only one cell would occupy a single well, and thus allowed for a "wash" stage. During this step, excess cells would be removed using manual pipetting without any risk of dislodging successfully captured cells.

Optimization of the capture flow rates focused on maximizing the number of cells captured, while minimizing the degree of "cell dislodging" during the wash steps. Figure 5.4(a) demonstrates the range of flow rates used in experimentation. The plot follows a marked upward trend towards 50 μL/min with a drop off at 60 μL/min. Such a trend can be explained by the necessity for a balance between the operational parameters of the device. A low flow rate, which may maximize cell viability and allow for the largest degree of cell "spreading", still results in a low capture efficiency [figure 5.4(b)]. The slower flow rates (20 and 30 μL/min) do not apply a strong enough force to retain successfully captured cells during the wash step. As the flow rate is increased, the capture efficiency approaches optimum values.

Near the mid-range of our parameter window, cells have ample time to spread homogenously over the functional of the device, while experiencing an aspiration flow that

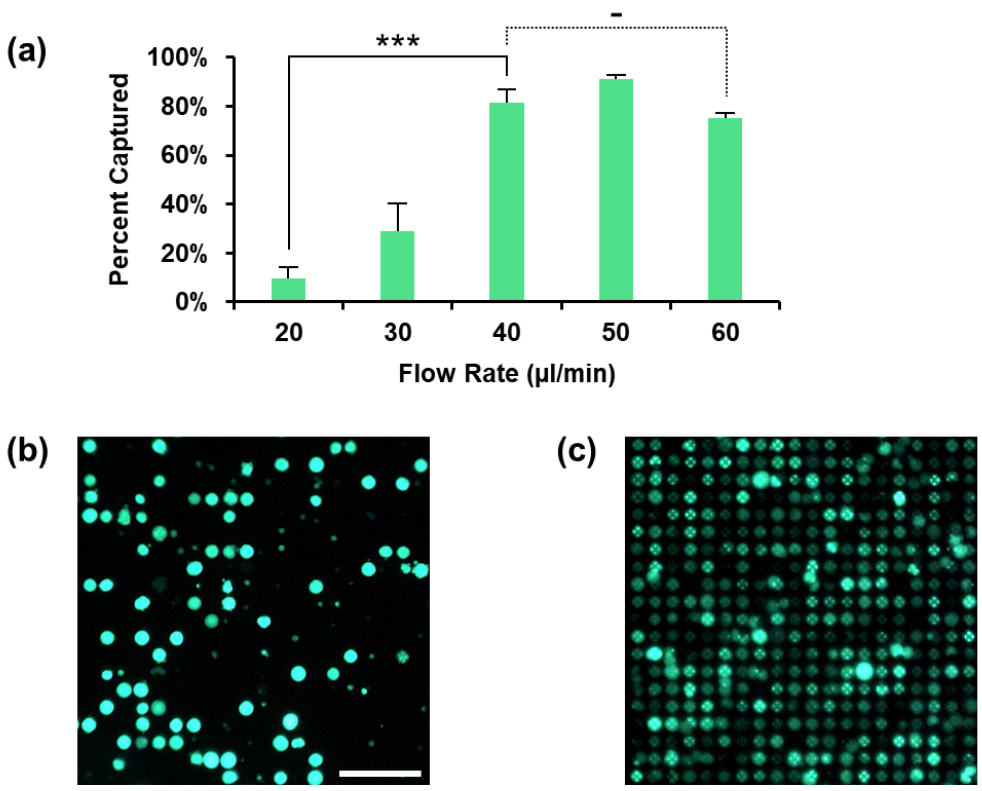

Figure 5.4. Results of capture efficiency optimization study. (a) Plot of capture site occupancy percentage as a function of applied aspiration flow rate [***: $p \leq 0.001$; - : no statistical significance]. (b) Fluorescent micrograph of a portion of the capture site array after capture at 20 µL/min aspiration flow rate. (c) Fluorescent micrograph of the array after capture at 40 µL/min flow rate. The images in (b) and (c) are identical magnification (Scale bar = 100 µm), and only topside illumination was used for imaging. The cells were stained with CellTracker Green prior to their introduction to the device, to allow visualization of viable cells during the capture optimization studies.

will keep them from settling over the non-functional “dead space” of the chip. In addition, these flow rates are strong enough to immobilize captured cells during the wash step, resulting in a well-ordered cell arrangement [figure 5.4(c)]. At a high flow rate, though we did observe moderately high capture efficiency, cellular release proved more difficult. We hypothesize that the non-ideal clover-leaf geometry achieved during our isometric etch process of the hemispherical capture sites resulted in cell “wedging”. The capture flow rate of 40 μL/min resulted in an efficiency of 82% and was applied as our optimum parameter. Though 50 μL/min did yield a slightly higher percentage (90%), the difference between these two flow rates was marginal. As a result, 40 μL/min was chosen to maintain cellular viability without a significant loss of total device efficiency.

Despite the high capture percentages calculated from our studies, there was a disadvantage inherent in the strategy applied. Though we used direct counts of occupied and unoccupied capture wells within each array, these counts were only subsets of the entire array area. Rather than generate a total of 10,000 counts per experiment, we were only able to generate 1,200 as each quadrant was counted with three 10x10 grids at varying locations. As a result, the capture efficiency was approximated rather than calculated using true counts, and the resultant number of successfully captured cells was extrapolated using the approximated percentage. For future work, we looked towards more conventionally accepted and accurate methods to quantify a bulk population of fluorescent cells.

5.3.2. Calculating Device Efficiency Using Hemocytometry

This set of experiments, with the application of our optimized capture flow rate, sought to improve the operational parameters focused on successful cell puncture and payload delivery. In these studies, we utilized propidium iodide as our payload of choice. The concentration of 30 μg/mL was chosen based on concentrations from similar studies, as well as a way to maximize the diffusional driving force into the cytosol.[35] This would ensure an adequate fluorescent signal during device efficiency calculations.

The primary parameter required to achieve maximum device efficiency was the immobilization/puncture flow rate. This flow rate simultaneously acted to restrain captured cells from being washed away, and puncture those captured cells. Depending on the magnitude of the flow rate, we estimate that the membrane pores created from our UHT mechanoporation device measure between 300 – 500 nm (based on the diameters of our microneedle tips). This value falls quite well within the range of reported pore diameters, and is capable of allowing passage of PI into the cell's cytosol.[40] Moreover, our incubation time of 30 minutes was chosen based on complementary times of other poration studies.[33,40,61,78]

The challenge in optimizing the immobilization/puncture flow rate rested in balancing the degree of cell damage rendered by the capture well and ensuring adequate poration to allow for effective delivery. Looking at the SEM images of our array and single capture well, one can see that the geometry digresses from that of our initial concept. The cloverleaf shape observed in the micrographs stems from shortcomings in current microfabrication technology. This clover shape may introduce a danger to cell viability due

to the sharp edges at the corners of each "leaflet". Higher flow rates can potentially shear the cell membrane due to abrasion against these edges both during the puncture stage and the release stage. However, more studies are required to validate this theory.

Similar to our capture studies, we employed the same range of flow rates in optimizing our immobilization/puncture flow rate. Figure 5.5(a) indicates a definite trend in the percentage of live porated cells (our device efficiency), with a maximum value of 42% at 30 μL/min and drop offs on either side of this flow rate. We can reason that at this poration condition, the captured cells experience enough of an aspiration flow to be successfully punctured by the solid microneedle tip and are not so tightly wedged within the non-hemispherical capture well that they lose viability upon release. Lower flow rates illustrate conditions where cells have a decreased risk of deteriorative effects on viability, but do not experience a high enough force to sufficiently porate an appreciable number of cells. Therefore, the total device efficiency decreases. Alternatively, higher flow rates do accomplish larger degrees of poration, but tightly wedge cells into the non-spherical geometry of the capture well. Upon release, these cells may be completely sheared away; thus lowering cell viability and in many cases the number of cells recaptured. Cell micrographs allow for comparisons between staining for immobilization/puncture flow rates of 30 μL/min [figure 5.5(b)] and 60 μL/min [figure 5.5(c)]. One can observe that not only is there a significant difference in cell viability (blue field), but also a difference in the number of cells within the same micrograph area.

Through comparative studies of poration and viability staining, we established an optimized immobilization/puncture flow rate to be 30 μL/min. Moreover, by counting cells

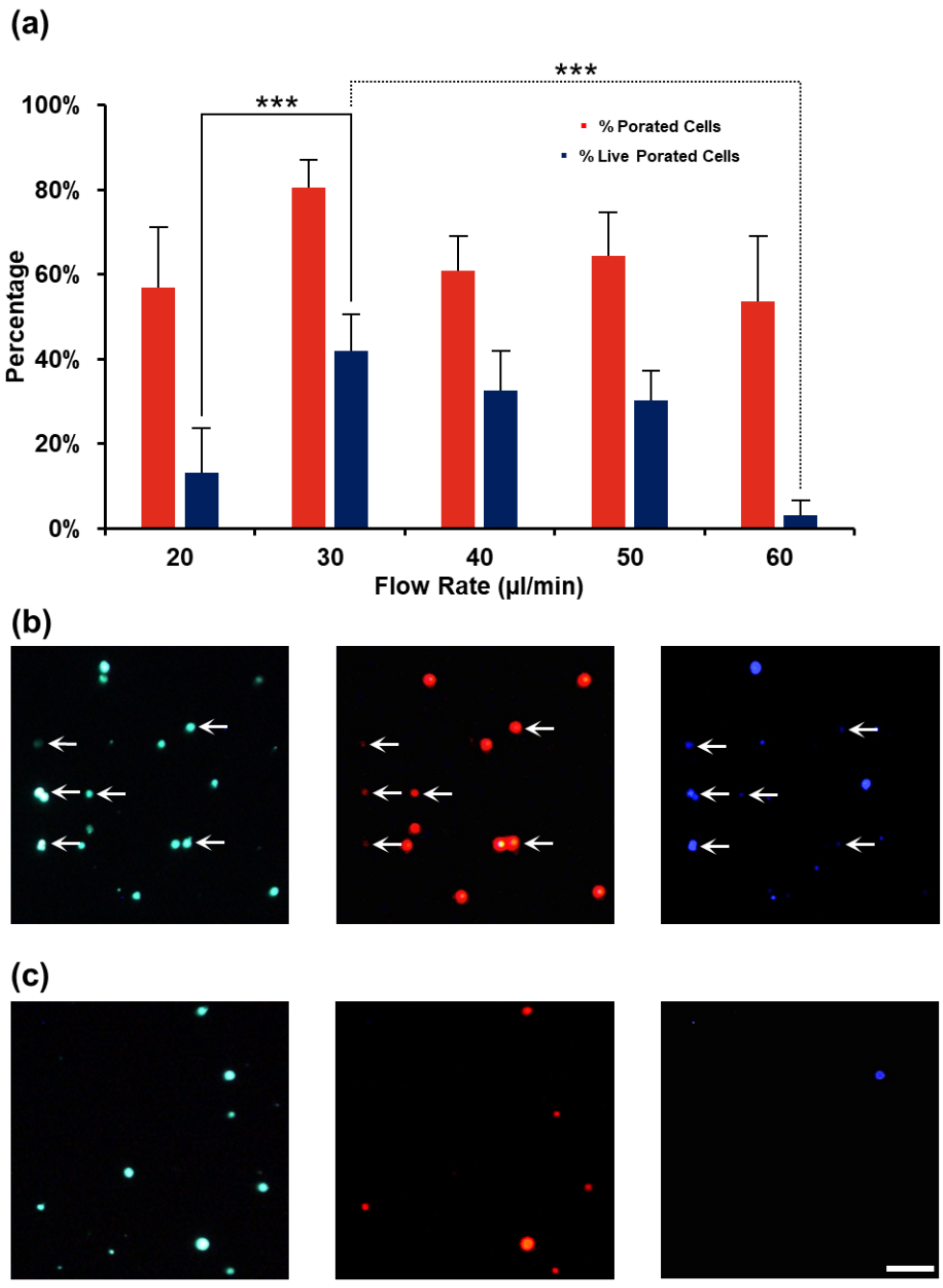
(a)
***
***
100%
80%
60%
40%
20%
0%
Percentage
% Porated Cells
% Live Porated Cells
20
30
40
50
60
Flow Rate (µl/min)
(b)
(c)

Figure 5.5. Results of poration efficiency optimization study. (a) Plot of percentage of porated cells and live porated cells as a function of applied aspiration flow rate. (b) Hemocytometer micrographs of cells collected after mechanoporation at 30 μL/min aspiration flow rate. (c) Hemocytometer micrographs of cells collected after mechanoporation at 60 μL/min flow rate. Within each image series in (b) and (c), the same field of view is shown, and the magnification of all images is identical (Scale bar = 100 μm). As described earlier, the green stained cells (i.e., CellTracker Green positive) are those that were viable prior to their introduction to the device. The red stained cells (i.e., PI positive) are those that were porated (or killed) during the mechanoporation procedure. Finally, the blue stained cells (i.e., Calcein Blue AM positive) are those that were viable after the mechanoporation procedure. Consequently, cells displaying both green and red staining represent the subset of initially viable cells that were porated (or killed) during the mechanoporation process. Normalization of this count by the number of green cells (i.e., the Initial Viability Count) yielded the % Porated Cells data reported in (a). Cells simultaneously displaying green, red, and blue staining (e.g., those marked with white arrows in (b)) represent the subset of initially viable cells that were porated and maintained their viability afterwards. Normalization of this count by the number of green cells yielded the % Live Porated Cells data reported in (a), which represents the overall device efficiency (***: p-value < 0.001).

on a hemocytometer, we calculated that ~9000 cells were recaptured from our optimized experimental parameters. This value measures closely to the number of cells counted in our capture efficiency studies. In addition, this value allows us to translate device efficiency to the number of cells in the population that were successfully porated and still viable. From our highest device efficiency, ~4000 cells were successfully treated by our device. This value serves to indicate the potential impact of the UHT mechanoporation chip in high throughput cell manipulation. Comparably, though most studies report high efficiencies and indicate potential for scalability of their technology, few currently show successfully manipulated cell populations greater than 1000 cells.[35,39,78]

Though these secondary studies served to confirm that the mechanoporation device is capable of delivering exogenous molecules into a cell's cytoplasm, the efficiencies illustrated in figure 5.5(a) are far lower than what is desired. Much of this can be attributed to the necessity for further optimization, covered in chapter 6, but also to the methods by which we assessed for these efficiencies. The sensitivity of a CCD camera was shown to be less than adequate to pick up the fluorescence of a single cell delivered with PI. As such we looked towards methods equipped to be able to accurately assay for PI fluorescence in all cells treated by the UHT mechanoporation device. Moreover, as mentioned in prior sections (5.3.1), the use of a hemocytometer merely allowed us to estimate device efficiencies by generating a concentration of treated cells. In order to truly understand the efficacy of this system, we looked towards methods that could count all the cells recovered from a mechanoporation experiment.

6. OPTIMIZATION OF EXPERIMENTAL PARAMETERS FOR THE UHT MECHANOPORATION DEVICE – JURKAT CELLS

6.1. Introduction

Building off of the efficiencies generated from the optimization studies using K562 cells, we sought to optimize the delivery of functional payloads into our cell models. These studies saw the use of Jurkat cells over K562 cells. Following re-optimization of our primary capture and puncture/immobilization parameters using the new cell model, we created a new experimental protocol to assess the efficacy of our device in transfecting eGFP plasmid. Successful delivery of this functional molecule served to demonstrate that not only do our cells survive short term mechanoporation, but they also are still viable and functional at the 12-hour time point, evidenced by GFP fluorescence. In addition, to more accurately characterize chip function, we applied WEKA segmentation and flow cytometry to calculate our capture and device efficiencies, respectively.

6.2. Materials and Methods

6.2.1. Chip Assembly

Before any testing was conducted, the UHT mechanoporation chip was thoroughly stripped of any organic contaminants by a 1-hour Piranha bath (1:1 H_2SO_4 and H_2O_2, 80˚C). Following the cleaning process, the device chip was lined with 250 μm PDMS gaskets (McMaster-Carr) and placed into the polycarbonate fixture set as described in section 3.2.6.

A BX50 fluorescent microscope (Olympus) equipped with a Retiga EXi *FAST* CCD camera (Q Imaging) was used for the experimental setup, with an external high intensity lamp from Sola Light Engine, Lumencor for cell visualization. Finally, a PhD

Ultra syringe pump (Harvard Apparatus) and a 10-ml glass, gastight syringe (Hamilton) was connected to the fixture using finger tight fittings (IDEX Health and Sciences) and LC tubing (IDEX Health and Sciences) to confer capture and release functionalities to the chip. Before beginning cell testing, the aspiration circuit was manually flushed with 10 ml of 70% ethanol, 10 ml of Nanopure DI water, and 10 ml of PBS. Propidium iodide was infused into the aspiration circuit as specified in section 5.2.1., but at a new concentration of 0.1 μg/mL. A successfully punctured cell would exhibit a rightward shift on a flow cytometry plot as PI intercalates with the DNA of the cell and fluoresces in the red spectrum. Finally, the open reservoir was also filled with a starting volume of 350 μL of PI/PBS solution as done so in prior experimental studies.

6.2.2. Jurkat Cell Culture and Preparation

Jurkat, T lymphocyte cells (ATCC) were cultured in an upright 50 ml flask at 37˚C and 5% CO_2 conditions. We used Dulbecco's Modified Eagle Medium (DMEM; Life Technologies, Gibco) with 10% fetal bovine serum (FBS; Life Technologies, Gibco) as the culture media, and cultured the cells for 48 hours prior to replacing the flash with fresh media. A $1e^6$ cells/mL population density was allotted before re-establishing the cell population to $1e^5$ cells/mL.

We counted a small aliquot of Jurkat cells for viability and concentration using a MUSE cell analyzer (EMD Millipore) at a 1:10 dilution of MUSE viacount stain to cells. A new sample of Jurkat cells were then stained with 1 mL of 10 μM calcein blue AM (Life Technologies) in PBS for 30 minutes. This membrane permeable dye is cleaved via

enzymatic processes and is then localized only within live cells. Calcein Blue AM fluoresces in the blue color spectrum. Using calcein negated any dead cells from skewing capture efficiency calculations and allowed for convenient visualization of live cells during device testing. We used a concentration of 500 cells/μL in PBS for our device testing after the 30-minute staining period.

6.2.3. Jurkat Capture Efficiency Optimization

Following preliminary live cell staining with calcein blue AM, we "primed" the syringe pump at the capture flow rate of choice for 5 minutes. A total of 20,000 cells were added to the array during the capture studies in aliquots of 2500 cells/5 μL. Manual washing with 700 μL of PI/PBS solution and the application of an immobilization flow rate identical to the capture flow rate removed excess, uncaptured cells from the array. Flow rates of 20-60 μL/min over an interval of 10 μL/min were applied for the capture efficiency optimization tests. Each flow rate experiment was conducted in triplicate in order to allow for statistical analysis using a standard student's t-test. On chip imaging was conducted to calculate the capture efficiency for each applied flow rate, in 8-bit mono grayscale format. The exposure of each image was taken based on the degree of fluorescence observed per test. All exposure times and settings were maintained between arrays within each test; however, were varied between studies.

6.2.4. Capture Efficiency Characterization using the WEKA Segmentation Method

Capture efficiency was characterized using the WEKA segmentation plugin for the Image Processing and Analysis in JAVA (ImageJ) program. All 4 quadrant images from each test were first cropped to the boundaries of the array, to remove excess black background [figure 5.1(a)]. The array exhibiting the smallest degree of cell clumping was chosen as the master classifier. Cells were first segmented from the black background using this "master" array, and the settings were then applied across the entire experiment for all 3 remaining arrays. This process was repeated for each test. Due to variations in exposure conditions between each test, one single master classifier could not be used. As such, in an effort to maintain as much objectivity as possible, one master classifier was used per test. This totaled to 12 master classifiers for the entire triplicate study. Following segmentation of each array, using the respective master classifier, the results were outputted into binary green/red color images [figure 5.1(b)]. These images were then converted to 8-bit grey scale images. The final conversion step was to process the 8-bit figures into binary black/white images, with cells representing the black portions of the images, and the background representing the white portions of the images [figure 5.1(c)].

ImageJ's built in "analyze particle" program allowed for automated and consistent counting of captured cells, and exclusion of large cell clumps, across all 60 array images following WEKA segmentation. The optimal parameters applied for this stage of cell counting involved using a range of 20-120 square pixels as ideal cell sizes [figure 5.1(d)]. All particles below 20 square pixels were defined as cell particulate matter, and particles above 120 square pixels were defined as cell clumps and could not be counted as

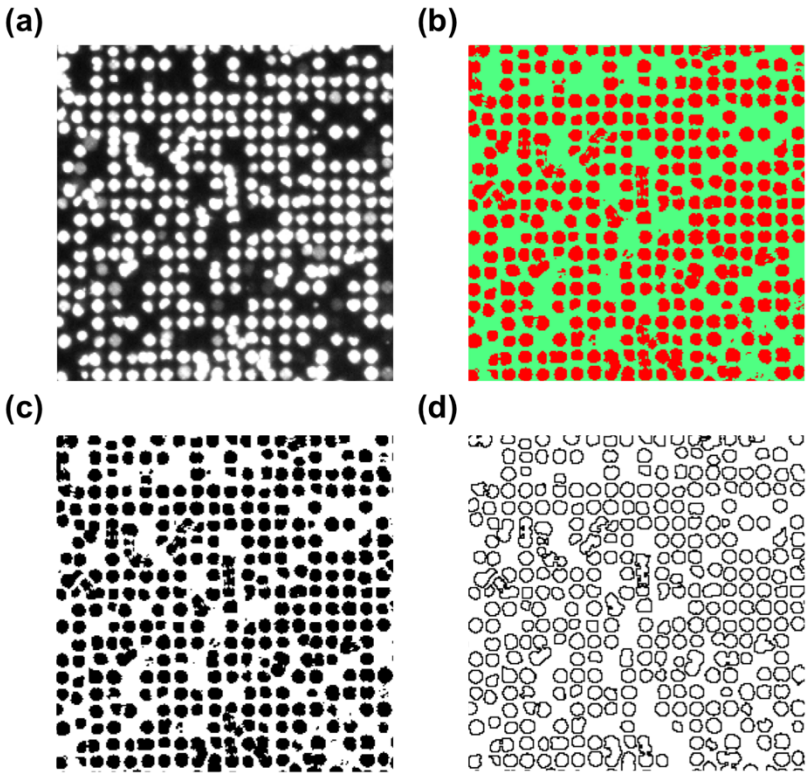

Figure 6.1 Visual progression of WEKA analysis on a capture array following cell capture during mechanoporation. Only a subset is shown for ease of visualization (a) The capture array is first imaged using the attached CCD camera on the upright fluorescence microscope in monochrome format, then cropped to the appropriate boundaries. (b) Each image is classified using ImageJ's built-in WEKA segmentation program and outputted as a binary red/green image (red representing cells). (c) The WEKA output is converted into a binary black and white image with black representing cells. (d) Using the particle counting plug-in, successfully captured cells are counted based on an assigned threshold and a visual output is given by an outline representation of counted cells.

successfully "captured" cells. The results were then tabulated, and total capture efficiencies were calculated as the number of cell counts divided by 10,000, yielding a true capture efficiency. This procedure allowed for exact capture percentages as opposed to percentages that were given using counts of subsets of entire arrays, as detailed in prior methods (see chapter 5).

6.2.5. Device Efficiency Optimization

For optimum cell visualization, Jurkat cells were stained with 10 μM of Calcein Blue AM for 30 minutes in PBS, as described in the previous sections and resuspended in 4% glycerol in PBS. We applied the optimized capture flow rate of 30 μL/min for 5 minutes to allow for the syringe pump to "prime". Jurkat cells then were added to the open reservoir at a concentration of 500 cells/μL in volumes of 5 μL (2500 cells). This was repeated a total of 8 times, which corresponded to 20,000 cells introduced to the device array. Excess, uncaptured cells clumped above the capture array or localized within the non-functional area of the device were removed with 700 μL of PI/PBS solution. Captured cells were simultaneously punctured and kept in place by the application of an immobilization/puncture flow rate of choice.

Successfully captured and punctured cells were then released from the device array and recollected in the PI/PBS solution. This sample was then co-stained with 1 μM of CellTracker Green CMFDA Dye (Life Technologies) for 30 minutes. CellTracker Green CMFDA Dye uses a similar enzymatic cleavage scheme to Calcein Blue AM, wherein live

cells cleave a portion of the dye's structure, rendering fluorescence. As CellTracker Green relies on enzymatic activity, it is thus a live cell stain.

In tandem, two controls were also applied to account for passive diffusion of the fluorescent molecules, as well as baseline characterization of Jurkat cell viability. Control 1 co-incubated cells in 0.1 μg/mL of PI and 1 μM of Cell Tracker Green in PBS for 30 minutes, serving as a "positive control". Control 2 incubated cells in only PBS for 30 minutes, serving as a "negative control". Both sets of cells were first exposed to 4% glycerol solution for 7 minutes to assess any deteriorative effects of this solution on cell viability. In addition, these controls were used to establish forward scatter, side scatter, and fluorescent gating during flow cytometry.

Our sample was then washed of all stains and resuspended in 100 μL of FACS stain solution (0.5 NaN_3, 500 ml HBBS; Gibco), and assayed using flow cytometry (MACSQuant Analyzer).

6.2.6. Experimental Setup for Transfection of eGFP Plasmid

Jurkat cells were pre-stained with 4 μM of Calcein AM Red Orange dye (based one literature precedent) in PBS for 30 minutes, centrifuged, and resuspended in 4% glycerol in PBS.[79] The experimental setup was infused completely with eGFP plasmid in PBS at a concentration of 20 μg/mL. The syringe pump was set to the optimized capture flow rate of 30 μL/min and allowed to "prime" for 5 minutes. Cells were then added to the fixture reservoir as described in previous sections and chapters. However, as opposed to a PI/PBS solution, excess cells were washed with 700 μL of the eGFP/PBS solution while the

optimized immobilization/puncture flow rate of 40 μL/min was applied. Concurrently, successfully captured cells were punctured and kept in place from the "immobilization/puncture" flow rate. Punctured cells were released and recollected in eGFP/PBS solution, and allowed to recover via a 30-minute incubation.

Following the incubation period, the sample was centrifuged and resuspended in 1500 mL of RPMI media (Lonza) supplemented with 10% FBS, and 0.5% penicillin streptomycin in a 24 well culture plate (Lonza). The sample was then placed in a cell incubator at a 37˚C with 5% CO_2 for a period of 12 hours. Following the long-term culture period, the sample was then centrifuged and resuspended in 1000 μL of PBS solution and stained with 8μM of Calcein Blue AM for 30 minutes. The sample was centrifuged again, resuspended with 100 μL of FACS stain solution (Life Technologies) and run on flow cytometry. The green, FITC channel on the MACSQuant machine was used to characterize delivery efficiency of the GFP plasmid, and the VioBlue channel was used to assess cellular viability.

We used two controls during the eGFP plasmid transfection tests to account for passive diffusion of the plasmid constructs, as well as any background fluorescence of the Jurkat cells. For the passive diffusion controls, Jurkat cells were first exposed to 4% glycerol solution for 7 minutes to match the experimental conditions of the mechanoporated cells as closely as possible. We then incubated this control in eGFP plasmid at a 20 μg/mL concentration in PBS for 30 minutes. The sample was then centrifuged and resuspended in RPMI culture medium with 10% FBS and 0.5% penicillin/streptomycin and incubated in tandem with the mechanoporated cell sample for

12 hours in a 24-well culture plate. Following the incubation period, the control sample was stained with 8 μM of Calcein Blue AM for 30-minutes, then resuspended in 100 μL of FACS stain solution, and utilized to establish forward scatter, side scatter, and fluorescent gating during flow cytometry. The last control, used to monitor for autofluorescence of Jurkat cells was merely an aliquot of stock cells incubated in similar culture conditions with the positive control and mechanoporated sample. No staining was completed for this control.

6.2.7. Electroporation Control Studies

To provide for comparisons to gold standard techniques for cell delivery, we ran studies using electroporation as a benchmark for delivery efficiency, cell viability, and delivery yield with eGFP plasmid as the payload. We used the standard Lonza Nucleofector kit for Jurkat cells (Lonza, DSMZ ACC 282, cryopreserved; VCA-1003). $1e^6$ Jurkat cells were aliquoted from the stock culture flask and suspended in 82 μL of nucleofector solution V and 12 μL of supplement for a total volume of 100 μL. 2 μg of eGFP plasmid was added to the solution. The sample was placed in a cuvette and electroporated with the X-01 program on the electroporation instrument. We removed the sample from the cuvette and immediately resuspended the cells in 1500 μL of RPMI media with 10% FBS and 0.5% penicillin/streptomycin. The samples were incubated for 12 hours in a 24-well culture plate at 37˚C and 5% CO_2 in a standard incubator. DAPI was used at a 20% concentration following the 12-hour incubation period, and the samples were run on flow cytometry in FACS stain solution to assess for viability and delivery efficiency. A passive diffusion

control was also applied to this study by exposing stock Jurkat cells to the eGFP plasmid for 1 minute in PBS, then resuspending in fresh media and culturing for 12 hours. In addition, a control for autofluorescence was also used.

6.2.8. Delivery Efficiency and Device Yield Analysis

Percentages for delivery efficiency, delivery yield, and transfection efficiency were calculated using the number of events in several various flow cytometry plots. In addition, these percentages were calculated in a similar manner to that reported in other cell delivery studies. [Chang Lu, J of Controlled Release] Such calculations were based on the following equations:

Eq. 6.2.6.1. $$Delivery\ Efficiency\ (\%) = \left(\frac{R}{V}\right) * \ 100$$

Eq. 6.2.6.3. $$Cell\ Viability\ (\%) = \left(\frac{V}{T}\right) * 100$$

Eq. 6.2.6.3. $$Delivery\ Yield\ (\%) = \left(\frac{R}{T}\right) * \ 100$$

Where R = the number of cells expressing PI;

V = the number of viable cells (cells with cell tracker green staining);

T = the total number of cells observed via flow cytometry.

The initial population of Jurkat cells (T) were established using the forward and side scatter plot. This population was then plotted across side scatter vs. cell tracker green. Cells fluorescing in the green spectrum (V) were marked by a rightward shift on the plot. These

cells were gated and plotted across side scatter vs. propidium iodide. Cells fluorescing in the red spectrum (R) were marked by a rightward shift on the plot.

6.3. Results and Discussion

6.3.1. Assessment of Cell Capture Efficiency

The capture studies conducted using K562 cells in the previous chapter provided the basis for re-optimization of the capture operational parameters with the new Jurkat cell type. Again, we tuned the parameters associated with manual cell introduction, and variable flow rates. However, a 350 μL reservoir volume was maintained as qualitative results indicated that this parameter need not be changed simply from the application of a new cell line. Our basis for what constituted optimal capture was also identical to prior studies: single cell well occupation, minimal clumping, and lowest possible applied flow rate. We found that a total cell density of 20k, double the capacity for the UHT mechanoporation array was optimal for Jurkat cells. This maintained the use of a wash stage and ensured maximum capture site occupation.

Figure 6.2(a) presents the capture efficiencies for each flow rate parameter applied in the capture optimization study. Much like the results from the K562 cell capture studies, the current plot reaches a maximum efficiency at 30 μl/min with a minimum at 60 μl/min. We surmise that at 30 μL/min, the strength of the aspiration flow is enough to successfully capture a single cell in the capture well, maintain its position during the wash stage, but is not so aggressive as to wedge or shear the cell through the aspiration vias [Figure 6.2(b)]. We hypothesize that such shearing and wedging effects are the cause of the lower capture

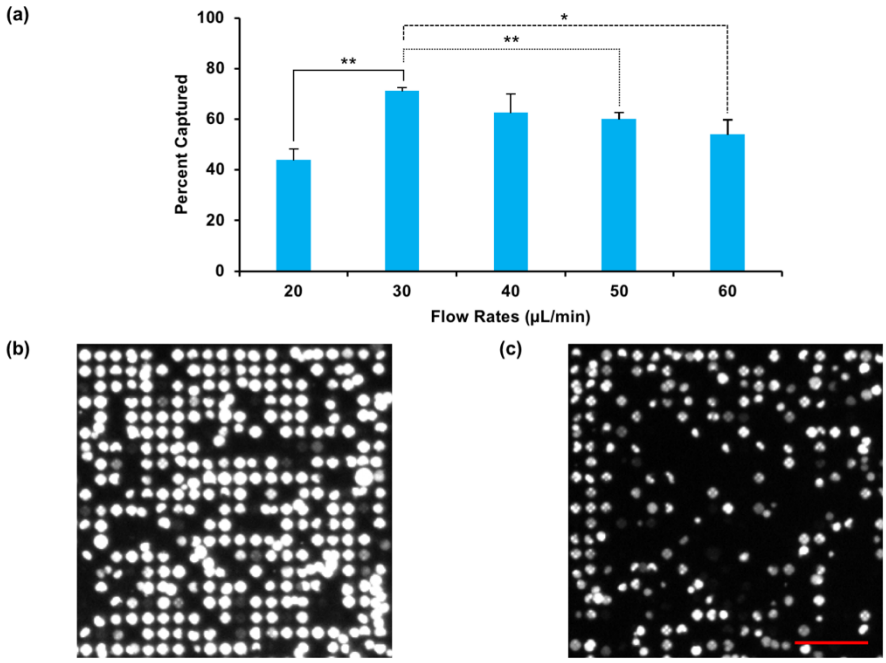

Figure 6.2 Results of the capture optimization studies using Jurkat cells. Cells were pre-stained with 10 µM of Calcein Blue AM to allow for on chip visualization and image generation during device testing. (a) Capture efficiencies in triplicate across the parameter window demonstrate that the optimum flow rate for Jurkat capture is 30 µL/min [*: $p \leq 0.05$; **: $p \leq 0.01$; *** $p \leq 0.001$]. (b) Lower flow rates, such as the optimum 30 µL/min yield an ordered arrangement of cells, with typically one cell positioned directly above one capture well. Some clumping is still apparent at lower flow rates, and these areas were not counted as successfully captured cells during WEKA segmentation. (c) Higher flow rates, such as 60 µL/min are much more aggressive, and may result in some ordered arrangement, but likely cause cell shearing through the capture array due to the high pressure-drops incurred from a system that cannot maintain a standard pressure as the array becomes increasingly occupied. Scale bar: 100 µm.

efficiency at the maximum flow rate (60 μL/min) [Figure 6.2(c)]. While an ordered arrangement is observed, a low overall population of the array is apparent. The low Calcein Blue AM intensity apparent in certain captured cells may be due to efflux after membrane puncture. Thus, the capture flow rate of 30 μl/min, which resulted in an efficiency of 71%, was applied as our optimum parameter.

It is important to note that capture efficiencies were calculated by direct counts of captured cells using WEKA segmentation on ImageJ. This method adequately addressed many of the shortcomings inherent to our prior technique of assessing capture efficiency. At optimum flow rates, our device thus successfully captured ~7100 suspended cells, a throughput orders of magnitude higher than current cell capture techniques.[34,35,38,39,58]

Our studies using both the K562 and Jurkat cells demonstrate how the functionality of the UHT mechanoporation device with respect to capture transfers between multiple cell types. The similarities between optimum capture efficiencies as well as the general trend within the parameter window may indicate that this chip need only be optimized once for application across cell models that have relatively similar physical characteristics (i.e. culture type, and relative size). For cells that significantly deviate from K562s or Jurkats in physical characteristics, this transfer of optimum parameters may not be possible, though no tests have been conducted to confirm this hypothesis.

6.3.2. Assessment of Cellular Viability and Device Efficiency Using Flow Cytometry

Our efforts to maximize the cellular viability and device efficiency of the UHT mechanoporation chip centered on improving cell puncture by optimizing the associated

operational parameters. Much like our studies with K562 cells, we utilized propidium iodide (PI) as our delivery molecule using a concentration of 0.1 μg/mL with a 30 minute incubation, which were experimental factors based on similar studies.[33,35,50,61,78]

Figure 6.3 represents flow cytometry results typical of our control studies. We established our base Jurkat population within our mechanoporation sample using the forward and side scatter plots for the positive control [figure 6.3(a)]. In addition, based on our secondary control data [figure 6.3(b)], we can safely conclude that the rightward shifts in cell tracker green, indicative of cellular viability, is not affected by autofluorescence.

The third set of plots in both figures 6.3(a) and 6.3(b) represent the proportion of viable Jurkat cells that exhibit red fluorescence, via propidium iodide. Our control studies indicate no shift in the red spectrum. This serves to demonstrate that PI exhibits minimal passive diffusion (<5%) into a highly viable cell population. Moreover, Jurkat cells express negligible background fluorescence within PI's fluorescence wavelength. We can therefore conclude that any shift in the mechanoporation plot must therefore be from the delivery of PI molecules via transient membrane pores created by the UHT mechanoporation device.

Figure 6.4(a) illustrates the results of our mechanoporation testing using flow cytometry. The delivery efficiency shown in Figure 6.4(b), which is calculated from the number of cells expressing propidium iodide among the total viable cell population is consistently high across all of the applied immobilization flow rates. These consistent efficiencies are explained by optimized capture parameters. One optimized capture parameter includes cell capture with a unique and constant flow rate for all delivery efficiency optimization tests. Additionally, an initially large population of cells available

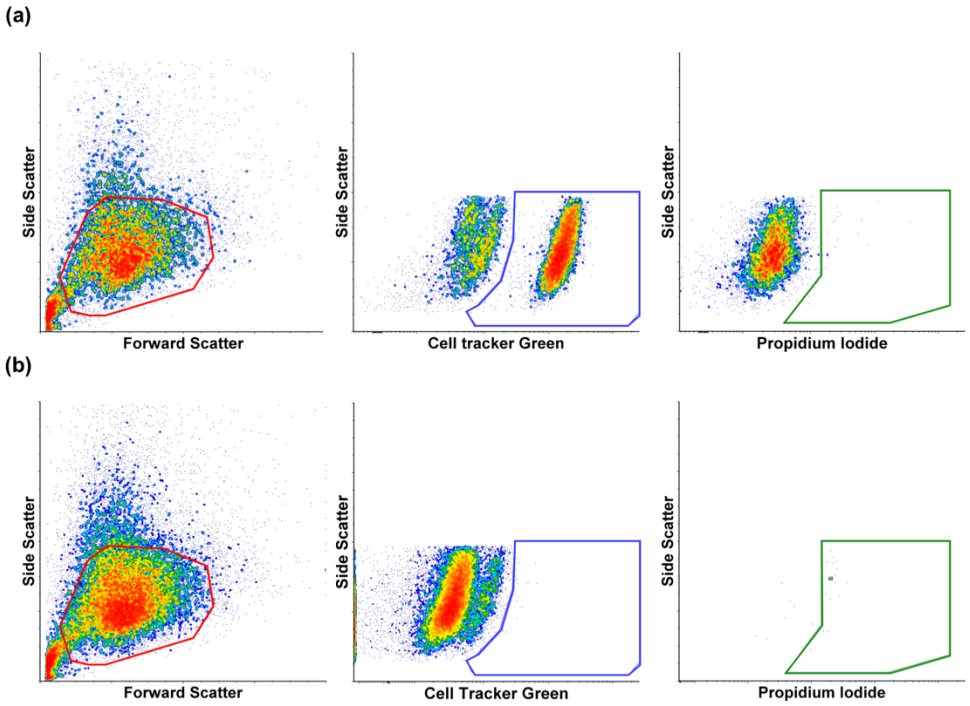

Figure 6.3. Flow cytometry plots of representative controls studies used during the optimization of device parameters to maximize device efficiency. (a) Positive control used to assess passive diffusion of propidium iodide into Jurkat cells. Cells were incubated in 0.1 µg/mL of PI solution for 30 minutes, and then stained with cell tracker green at a concentration of 1 µg/mL to assess for viability drop solely from the time exposed to PBS solution. We can observe a moderate drop in viability simply from time, as well as no passive diffusion of propidium iodide into live cells. (b) Control used to assess autofluorescence of cells on the green and red channel along with as assessment of cellular viability after exposure to 4% glycerol for seven minutes. Viability was assessed using DAPI (not pictured) and demonstrated a minimal loss in cell life with glycerol exposure.

for puncture allows for high delivery efficiencies across the whole immobilization flow rate parameter window. Moreover, the comparison of delivery efficiency of the sample to the control confirms that the influx of PI is primarily caused by the UHT mechanoporation chip creating transient membrane pores in each captured Jurkat cell.

We can study the effect of the device on cellular viability from figure 6.4(b). It illustrates a marked decrease in viability across the whole parameter window. While some of the apparent low viabilities may be attributed to low starting viabilities prior to testing (Appendix F), such as for the 20 μL/min or 60 μL/min parameters, others are most likely brought about due to the aggressive nature of our device. Without a discrete means of controlling the large pressure drop across the device array as it is increasingly occupied, there is a higher chance of cellular death during the capture and puncture phase. In addition, such a high pressure may lead to cell wedging within in the capture well, necessitating a large release flow rate that may cause cell shearing and a resultant low delivery yield, as is shown in figure 6.4(c).

Figure 6.4(c) illustrates the delivery yield for the UHT mechanoporation device. The delivery yield is the total number of viable, PI expressing cells, out of the total Jurkat cells in the sample population. We observe a positive trend to 30 μl/min, a flat line through 50 μl/min and a distinct drop at 60 μl/min. We find that the delivery yield is nearly half that of the delivery efficiency, indicating that while the UHT mechanoporation chip successfully treats Jurkat cells, the total number of cells treated is still sub-optimal. Further

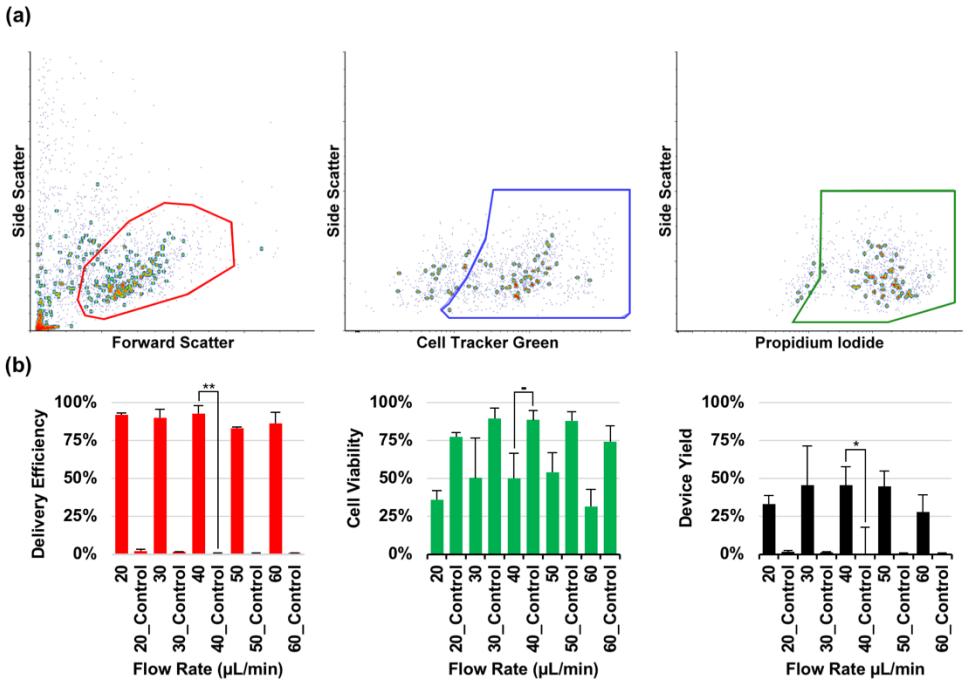

Figure 6.4. Results from triplicate UHT mechanoporation device optimization studies. (a) Representative flow cytometry plots for the optimum flow rate applied (40 µL/min). Gates were established using associated control plots. (b) Statistical comparisons of the average delivery efficiency, cell viability, and device yield to the positive control sample. We can observe high delivery efficiencies across the entire parameter window along with maximum cellular viability for the mid-range flow rates. The optimum efficiency, when compared to 30 µL/min, is observed at 40 µL/min due to a narrow standard deviation for the device yield. [**: $p \leq 0.01$; *: $p \leq 0.05$; -: no statistical significance].

device development is thus necessary to increase the delivery yield. Combining the efficiencies from Figures 3(a), 5(a), and 5(b), we can see that in its current state, the optimum operational parameters of the UHT mechanoporation device are a 30 µl/min capture flow rate and a 40 µl/min immobilization flow rate. The variability in delivery yield of the 30 µl/min flow rate discourages its application as an optimum parameter. The t-tests applied indicate little to no statistical significance between 30-50 µl/min, and may indicate that the differences between each parameter are not aggressive enough to warrant a significant variation in delivery yield.

6.3.3 Transfection of Functional Molecules Using Optimum Operational Parameters

To characterize the viability and functionality of mechanoporated cells beyond the 30-minute incubation window, we applied the optimum operational parameters (30 µL/min capture, 40 µL/min puncture) to the transfection of eGFP plasmid, figures 6.5 and 6.6. Following a 12-hour incubation time, we assessed the degree of fluorescence via flow cytometry for our mechanoporated sample as well as our controls. Our forward/side scatter gates, GFP gates, and Calcein Blue AM gates were establish using the positive control [figure 6.5(a)]. We can observe a minimal degree of passive diffusion of GFP into a highly viable population of cells, along with negligible autofluorescence on both the green and blue channels [figure 6.5(b)].

The delivery efficiency of our mechanoporation sample was calculated by dividing the number of events indicating positive green fluorescence in gate 3 by the number of events within gate 2, the viable cell population [Figure 6.6(b)]. Our results indicate a 97%

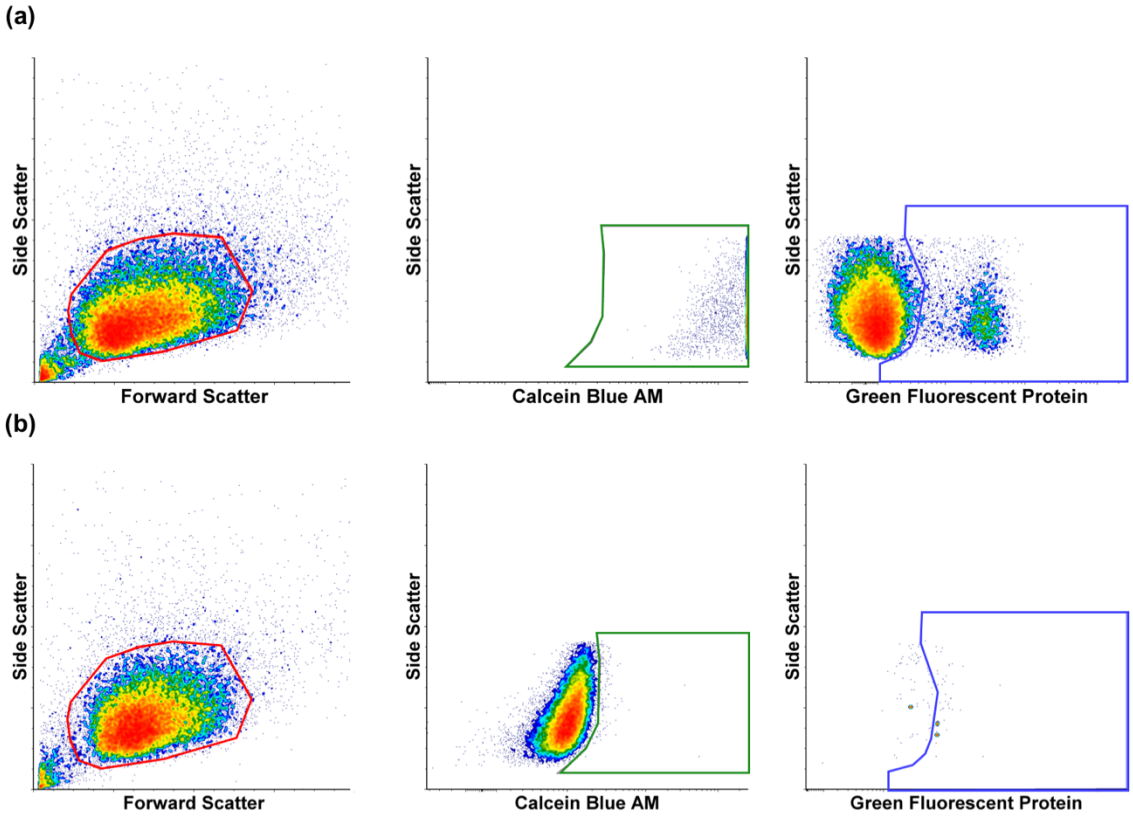

Figure 6.5. Flow cytometry plots for the eGFP transfection controls. (a) Positive control used to assess the degree of passive diffusion of eGFP plasmid into Jurkat cells without mechanoporation, as well as the effect of 4% glycerol exposure on cell viability. (b) Autofluorescence control used to ascertain the extent of inherent Jurkat fluorescence the blue and green channels. These control were used to establish proper gating for the subsequent mechanoporation sample.

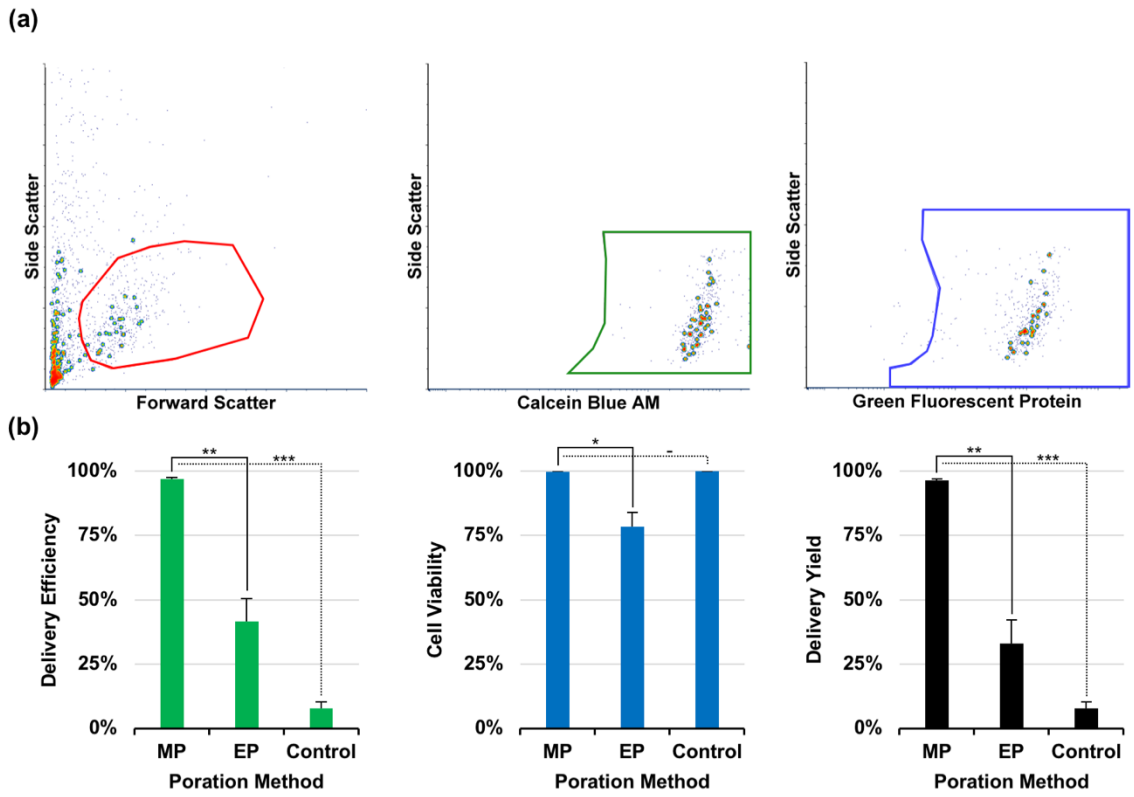

Figure 6.6. Results of the long term eGFP plasmid transfection mechanoporation study. (a) Representative flow cytometry plots for the optimum device operational parameters (30 µL/min capture, 40 µL/min puncture/immobilization). Gating for these studies was established using the controls. (b) Quantified results of these studies in comparison to electroporation and control samples [***: $p \leq 0.001$; **: $p \leq 0.01$; * $p \leq 0.05$; - : no statistical significance].

delivery efficiency of eGFP plasmid through the mechanoporation procedure. In comparison to the standard Amaxa kit electroporation protocol, the UHT mechanoporation device is more efficient (42% vs. 97%).[80] This superiority is also apparent in both the 12-hour cell viability [figure 6.6(b)] as well as the delivery yield [figure 6.6(c)]. The increase in cell viability of our long-term sample in comparison to the results from section 6.3.2 serve to indicate a recovery of our cells by exposure to standard culture conditions. Though our delivery yield is larger than both the EP studies and our control, it is important to note that the number of cells recovered from our testing was far lower than that of electroporation. This result indicates that certain limitations inherent to device design need to be addressed in order to realize maximum efficiencies. Flow cytometry plots of the benchmark electroporation studies can be found in Appendix F.

6.3.4 Competitive Landscape of Cell Manipulation Technology and Comparison of Recent Technologies to Current UHT Mechanoporation Device Efficiencies

The impact of the UHT mechanoporation device can be put into perspective through the study and understanding of competing technologies that seek to deliver similar molecules and large payloads into transiently porated cells. The vast field of cell manipulation has led to the creation of several forms of competitive technologies focused on transient membrane poration. However, for the ease of comparison, we can distill these technologies into 3 primary forms: squeeze/shear poration, electric field poration, and acoustic field poration.

6.3.4.1 Squeeze/Shear Poration Competitive Landscape

Within squeeze/shear poration, the leading technology, known as squeeze cell poration (SQZ), uses a network of in-line microfluidic channels with constrictions midway. Cells are flown through these channels, and when a cell approaches a constriction, it is deformed. This leads to the generation of transient membrane pores that allow for delivery of an exogenous payload through passive diffusion. Such technology has previously reported the successful delivery of small fluorescent molecules and siRNA.[44]

Recently, this technology has also shown efficient delivery of large molecules, namely GFP plasmids.[81] Much like UHT mechanoporation, SQZ has the advantages of high throughput, scalable design, and ease of manufacturing. However, it is limited in its large molecule delivery by the necessity of an electric filed to establish a charge gradient. This gradient "drags" large charged molecules, such as plasmids, towards the porated cells. The UHT mechanoporation system has demonstrated successful delivery of GFP without the use of an external field. In addition, as opposed to a trade-off of < 80% cellular viability for > 90% transfection efficiency in SQZ poration, the UHT mechanoporation system has demonstrated > 90% transfection efficiency and cellular viabilities.[81] In addition, SQZ poration's disadvantage of clogging (which can reduce throughput) is not reflected within the UHT mechanoporation device. Finally, SQZ poration cannot currently be applied to treat cell populations of distributed sizes. On the other hand, because the UHT mechanoporation device's capture wells can be tailored to fit any cell diameter, creating a device with undersized capture wells will allow for successful treatment of large and small cell diameters.

Building off of the established principle of SQZ poration, recent technologies have attempted to improve this system. Single point constriction (SPC) poration devices use a set of serial, short single-point constrictions in a flow-through microfluidic channel to allow for transient membrane poration.[82] Much like the original SQZ concept without an external electric field, delivery in SPC-based devices relies on passive diffusion of exogenous molecules in solution. The advantages of this system over SQZ are minimal backpressure during operation as well as comparable delivery efficiencies while significantly reducing the constriction length and increasing the number of dimensions over which the cell is deformed. This system maintains the versatility of small molecule delivery (siRNA, fluorescent molecules, etc.), however has shown little success in efficient delivery of large molecules. The delivery efficacy of 70 kDa dextran molecules for example is reported to be 60% at maximum.[82] As of now, the authors have admitted no success for plasmid delivery. Moreover, though high delivery efficiencies have been reported with this system (80-90% for small molecules), they have been achieved using 2-4 sequential constriction with small diameters, and large pressures. Such operational factors negatively impact the viability of the applied cell types, and foreshadow low efficiencies if attempts are made to introduce large molecules using this device.

Conversely, the UHT mechanoporation system exhibits high throughput operation, as well as the successful delivery of large plasmids (4kbp pmax eGFP) with minimal effect on cell viabilities (> 90%). As opposed to the necessity of high concentrations to achieve delivery of molecules using the SPC system (100 μg/mL) for modest efficiencies (60%),

we have demonstrated 90% transfection efficiencies of eGFP plasmid at a concentration of 20 μg/mL.

Acoustic shear poration (ASP) has used the limitations of SQZ poration as a basis of creating a novel poration system based on membrane shearing. ASP uses an array of acoustic horn structures for focused application of mechanical stimuli in conjunction with a piezoelectric transducer for acoustic wave generation.[83] This generates a pressure gradient for fluid/cell transport. As the cells flow through small outlets at the base of the horned structure array, the acoustic waves lead to cell shearing, leading to spontaneous membrane pore formation. An electric field is established within the collection cuvette, allowing for delivery of charged molecules into the cytoplasm. Though currently unconfirmed, ASP has the advantage of high throughput and scalability, much like the UHT mechanoporation device.[83] In addition, this system has the distinct advantage of being able to control the degree of poration applied to the cells (i.e. no effect, reversible/irreversible poration, lysis/death) by controlling the exposure time and shear rate (k). The ASP system also claims to address some of the clogging issues exhibited by SQZ.

Despite the effectiveness of this system, it exhibits several limitations that are not inherent to the UHT mechanoporation device. Similar to SQZ poration, this device requires the application of an electric field to transfect large molecules and shows non-competitive transfection efficiencies for Jurkat cells (35%) at higher concentrations (30 μg/mL).[83] As a review, the UHT mechanoporation device has demonstrated transfection efficiencies of greater than 90% for Jurkat cells using delivery concentrations of 20 μg/mL. In addition, while the mechanoporation chip is capable of transiently porating multiple cell types using

the same device, the ASP system is cell type limited. This means that a single device can only treat one cell type, and a new device must be fabricated to treat another cell model.

The inertial microfluidic cell hydroporator (iMCH) represents the simplest flow-based cell poration system that has been developed within the last year. This system allows for cellular delivery through 3 fundamental steps: (1) the cell/delivery molecule suspension is injected into a microfluidic glass channel, (2) cells are aligned to the middle of the channel through basic inertial forces, (3) cells collide sequentially with a sharp tip in the channel wall, leading to fluid shear induced membrane disruption and subsequent delivery of the exogenous molecule in suspension.[84] Like most flow-based devices, the iMCH system sports an ultrahigh throughput functionality (greater than 1e6 cells), though no cells counts were reported in this study. One of its greatest advantages is the insensitivity to cell size. As no true squeezing or passage through a sized entry point is necessary for this poration device, it can treat nearly all cell diameters. .[84] In addition, the authors assume consistent molecular delivery due to the uniform forces applied on every cell, attained from the serial poration scheme. The UHT mechanoporation device not only has all of the advantages demonstrated by the iMCH, but it is able to address several of the iMCH limitations.

Due to the large Reynolds numbers required for device operation, the delivery of large fluorescent molecules, such a 70kDa FITC yields only a 50% efficiency, and at the expense of high viabilities. In addition, this system demonstrates a minimal pmax GFP transfection efficiency (45-50%), far below the efficiencies generated by the UHT mechanoporation device. In addition, the UHT mechanoporation device may be superior

in poration functionality by reducing the flow rates (and associated forces) for poration by first bringing cells into close proximity to the solid penetrators.

6.3.4.2 Electroporation Competitive Landscape

Quite possibly the most competitive electroporation system currently established is the nanoelectroporation (NEP) platform. This system applies three sets of electric fields to capture cells onto an array of microchannels, transiently puncture the plasma membrane, and deliver an exogenous payload into the cell cytosol.[85] The NEP system shares many of the same advantages as the UHT mechanoporation device. Both systems manipulate suspended, clinically relevant cell types, exhibit single cell control, and high eGFP transfection with a relatively minimal loss in viability. However, the UHT mechanoporation system demonstrates higher efficiencies for GFP (90%) compared to NEP (75%), and superior cellular viabilities after transfection: 90% vs. 80%.[85] Most importantly, the NEP system has a significant limitation that the UHT mechanoporation device addresses: the need for an electric field as the driving factor for delivery. Due to this field requirement, the NEP platform relies on charge molecules for successful delivery. Since the UHT mechanoporation system uses diffusion gradients as the driving factor for delivery, it is not limited to only charged molecules.

Electric fields have also been applied as a method to create projectiles of delivery molecules that simultaneously porate and deliver into a target cell's cytosol. The electro hydrodynamic atomization (EHDA) method uses an electrically conductive fluid housed in a delivery capillary to generate an electrospray for cell permeabilization. The capillary

acts as the primary electrode, while the cell monolayer acts as the counter electrode. These electrodes are then connected to a high voltage source, which generates the electric field that drives the electrospray into the cell monolayer.[86] The EHDA has a simple and robust design, with an ease of manufacturability, all of which are advantages reflected by the UHT mechanoporation chip. In addition, both systems are not limited to charged molecules for delivery and have a certain degree of control over the quantity of payload delivered into each cell whether it is by the electrospray parameters or the concentration of delivery molecule in solution.

However, unlike the UHT mechanoporation system, EHDA can only treat non-trypsinized cell population in a monolayer. This leads to a limitation of the application of EHDA. Because EHDA is serial in its operation, it exhibits a low throughout (1 cell/spray). The transfection efficiencies reported via EHDA are also not competitive compared to the UHT mechanoporation device. EHDA demonstrates a minimal transfection efficiency for clinically relevant cells (60% for pmax GFP) with a minimal associated cell viability following poration and delivery (50%).[86] The UHT mechanoporation device is a high throughput system that can treat clinically relevant cell types on a massively parallelized scheme with > 90% transfection efficiencies and cell viabilities.

6.3.4.3 Sonoporation Competitive Landscape

Acoustic fields have long been utilized as a method for transient membrane poration for cell delivery, with the typical bulk ultrasound system acting as the standard.[37] However, recent research efforts have attempted to streamline the technology to allow for

precise transient membrane poration and delivery. Bubble microjet poration (BMP) is one such example of a technology that uses acoustic fields to precisely permeabilize a target cell's plasma membrane. This system individually immobilizes cells in conical trapping structures as a suspension of cells is flown across the device's functional surface. BMP then nucleates individual bubbles next to each trapped cell using an acoustic field. These bubbles then burst and the jetting phenomenon transiently porates the target cell's plasma membrane.[38] Delivery is achieved via passive diffusion of the exogenous molecule which is solubilized in the surrounding solution.

Though BMP has advantages characteristic of the UHT mechanoporation system: precision, diffusion driven delivery, and tunability of the membrane pore size (based on the distance of the bubble from the cell), it suffers from several disadvantages that reduce its impact as an effective means of achieving intracellular delivery. In its current iteration, BMP has a limitation in throughput: 65 treated cells assuming a 100% viability.[38] In addition, the researchers report no transfection of complex molecules. Conversely, as has been stated previously, the UHT mechanoporation device can treat up to 10k cells in its current iteration and has successfully transfected pmax GFP plasmids with high efficacy.

Microbubbles similar to those applied in BMP have also been used as a means of increasing the efficiency of standard bulk sonoporation. Crosslinked positive microbubbles (CPMBs) are produced by covalently crosslinking PEI_{1800} to BSA. The disulfide bonds within the BSA stabilize the formation of these microbubbles.[87] [Du. J, Colloids and Surfaces B] Through electrostatic interaction, the payload (DNA) is adsorbed onto the surface of the CPMBs. Rupture of the bubbles via sonication leads to simultaneous microjets and

introduction of DNA into the porated cell's cytoplasm. CPMB has the advantage of ease of manufacturability, demonstrates competitive transfection of DNA (using conjugated Cy3 markers as fluorescent confirmation) with an efficiency of 80%, as well as high throughput (as this is still a bulk sonoporation method).[87]

However, it's limited by the fact that it treats trypsinized cell populations, similar to EHDA. In addition, unlike the UHT mechanoporation system which precisely generates only a single pore per cell, the CPMB platform still relies on bulk sonoporation for membrane permeabilization. As such, it has no discrete control over how many transient pores are created per cell. Moreover, the extended sonoporation times necessary for successful DNA transfection impacts cellular viability (70%).[87] Finally, like most of the current cellular manipulation technologies in the competitive landscape, CPMB requires the use of a charged molecule for delivery (i.e. adsorption onto the CPMB surface). These limitations hinder CPMB from becoming a competitive technology against the high throughput and high efficiency operation of the UHT mechanoporation system.

6.3.4.4 Conclusions on the Competitive Landscape

From the comparisons conducted against a representative range of competitive technologies focused on transient cell membrane permeabilization, we can conclude that the current iteration of the UHT mechanoporation device demonstrates a higher potential to meet the needs of CAR T-cell manufacturing. Not only does the UHT mechanoporation system exhibit efficiencies that surpass many of the efficiencies reported by competing techniques (i.e. NEP, SQZ, BMP), it also addresses several of the limitations inherent in

said techniques. These include the need for external fields to drive large molecule delivery, sacrifices in cell viability for high transfection efficiencies of large molecules, and low throughput. As a result, the UHT mechanoporation device, with its advantages of scalability, precision, and ability to effectively treat suspended cell types along with its superiority in operation over the competitive landscape represents a concept that will address the current limitations of gold standard genetic modification techniques for CAR T-cell production.

7. CONCLUSIONS AND FUTURE DIRECTIONS

Conclusions

7.1. Summary of Current State of the UHT Mechanoporation Device

T-cell immunotherapies hold the promise of being one of the first true cures for cancer, addressing many of the critical limitations inherent to current gold standard treatments. However, like most therapies, it comes with certain drawbacks. Viral transduction is primarily limited in scalability and cost, and it is here that non-biological methods of cell delivery may pose a solution.

In summary, physical poration methods such as squeeze cell poration, or microinjection provide a safer and more precise means of cellular manipulation compared to other competing non-biological technologies. However, due to the difficulty of cell targeting and precise poration, few mechanoporation technologies exist that can manipulate cells at an appreciable rate. By exploiting silicon microfabrication, we have developed a scalable and potentially cost effective mechanoporation device that can be tailored to any cell type via small variations in the capture well geometry. Moreover, due to the inherent parallelized design and fabrication methodology of our device we can further scale the number of capture wells beyond the current 10K value if necessary. The unique design of our UHT mechanoporation device allows for simultaneous capture and puncture via aspiration flow in each capture well. As such, the central parameters that were necessary to optimize for device operation were the capture and immobilization/puncture flow rates.

Successful flow rate optimization, in combination with other improvements in peripheral parameters (i.e. initial reservoir volume, cell type, fixture set, etc.) has led to

cell capture efficiencies of 70%, and subsequent delivery efficiencies of > 90% for propidium iodide and transfection efficiencies of > 90% for eGFP plasmid in our most recent studies (chapter 6). The lower delivery yields of 40% from the PI delivery experiments serve to indicate areas where the UHT mechanoporation device still requires development. However, the > 90% delivery yields seen from the eGFP transfection studies highlight the capabilities of Jurkat cells to recover during the 12-hour incubation period. Overall, our efforts demonstrate the high impact of our UHT mechanoporation chip in relation to efficient cell manipulation, and towards making physical manipulation a competitive technology in cellular therapeutics.

7.2. Recommendations for Future Studies

The optimization studies covered throughout this dissertation were a means to illustrate the feasibility of an ultrahigh throughput device capable of cellular manipulation. However, in order to truly be a competitive therapeutic system, this device would require the addition of new functionalities, namely that of active injection. The mechanoporation concept represented an interim device to allow us to optimize nearly every functional aspect of a similar cell poration device capable of actively introducing exogenous payloads into cell's cytoplasm or nucleus, as illustrated in figure 7.1. But, this system comes with the added complexity of micromachining an entirely independent fluidic circuitry on the backside of the chip for capture/poration and injection. In addition, we will be required to not only fabricate refined penetrators, but also deep etch a central lumen for injection functionality into each microneedle. With the addition of these hollow penetrators, our

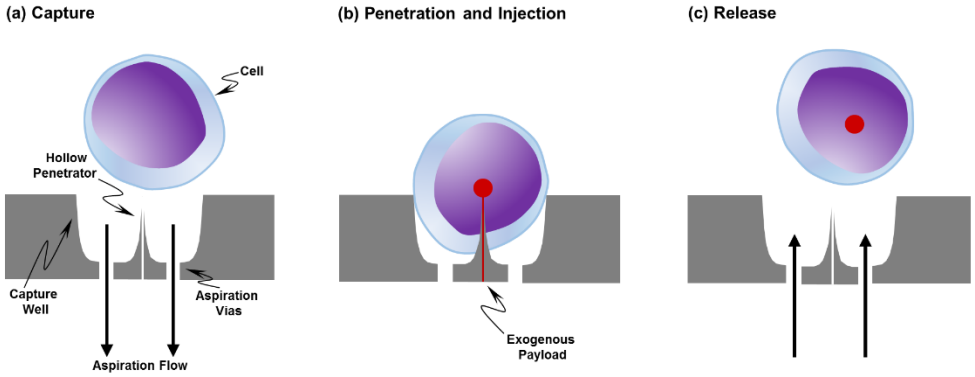

Figure 7.1. Microinjection device operation concept (illustrated for a single capture site within a larger array). Each capture site consists of a hemispherical capture well with a centrally-located hollow penetrator and a multiplicity of aspiration vias situated at the bottom of the well. Microinjection is achieved through: a) Use of negative flow through the aspiration vias to draw the cell into the capture well; b) Poration of the plasma membrane by the penetrator upon cell capture; and injection of the exogenous payload via the integrated fluidic circuitry within the penetrator's lumen c) Reversal of aspiration flow to release the cell.

UHT mechanoporation system will be able to introduce specific volumes of delivery material into each punctured cell.

In the short term, we can further improve peripheral parameters of the current UHT mechanoporation device to increase efficiency. The low degree of cell recovery following our immobilization/puncture step can be addressed via several avenues. One of these avenues is improving the isotropic aspiration via etch responsible for simultaneous realization of the capture well geometry and solid central penetrator geometry. Due to transport limitations during this step, as covered in chapter 3, the profile of the capture well follows a clover-leaf phenotype. By altering this etch step from a single step to several shorter etch steps we will achieve a truer to form profile of the capture wells. Since we hypothesize that the sharp edges inherent to the current clover-leaf capture sites wedge cells during device testing, this change in the fabrication process will theoretically improve the number of recovered cells.

A different solution would be to apply surface passivation to reduce the "biofouling" of un-released cells in our current device iteration.[88,89] This passivation will reduce the adherent properties of the UHT device chip thereby potentially increasing the release efficiency. In this strategy, we may need to re-optimize the capture parameters due to the altered properties of the device array surface.

A secondary limitation to be addressed in both the current mechanoporation device as well as the active injection system is that of transient increases in pressure across the device array during successive capture well occupation. Cell that are introduced later in the capture cycle experience higher pressures compared to cells captured from earlier "pulses".

This is explained by conservation of mass. As the number of open vias begin to reduce, the relative flow at the device array begins to increase, thereby causing a pressure spike. Such an effect is undesirable because it can be detrimental effect on the delicate viability of our treated cells. Not only will late stage cells begin to impact open capture wells at significantly higher velocities, but early stage captured cells will begin to experience increasing pressures and potentially be sheared through the device itself. To alleviate this uneven pressure distribution, we can look to PID-control systems as a possible solution.

Systems that have closed loop feedback control have already been demonstrated to work efficiently in automated micro-drop production using flow focusing.[90] By tracking the initial diameters of the micro-droplets formed, the closed loop PI system modulates the flow rates of both the dispersed and continuous phase liquids in the microchannel to reach the desired micro-droplet size. Such research sets a precedent for the application of PID control to UHT mechanoporation device operation. Moreover, because flow through our system can be assumed to be laminar, viscous, and incompressible, we can fine tune and predict the correct circuit geometry by analogizing fluid flow through the chip and tubing as electrical circuitry.[91] By actively modulating the flow rate across the surface of the device, all cells, regardless of when they are introduced to the device will experience a consistent pressure. As a result, this system will aid in increasing the efficiency of the UHT mechanoporation chip.

BIBLIOGRAPHY

1. The WHO. Cancer, *Media Center*, 2018, 1-7.

2. NIH. National Cancer Institute, *What is Cancer,* 2015.

3. R. D. Wood, M. Mitchell, J. Sgouros and T. Lindahl, *Science*, 2001, **291**, 1284-1289.

4. R. L. Siegel, K. D. Miller and A. Jemal, *CA Cancer J Clin*, 2018, **68**(1), 7-30.

5. A. Modi, A. Grasso and A. Simmons, 1998.

6. L. B.Bailey and I. Jesse F. Gregory, *Journal of Nutrition*, 1999, **129**, 779-782.

7. L. Brannon-Peppas and J. O. Blanchette, *Advanced Drug Delivery Reviews*, 2012, **64**, 206-212.

8. R. J. Chari, *Accounts of Chemical Research*, 2008, **41**(1), 98-107.

9. C. Sawyers, *Nature*, 2004, **432**(294-297).

10. M. Kalos and C. H. June, *Immunity*, 2013, **39**(1), 49-60.

11. N. P. Restifo, M. E. Dudley and S. A. Rosenberg, *Nat Rev Immunol*, 2012, **12**(4), 269-281.

12. J. Deguine, B. Breart, F. Lemaitre, J. P. Di Santo and P. Bousso, *Immunity*, 2010, **33**(4), 632-644.

13. J. N. Kochenderfer, W. H. Wilson, J. E. Janik, M. E. Dudley, M. Stetler-Stevenson, S. A. Feldman, I. Maric, M. Raffeld, D. A. Nathan, B. J. Lanier, R. A. Morgan and S. A. Rosenberg, *Blood*, 2010, **116**(20), 4099-4102.

14. R. J. Brentjens, I. Riviere, J. H. Park, M. L. Davila, X. Wang, J. Stefanski, C. Taylor, R. Yeh, S. Bartido, O. Borquez-Ojeda, M. Olszewska, Y. Bernal, H. Pegram, M. Przybylowski, D. Hollyman, Y. Usachenko, D. Pirraglia, J. Hosey, E. Santos, E. Halton, P. Maslak, D. Scheinberg, J. Jurcic, M. Heaney, G. Heller, M. Frattini and M. Sadelain, *Blood*, 2011, **118**(18), 4817-4828.

15. S. A. Rosenberg, J. C. Yang, R. M. Sherry, U. S. Kammula, M. S. Hughes, G. Q. Phan, D. E. Citrin, N. P. Restifo, P. F. Robbins, J. R. Wunderlich, K. E. Morton, C. M. Laurencot, S. M. Steinberg, D. E. White and M. E. Dudley, *Clin Cancer Res*, 2011, **17**(13), 4550-4557.

16. D. L. Porter, M.D., B. L. Levine, Ph.D., M. Kalos, Ph.D., A. Bragg, M.D. and C. H. June, M.D., *The New England Journal of Medicine*, 2011, **365**, 725-733.

17. P. F. Robbins, R. A. Morgan, S. A. Feldman, J. C. Yang, R. M. Sherry, M. E. Dudley, J. R. Wunderlich, A. V. Nahvi, L. J. Helman, C. L. Mackall, U. S. Kammula, M. S. Hughes, N. P. Restifo, M. Raffeld, C. C. Lee, C. L. Levy, Y. F. Li, M. El-Gamil, S. L. Schwarz, C. Laurencot and S. A. Rosenberg, *J Clin Oncol*, 2011, **29**(7), 917-924.

18. J. N. Kochenderfer, M. E. Dudley, S. A. Feldman, W. H. Wilson, D. E. Spaner, I. Maric, M. Stetler-Stevenson, G. Q. Phan, M. S. Hughes, J. C. Yang, U. S. Kammula, L. Devillier, R. Carpenter, D. A. Nathan, R. A. Morgan, C. Laurencot and S. A. Rosenberg, *Blood*, 2011, **119**(12), 2709-2720.

19. M. Ahmadzadeh, L. A. Johnson, B. Heemskerk, J. R. Wunderlich, M. E. Dudley, D. E. White and S. A. Rosenberg, *Blood*, 2009, **114**(8), 1537-1544.

20. L. Baitsch, P. Baumgaertner, E. Devevre, S. K. Raghav, A. Legat, L. Barba, S. Wieckowski, H. Bouzourene, B. Deplancke, P. Romero, N. Rufer and D. E. Speiser, *J Clin Invest*, 2011, **121**(6), 2350-2360.

21. M. A. Cheever, P. D. Greenberg and A. Fefer, *The Journal of Immunology*, 1980, **125**(2), 711-714.

22. C. Wrzesinski, C. M. Paulos, L. Gattinoni, D. C. Palmer, A. Kaiser, Z. Yu, S. A. Rosenberg and N. P. Restifo, *J Clin Invest*, 2007, **117**(2), 492-501.

23. D. I. Gabrilovich, S. Ostrand-Rosenberg and V. Bronte, *Nat Rev Immunol*, 2012, **12**(4), 253-268.

24. R. Offringa, *Curr Opin Immunol*, 2009, **21**(2), 190-199.

25. G. M. Bendle, J. B. Haanen and T. N. Schumacher, *Curr Opin Immunol*, 2009, **21**(2), 209-214.

26. W. Qasim and A. J. Thrasher, *Br J Haematol*, 2014, **166**(6), 818-829.

27. M. V. Maus, S. A. Grupp, D. L. Porter and C. H. June, *Blood*, 2014, **123**(17), 2625-2635.

28. H. Singh, H. Huls, P. Kebriaei and L. J. Cooper, *Immunol Rev*, 2014, **257**(1), 181-190.

29. A. C. Field, C. Vink, R. Gabriel, R. Al-Subki, M. Schmidt, N. Goulden, H. Stauss, A. Thrasher, E. Morris and W. Qasim, *PLoS One*, 2013, **8**(6), e68201.

30. X. Wang and I. Riviere, *Cancer Gene Ther*, 2015, **22**(2), 85-94.

31. C. Humphries, *Nature*, 2013, **304**, S13-S15.

32. J. M. Meacham, K. Durvasula, F. L. Degertekin and A. G. Fedorov, *J Lab Autom*, 2014, **19**(1), 1-18.

33. M. Khine, C. Ionescu-Zanetti, A. Blatz, L. P. Wang and L. P. Lee, *Lab Chip*, 2007, **7**(4), 457-462.

34. J. K. Valley, S. Neale, H. Y. Hsu, A. T. Ohta, A. Jamshidi and M. C. Wu, *Lab Chip*, 2009, **9**(12), 1714-1720.

35. W. Longsine-Parker, H. Wang, C. Koo, J. Kim, B. Kim, A. Jayaraman and A. Han, *Lab Chip*, 2013, **13**(11), 2144-2152.

36. Y. Xu, S. Su, C. Zhou, Y. Lu and W. Xing, *Bioelectrochemistry*, 2015, **102**, 35-41.

37. M. Afadzi, S. P. Strand, E. A. Nilssen, S. E. Masoy, T. F. Johansen, R. Hansen, B. A. Angelsen and L. D. C. de, *IEEE Trans Ultrason Ferroelectr Freq Control*, 2013, **60**(1), 21-33.

38. Z. G. Li, A. Q. Liu, E. Klaseboer, J. B. Zhang and C. D. Ohl, *Lab Chip*, 2013, **13**(6), 1144-1150.

39. Q. Fan, W. Hu and A. T. Ohta, *Lab Chip*, 2015, **15**(2), 581-588.

40. Y. C. Wu, T. H. Wu, D. L. Clemens, B. Y. Lee, X. Wen, M. A. Horwitz, M. A. Teitell and P. Y. Chiou, *Nat Methods*, 2015, **12**(5), 439-444.

41. Y. Zhang and L. C. Yu, *Curr Opin Biotechnol*, 2008, **19**(5), 506-510.

42. Y. Zhang and L. C. Yu, *Bioessays*, 2008, **30**(6), 606-610.

43. A. K. Shalek, J. T. Robinson, E. S. Karp, J. S. Lee, D. R. Ahn, M. H. Yoon, A. Sutton, M. Jorgolli, R. S. Gertner, T. S. Gujral, G. MacBeath, E. G. Yang and H. Park, *Proc Natl Acad Sci U S A*, 2010, **107**(5), 1870-1875.

44. A. Sharei, J. Zoldan, A. Adamo, W. S. Sim, N. Cho, E. Jackson, S. Mao, S. Schneider, M. J. Han, A. Lytton-Jean, P. A. Basto, S. Jhunjhunwala, J. Lee, D. A.

Heller, J. W. Kang, G. C. Hartoularos, K. Kim, D. G. Anderson, R. Langer and K. F. Jensen, *PNAS*, 2012, **110**(6), 2082-2087.

45. A. Sharei, R. Trifonova, S. Jhunjhunwala, G. C. Hartoularos, A. T. Eyerman, A. Lytton-Jean, M. Angin, S. Sharma, R. Poceviciute, S. Mao, M. Heimann, S. Liu, T. Talkar, O. F. Khan, M. Addo, U. H. von Andrian, D. G. Anderson, R. Langer, J. Lieberman and K. F. Jensen, *PLoS One*, 2015, **10**(4), e0118803.

46. M. P. Stewart, A. Sharei, X. Ding, G. Sahay, R. Langer and K. F. Jensen, *Nature*, 2016, **538**(7624), 183-192.

47. F. Liu, D. Wu, X. Wu and K. Chen, *Soft Matter*, 2015, **11**(7), 1434-1442.

48. K. J. Cha, T. Kim, S. J. Park and D. S. Kim, *Journal of Micromechanics and Microengineering*, 2014, **24**(11), 115015.

49. E. Cornell, W. W. Fisher, R. Nordmeyer, D. Yegian, M. Dong, M. D. Biggin, S. E. Celniker and J. Jin, *Rev Sci Instrum*, 2008, **79**(1), 013705.

50. D. V. Nicolau, S. Sakai, J. Enderlein, S. Youoku, Y. Suto, R. C. Leif, D. L. Farkas, M. Ando, A. Ito and R. Raghavachari, 2005, **5699**, 59.

51. W. Wang, X. Liu, D. Gelinas, B. Ciruna and Y. Sun, *PLoS One*, 2007, **2**(9), e862.

52. S. Zappe, M. Fish, M. P. Scott and O. Solgaard, *Lab Chip*, 2006, **6**(8), 1012-1019.

53. X. J. Zhang, S. Zappe, R. W. Bernstein, O. Sahin, C. C. Chen, M. Fish, M. P. Scott and O. Solgaard, *Sensors and Actuators A: Physical*, 2004, **114**(2-3), 197-203.

54. S. Park, Y. S. Kim, W. B. Kim and S. Jon, *Nano Lett*, 2009, **9**(4), 1325-1329.

55. M. Nagai, K. Oohara, K. Kato, T. Kawashima and T. Shibata, *Biomed Microdevices*, 2015, **17**(2), 41.

56. H. Shafiee, J. L. Caldwell, M. B. Sano and R. V. Davalos, *Biomed Microdevices*, 2009, **11**(5), 997-1006.

57. A. Adamo and K. F. Jensen, *Lab Chip*, 2008, **8**(8), 1258-1261.

58. A. Noori, P. R. Selvaganapathy and J. Wilson, *Lab Chip*, 2009, **9**(22), 3202-3211.

59. W. Tonomura, T. Yamamoto, T. K. Saito and S. Konishi, *Sensors and Actuators B: Chemical*, 2010, **148**(1), 29-33.

60. D. Delubac, C. B. Highley, M. Witzberger-Krajcovic, J. C. Ayoob, E. C. Furbee, J. S. Minden and S. Zappe, *Lab Chip*, 2012, **12**(22), 4911-4919.

61. Y. Zhang, C. B. Ballas and M. P. Rao, *IEEE*, 2012.

62. S. S. Saliterman, *Fundamentals of Biomems and Medical Microdevices,* 2006, **First Edition**(SPIE — The International Society for Optical Engineering).

63. M. J. Madou, *Fundamentals of Microfabrication: The Science of Miniaturization,* 2002, **Second Edition**(CRC Press LLC).

64. S. C. Gott, *Titanium Vascular Stents with Rationally-Designed Sub-Micrometer Scale Surface Patterning,* 2014*,* **Doctoral Dissertation**(Mechanical Engineering), University of California, Riverside.

65. S. Park, S. O. Choi, S. J. Paik, S. Choi, M. Allen and M. Prausnitz, *Biomed Microdevices*, 2016, **18**(1), 10.

66. R. Zaouk, B. Y. Park and M. J. Madou, *Introduction to Microfabrication Techniques,* 2006, Humana Press Inc.).

67. D. L. M. C. Facility, *Introduction to Microscopy,* 2018, Light Microscopy Core Facility, https://microscopy.duke.edu/introduction-microscopy.

68. C. P. Fitch, *JAMA*, 1915, **64**(11), 893-896.

69. vlab.amrita.edu, *Hemocytometer (Counting of Cells),* 2011, http://vlab.amrita.edu/?sub=3&brch=188&sim=336&cnt=2

70. N. S. Prathalingam, W. W. Holt, S. G. Revell, S. Jones and P. F. Watson, *J Androl*, 2006, **27**(2), 257-262.

71. D. Cadena-Herrera, J. E. Esparza-De Lara, N. D. Ramirez-Ibanez, C. A. Lopez-Morales, N. O. Perez, L. F. Flores-Ortiz and E. Medina-Rivero, *Biotechnol Rep (Amst)*, 2015, **7**(9-16.

72. A. L. Givan, *Flow Cytmetry: First Principles,* 2001, **Second**(Wiley Liss).

73. P. O. Krutzik and G. P. Nolan, *Cytometry A*, 2003, **55**(2), 61-70.

74. I. Vermes, C. Haanen and C. Reutelingsperger, *Journal of Immunological Methods*, 2000, **243**(2000), 167-190.

75. C. Nakamura, H. Kamiishi, N. Nakamura and J. Miyake, Electrochemistry, 2008, **76**(8), 586-589.

76. I. Obataya, C. Nakamura, S. Han, N. Nakamura and J. Miyake, Nano Lett, 2005, **5**(1), 27-30.

77. Y. Zhang, Mems-Based Massively-Parallelized Mechanoporation Instrumentation for Ultrahigh Throughput Cellular Manipulation, 2012, Doctoral Dissertation(Mechanical Engineering), University of California, Riverside.

78. H. A. Rendall, R. F. Marchington, B. B. Praveen, G. Bergmann, Y. Arita, A. Heisterkamp, F. J. Gunn-Moore and K. Dholakia, Lab Chip, 2012, **12**(22), 4816-4820.

79. C. Bouzigues, M. Morel, A. Triller and M. Dahan, Proc Natl Acad Sci U S A, 2007, **104**(27), 11251-11256.

80. L. Chang, P. Bertani, D. Gallego-Perez, Z. Yang, F. Chen, C. Chiang, V. Malkoc, T. Kuang, K. Gao, L. J. Lee and W. Lu, Nanoscale, 2016, **8**(1), 243-252.

81. X. Ding, M. Stewart, A. Sharei, J. C. Weaver, R. S. Langer and K. F. Jensen, *Nat Biomed Eng*, 2017, **1**.

82. X. Xing, Y. Pan and L. Yobas, *Anal Chem*, 2018, **90**(3), 1836-1844.

83. J. M. Meacham, K. Durvasula, F. L. Degertekin and A. G. Fedorov, *Sci Rep*, 2018, **8**(1), 3727.

84. Y. Deng, M. Kizer, M. Rada, J. Sage, X. Wang, D. J. Cheon and A. J. Chung, *Nano Lett*, 2018, **18**(4), 2705-2710.

85. L. Chang, D. Gallego-Perez, X. Zhao, P. Bertani, Z. Yang, C. L. Chiang, V. Malkoc, J. Shi, C. K. Sen, L. Odonnell, J. Yu, W. Lu and L. J. Lee, *Lab Chip*, 2015, **15**(15), 3147-3153.

86. S. Boehringer, P. Ruzgys, L. Tamo, S. Satkauskas, T. Geiser, A. Gazdhar and D. Hradetzky, *Sci Rep*, 2018, **8**(1), 4031.

87. J. Du, X. Zhao, B. Li, Y. Mou and Y. Wang, *Colloids Surf B Biointerfaces*, 2018, **161**(279-287).

88. J. D. Cox, M. S. Curry, S. K. Skirboll, P. L. Gourley and D. Y. Sasaki, Biomaterials, 2002, **23**(929-935).

89. S. L. Peterson, A. McDonald, P. L. Gourley and D. Y. Sasaki, J Biomed Mater Res A, 2005, **72**(1), 10-18.

90. E. Miller, M. Rotea and J. P. Rothstein, Lab Chip, 2010, **10**(10), 1293-1301.

91. K. W. Oh, K. Lee, B. Ahn and E. P. Furlani, Lab Chip, 2012, **12**(3), 515-545.

92. E. R. Parker, M. P. Rao, K. L. Turner, C. D. Meinhart and N. C. MacDonald, Journal of Microelectromechanical Systems, 2007, **16**(2), 289-295.

9. APPENDICES

Appendix A

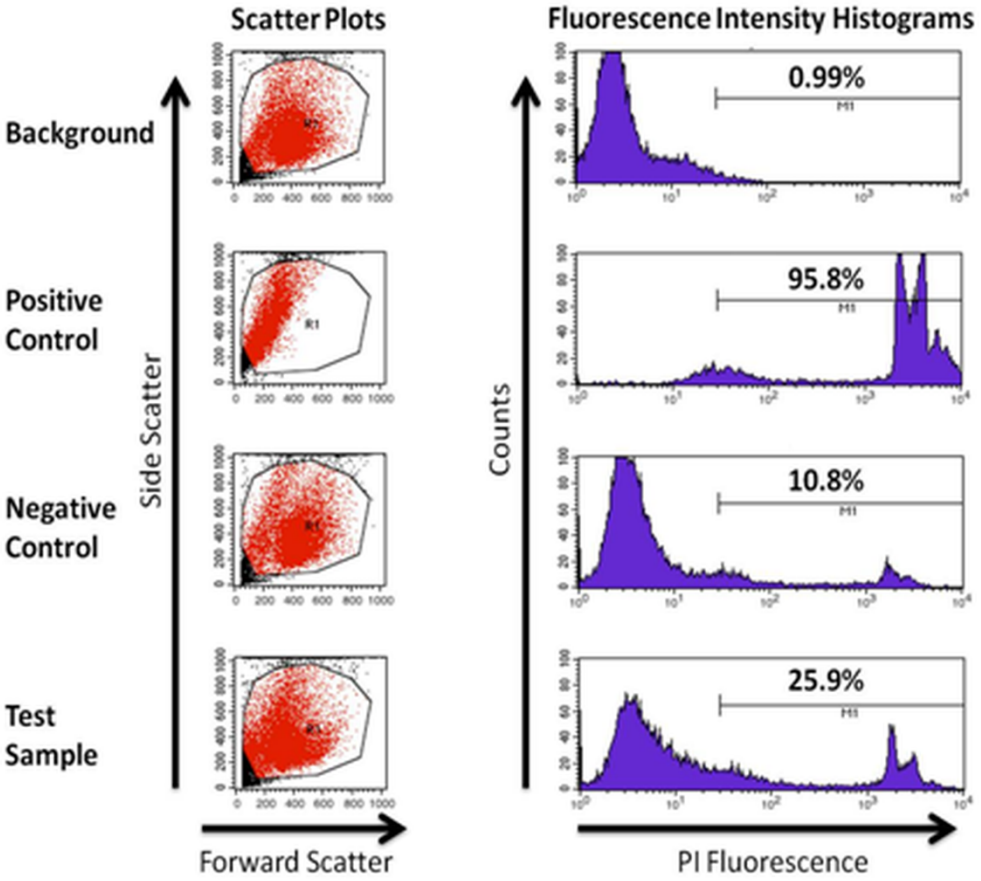

Figure A.1. Flow cytometry 2-D scatter plots for preliminary UHT mechanoporation device testing. (a) Background/autofluorescence control of K562 cells in culture with no exposure to PI. (b) Permeabilized cells incubated with propidium iodide. (c) K562 cells exposed to PI with no form of membrane permeabilization to account for passive diffusion of PI. (d) Mechanoporation sample. Cells were exposed to the capture wells and solid central penetrators repeatedly and incubated with PI. Delivery efficiency was calculated to be 14.1% via the subtraction of the percentage of PI positive events within the negative and background control from that of the mechanoporation sample.

Appendix B

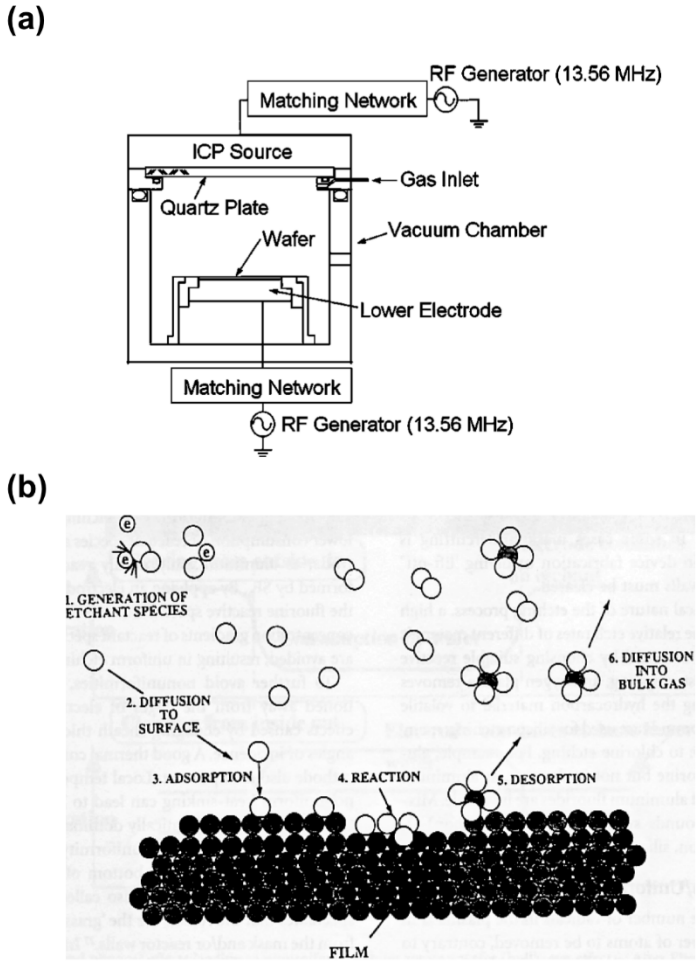

Figure B.1. (a) Schematic of a typical reactive ion etching (RIE setup).[92] (b) RIE uses ionized gas, or plasma, to bombard and react with the substrate of choice. The charge imbalance between the cathode and anode, generated by the RF source, causes ionized particles to move towards the anode, on which the wafer sits. When this occurs, the ionized particles bombard/chemically react with the surface, leading to etching of the substrate.[62]

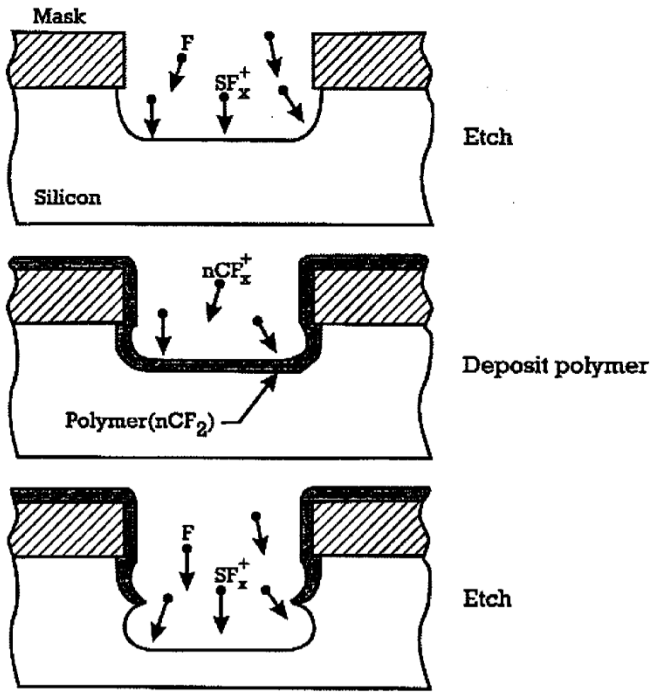

Figure B.2. Illustration of the fundamental steps involved in Bosch deep reactive ion etching (DRIE), which is used for realization of several of the high aspect ratio features in the UHT mechanoporation device.[62] This method applies cycles of SF_6 gas etching along with passivation formation using C_4F_8 ions to allow for generation of high aspect ratio features. Polymeric, passivation species formed from chemical cross-linking of C_4F_8 ions during plasma creation deposit on exposed areas of the substrate and protect against lateral etching (i.e. side wall etching). The passivation is removed from the floor of the substrate and is followed by etching. Slight undercutting during the etching process leads to scalloped features.

Appendix C

C.1. Processing Parameters for UHT Mechanoporation Device Fabrication

C.1.2. Wafer Cleaning and Deposition of SiO_2 on Device and Handle Layers (Ref. 3.2.1)

1. **Piranha:** 1:1 H_2SO_4 (96% concentration) and H_2O_2 (30% concentration), 80˚C, 30 minutes
2. **Di Water Rinse:** 1 minute
3. **Oxide Strip:** HF (120 mL, 49% concentration) and DI water (6000 mL), 1 minute
4. **RCA 2 Clean:** HCl (1000 mL, 37% concentration) and H_2O_2 (1000 mL, 30% concentration) and DI water (5000 mL), 10 minutes
5. **Di Water Rinse:** 5 minutes
6. **N_2 Wafer Dry**
7. **Wet Oxidation for 1 µm SiO_2 deposition on device and handle layers:**
    - Furnace temperature ramp to 500˚C
    - N_2 stabilization: 5 sccm at 500˚C, 5 minutes
    - Wet growth process conditions: 7 sccm H_2, 4 sccm O_2, 1100˚C, 2 hours
        - *CVD Equipment Corporation*
8. **Characterization of Film Thickness via Ellipsometry:**
        - *UVISEL Spectroscopic Phase Modulated Ellipsometer*
9. **PECVD 2 µm SiO_2 Deposition on Handle Layer (2 cycles):**
    - Initial heat exchange temperature: 60
    - Cathode heat temperature: 300
    - Oxide N_2 prepurge: 2 min, 900 mTorr, N_2 500 sccm, Power 0 W

- Oxide stab: 2 min, 900 mTorr, 2% SiH_4 400 sccm, N_2O 900 sccm, Power 0 W
- Oxide dep: 25 min, 900 mTorr, 2% SiH_4 400 sccm, N_2O 900 sccm, Power 25 W
- Nitrogen purge: 10 min, 900 mTorr, N_2 500 sccm, Power 0 W
- 50-minute process time
    - *Plasmatherm 790/Unaxis*

C.1.3. Substrate Patterning and Lithography of Device Layer, and Mask Pattern Transfer (Ref. 3.2.2)

1. **Lithography:**
    - HDMS and SPR 955 CM-0.9 positive photoresist (1 μm film thickness)
    - 3000 rpm, 30 seconds
    - 60 second pre-exposure bake 95˚C
2. **Exposure:**
    - Step size: X = 16, Y = 16
    - Row: 5 (dyes)
    - Column: 5 (dyes)
    - Exposure: 1.6 seconds
    - 60 second post-exposure bake at 110˚C
        - *GCA 6300 i-line system*

3. **Develop:**
    - AZ300MIF, 70 seconds
4. **Verification:**
    - *Optical microscope*
5. **Reactive Ion Etching (RIE) of Device Layer:**
    - 300 W Power (Tolerance: 5%), 100 mTorr pressure (Tolerance: 33%), 30 sccm CHF3 (Tolerance: 20%), and 20 sccm CF4 (Tolerance: 20%)
    - He leak-up test: 1 min; Max leak rate: 15 mT/min
        - *STS Multiplex RIE System; Surface Technology Systems*
6. **Photoresist Strip and Characterization:**
    - Acetone, IPA, DI water rinse
    - N_2 Dry
    - Characterize via dektak
        - *Veeco Systems Dektak 8*

C.1.4. Substrate Patterning and Lithography of Handle Layer, and Mask Pattern Transfer (Ref. 3.2.3)

1. **Lithography:**
    - HDMS and SPR220-3.0 Positive Photoresist (3.0 μm film thickness)
    - 2000 rpm, 40 seconds
    - 90 second pre-exposure bake at 115˚C
    - Hard contact, 350 W, 20 second exposure

- *Suss Micro Tec MA6 Contact Aligner System*

- 90 second post-exposure bake at 115˚C

2. **Develop:**
   - AZ300MIF, 60 seconds
   - Optical microscopy verification
3. **Reactive Ion Etching (RIE) of Handle Layer:**
   - 300 W Power (Tolerance: 5%), 100 mTorr pressure (Tolerance: 33%), 30 sccm CHF3 (Tolerance: 20%) and 20 sccm CF4 (Tolerance: 20%)
     - *STS RIE Multiplex System*
   - He leak-up test: 1 min; Max leak rate: 15 mT/min
   - 15 minute etch
4. **Photoresist Strip and Characterization:**
   - Acetone, IPA, DI water rinse
   - N_2 Dry
   - Characterize via dektak
     - *Veeco Systems Dektak 8*
   - Dice wafer into 21 dyes using diamond scribe

C.1.5. Realization of Device and Handle Layer Features in the Si Substrate (Ref. 3.2.4)

1. **Silicon Deep Reactive Ion Etching of Handle Layer:**
   - Standard O_2 clean

- Etching step: 700 W ICP source power, 20 W sample RF power, 36 mT pressure, 130 sccm SF_6, 13 sccm O_2, 14 seconds
- Passivation step: 600 W ICP source power, 0 W sample RF power, 24 mT pressure, 85 sccm C_4F_8, 7 seconds
- ~ 2 hour 20 min etch for single device chip
    - *STS MESC ICP Etcher System*
- Remove device chip from carrier wafer using Acetone/IPA/DI Water

2. **Piranha:**
    - 1:1 H_2SO_4 (96% concentration) and H_2O_2 (30% concentration), 80˚C, 30 minutes
    - DI water rinse
    - N_2 dry
3. **Characterization:**
    - Scanning electron microscope (SEM)
        - Leo Supra 55
4. **Silicon Isotropic Etching on Device Layer:**
    - Standard O_2 Clean
    - 500 W ICP source power, 20 W sample RF power, 12 mT pressure, 95 sccm SF_6, 13 sccm O_2
    - 4 minute 10 second etch
        - STS MESC ICP Etcher System
5. **Verification:**
        - *Optical microscope*
6. **Silicon Deep Reaction Ion Etching on Device Layer:**

- Etching step: 600 W ICP source power, 17 W sample RF power, 24 mT pressure, 130 sccm SF_6, 13 sccm O_2, 7 sec
- Passivation step: 600 W ICP source power, 0 W sample RF power, 14 mT Pa pressure, 85 sccm C_4F_8, 5 sec
- 11 minute etch
    - STS MESC ICP Etcher System

7. **Verification:**
    - *Optical microscope*

C.1.6. Removal of SiO_2 Shadow Mask Layer, Penetrator Refinement, and Final Device Cleaning (Ref. 3.2.5)

1. **Reactive Ion Etching of SiO_2 Mask Layer:**
    - 300 W Power (Tolerance: 5%), 100 mTorr pressure (Tolerance: 33%), 30 sccm CHF3 (Tolerance: 20%) and 20 sccm CF4 (Tolerance: 20%)
    - 3 minute 40 second etch
        - STS Multiplex RIE System
2. **Characterization:**
    - Scanning electron microscope (SEM)
    - Leo Supra 55
3. **Cl_2 Anisotropic Etching for Penetrator Refinement:**
    - Step 1: Cl_2 10 sccm, Pressure 1.7 Pa, Step time 5 s, ICP source power 400 W, Sample RF power 0 W
    - Step 2: Cl_2 10 sccm, Pressure 1.2 Pa, Step time 5 s, ICP source power 400 W, Sample RF power 0 W

- Step 3: Cl_2 10 sccm, Pressure 1.2 Pa, Step time 5 min, ICP source power 400 W, Sample RF power 12 W
- Step 4: N_2 100 sccm, Pressure 2.5 Pa, Step time 10 s, ICP source power 100 W, Sample RF power 0 W
- Step 5: N_2 100 sccm, Pressure 2.5 Pa, Step time 5 s, ICP source power 50 W, Sample RF power 0 W
    - Panasonic ICP Etcher E 620-R&D System

4. **Characterization:**
    - Scanning electron microscope (SEM)
    - Leo Supra 55
5. **Reactive Ion Etching for Chlorine Passivation Removal:**
    - 300 W Power (Tolerance 10%), 100 mTorr pressure (Tolerance 33%), 50 sccm CF4 (Tolerance 20%) and 40 sccm O2 (Tolerance 10%)
        - STS Multiplex RIE System
6. **Characterization:**
    - Scanning electron microscope (SEM)
    - Leo Supra 55
7. **Reactive Ion Etching to Remove SiO_2 on Handle Layer and BOX Layer:**
    - 300 W Power (Tolerance: 5%), 100 mTorr pressure (Tolerance: 33%), 30 sccm CHF3 (Tolerance: 20%) and 20 sccm CF4 (Tolerance: 20%)
    - 14 minute etch
        - STS Multiplex RIE System

8. **Characterization:**
    - Scanning electron microscope (SEM)
    - Leo Supra 55
9. **Piranha (Sample Cleaning for Device Testing):**
    - 1:1 H_2SO_4 (96% concentration) and H_2O_2 (30% concentration), 80˚C, 30 minutes
    - DI water rinse
    - N_2 dry
10. **O_2 Ashing (Sample Cleaning for Device Testing):**
    - 0.6 mbar, 100 W, 2 mins
11. **Characterization**
    - Confirm chip cleanliness via optical microscope and SEM

C.2. Engineering Drawings of the Fixture Set for UHT Mechanoporation Device Testing

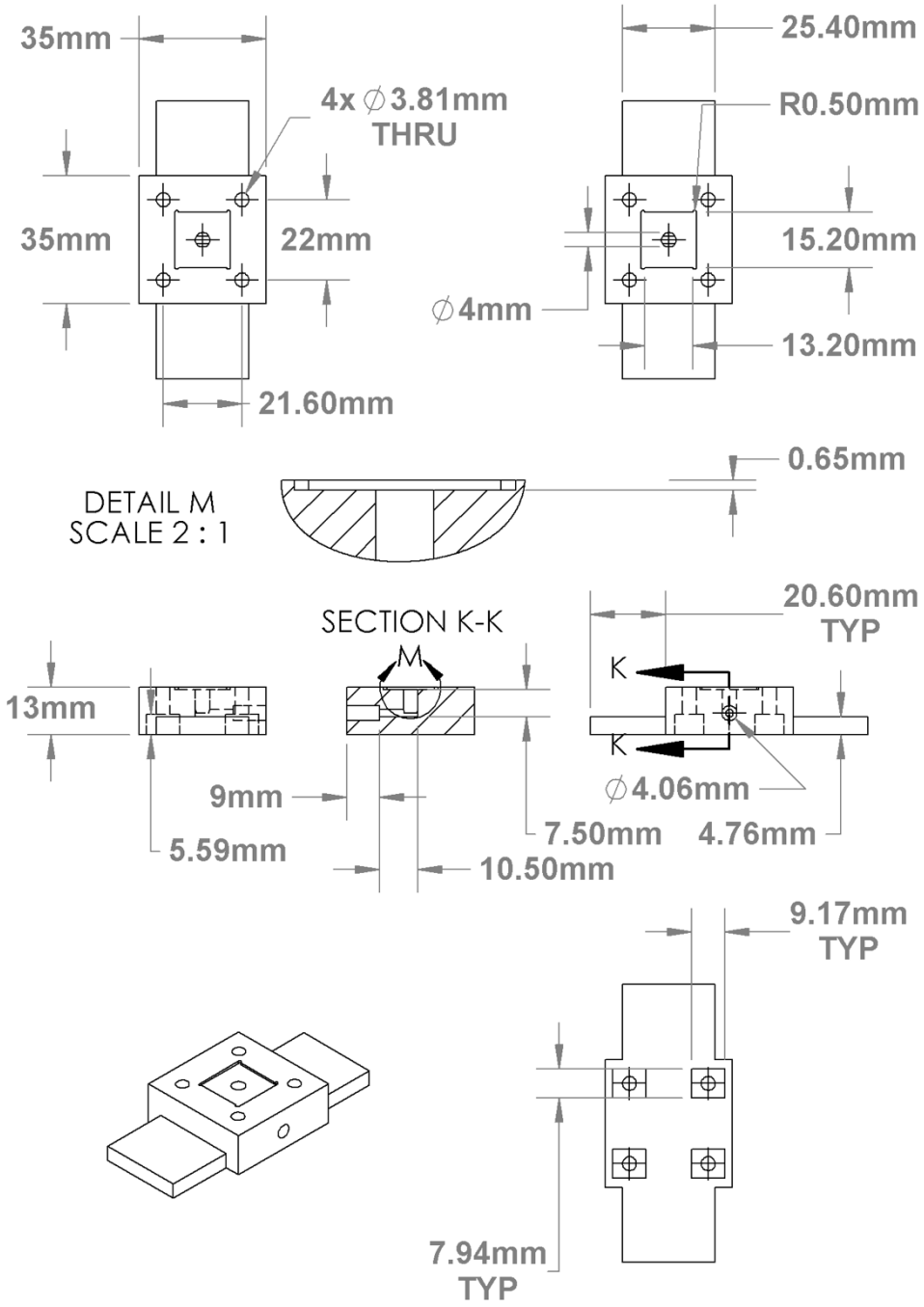

Figure C.1. Technical drawing of UHT mechanoporation device fixture set (bottom).

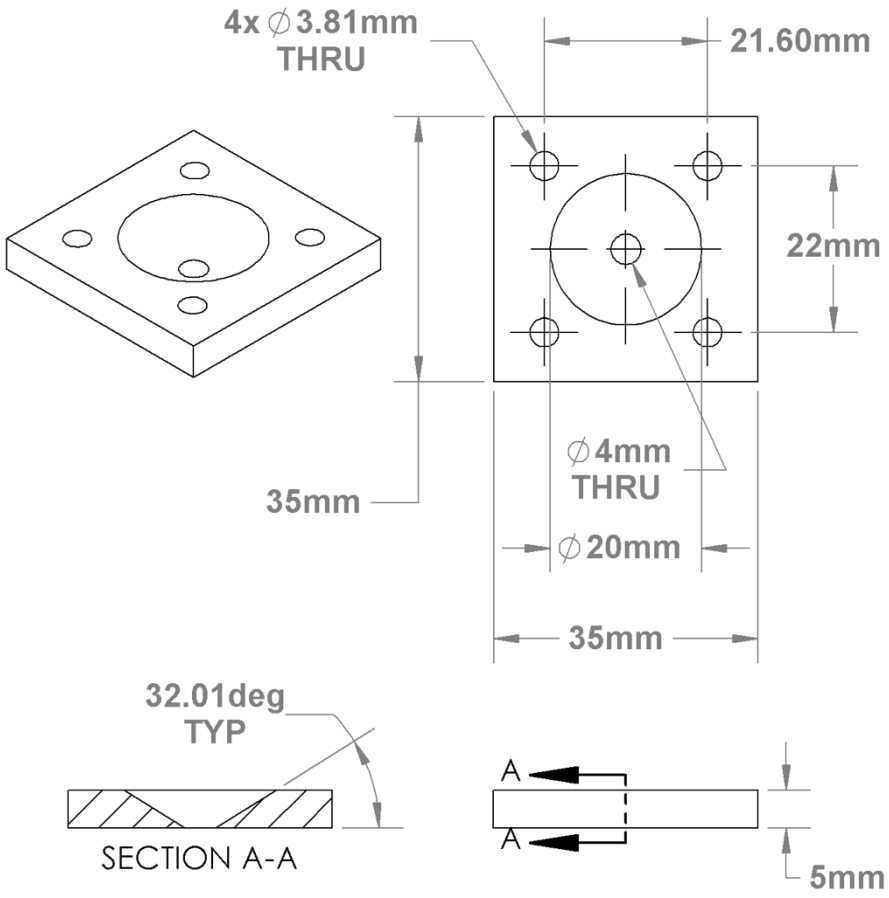

Figure C.2. Technical drawing of UHT mechanoporation device fixture set (top plate).

Appendix D

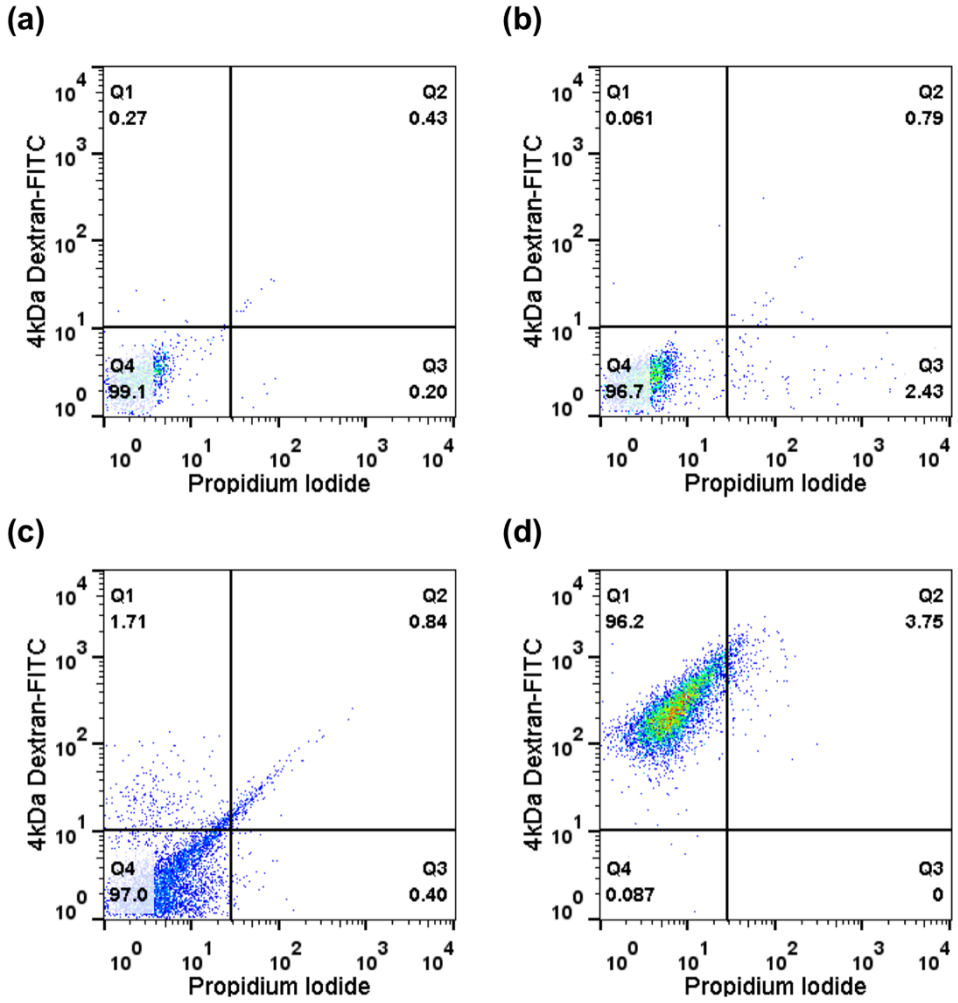

Figure D.1. Flow cytometry scatter plots of several controls completed during EL4 testing: (a) Background control of unstained EL4 cells (b) Background control EL4 cells incubated with PI without mechanoporation; (c) Negative control consisting of EL4 cells exposed to saponin for permeabilization to mimic complete poration; (d) Positive control consisting of EL4 cells exposed to saponin for permeabilization, and incubated in FITC-dextran for 30 min. Percentages of total events are shown within each quadrant on each plot.

Appendix E

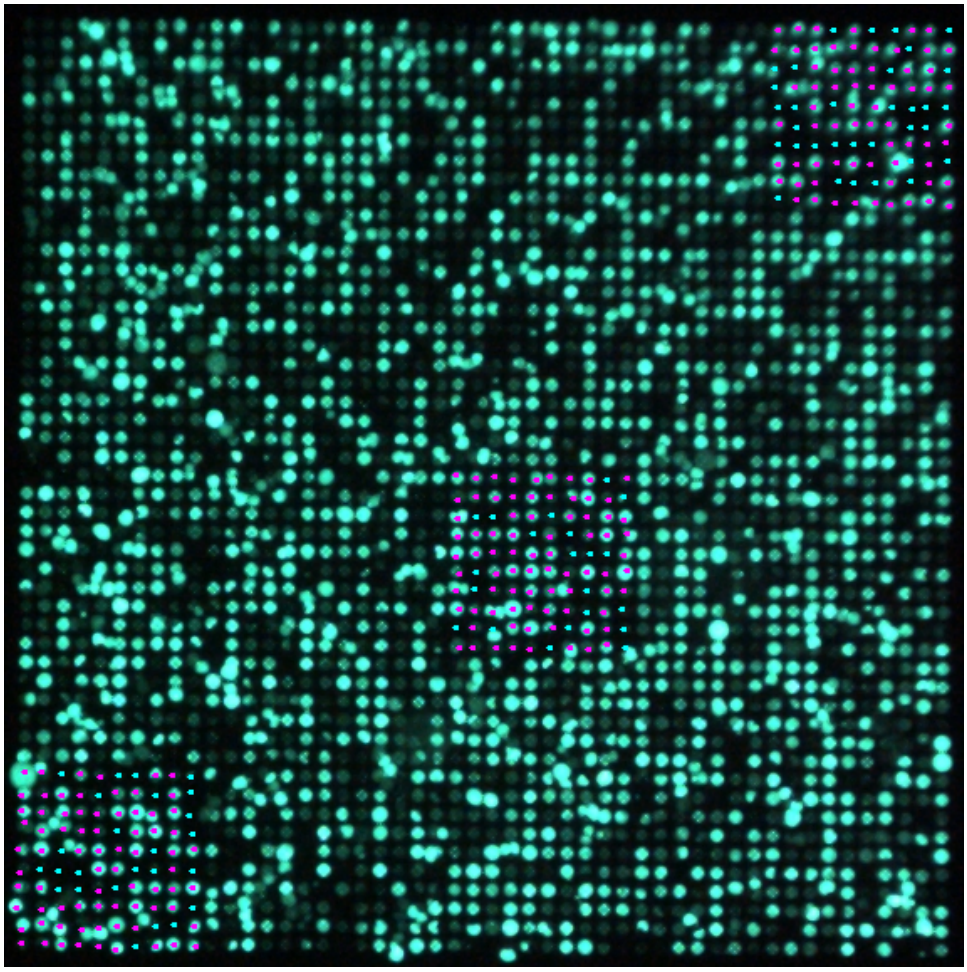

Figure E.1. Device array (1 of 4) following the capture of K562 cells at the optimum capture flow rate (40 μL/min). Capture efficiency was calculated manually by sampling 10x10 subarrays within each device array quadrant. 10x10 sections were sampled at the bottom left corner, top right corner, and mid region on ImageJ. Capture sites were then designated as occupied or unoccupied through manual marking. Pink spots represent occupied sites, while teal spots represent unoccupied sites. Markings were tallied based on color, and capture efficiencies were then calculated by dividing the total number of pink marks by the total number of markings (1200 per capture study).

Appendix F

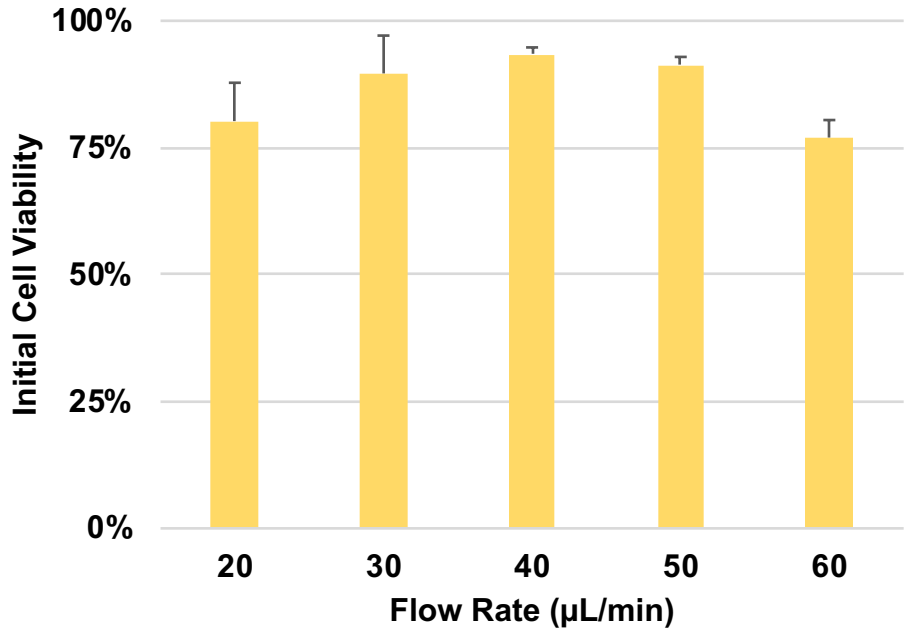

Figure F.1. Starting Jurkat cell viabilities prior to the mechanoporation optimization studies, generated through MUSE counting. Cells were stained for 5 minutes in viability dye prior to counting.

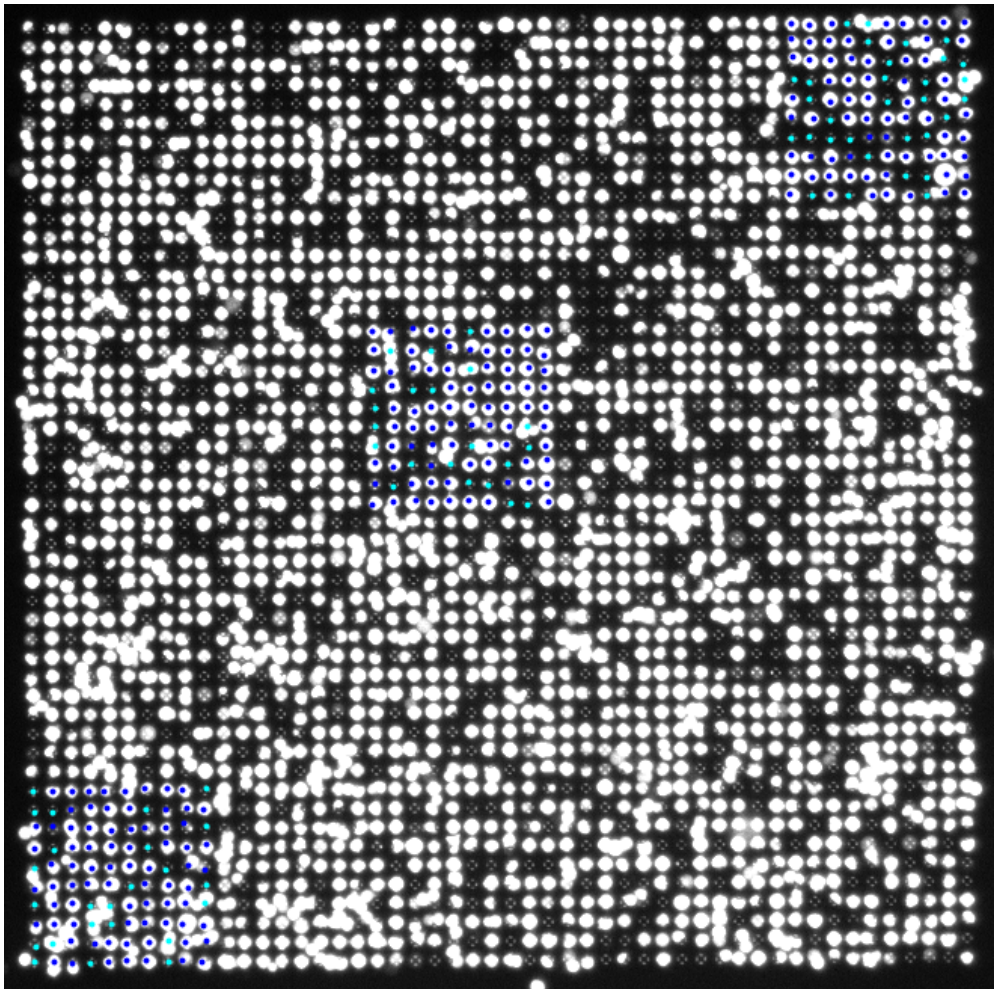

Figure F.2. Capture array micrograph for manual cell counting for capture efficiencies during Jurkat cell testing. Prior to the application of WEKA segmentation, the method outlined for calculating capture efficiency in chapter 5 was applied for the Jurkat optimization studies. As described in Appendix E, 10x10 subsections of the capture arrays were sampled and manually assessed for cell occupancy (bottom left corner, top right corner, middle region). Blue spots represent occupied capture sites, teal spots represent unoccupied capture sites. Capture efficiency was calculated by dividing the total number of blue markings (occupied site) by 1200.

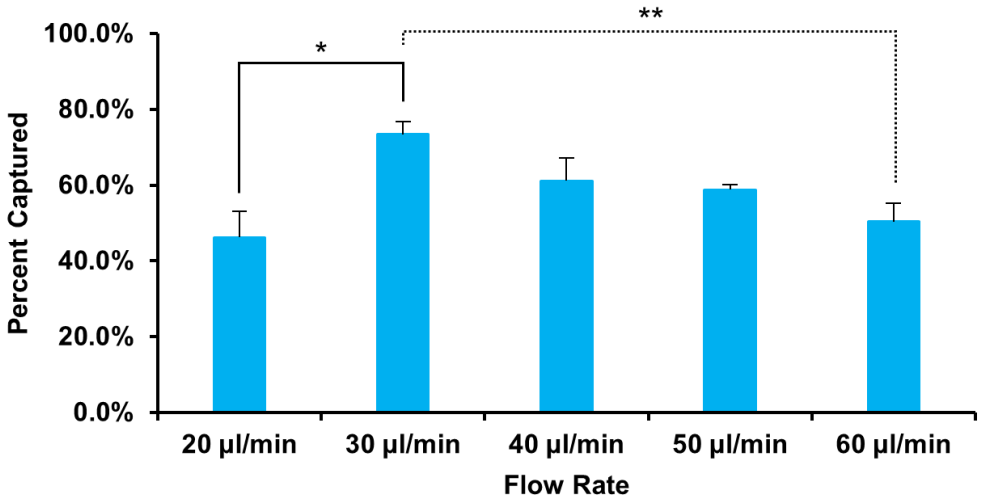

Figure F.3. Capture efficiency results from Jurkat optimization testing using the original counting method as outlined in chapter 5 (**: $p \leq 0.01$; *: $p \leq 0.05$).

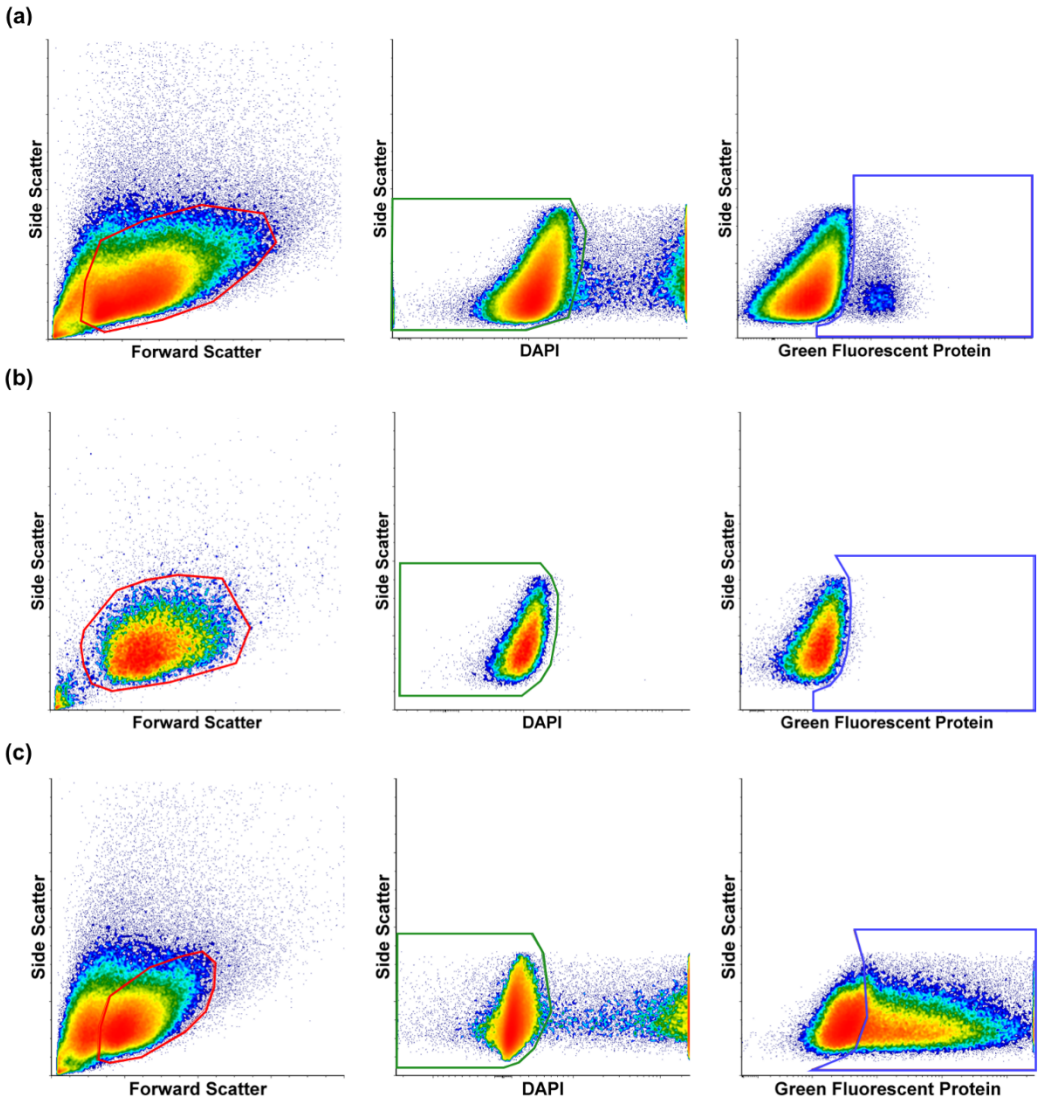

Figure F.4. Electroporation benchmark flow cytometry representative plots. (a) Passive diffusion control. Cells were incubated in 2 µg of eGFP plasmid in PBS for 1 minute before being resuspended in fresh media and incubated for 12 hours. (b) Autofluorescence control. Bare cells were incubated for 12 hours and run on the flow cytometer to account for an innate fluorescence of the Jurkat cells on the blue and green channels. (c) Electroporation sample. Jurkat cells were electroporated using the standard Lonza protocol with 2 µg of eGFP plasmid and incubated under standard culture conditions for 12 hours.

Appendix G

G.1. Calcein Blue AM Stock Concentration Preparation

- Product #: C1429 (ThermoFisher Scientific)
- Molecular Weight: 465.4128 g/mol
- Mass: 1 mg
- Stock Concentration for experiments: 4 mM & 8 mM
    1. $\frac{0.001\ g}{465.4128\ g/mol} = 2.1486e^{-6}\ mol$
    2. Volume to suspend solid stain to achieve 4 mM concentration:

       $\frac{2.1486e^{-3}\ mmol}{4\ mM} = 537.15\ \mu L$
    3. Volume to suspend solid stain to achieve 8 mM concentration:

       $\frac{2.1486e^{-3}\ mmol}{8\ mM} = 268.575\ \mu L$
- Add calculated volume of anhydrous DMSO (ThermoFisher Scientific, D12345) to solid stain
- Vortex vigorously
- Aliquot into smaller volumes
- Store at -80°C

G.2. Calcein Red Orange AM Stock Concentration Preparation

- Product #: C34851 (ThermoFisher Scientific)
- Molecular Weight: 789.55 g/mol
- Mass: 50 µg

- Stock Concentration for experiments: 1.267 mM
    1. $\frac{5e^{-5}\ g}{789.55\ g/mol} = 6.3327e^{-8}\ mol$
    2. Volume to suspend solid stain to achieve 4 mM concentration:

    $\frac{6.3327e^{-5}\ mmol}{1.267\ mM} = 50\ \mu L$
- Add calculated volume of anhydrous DMSO (ThermoFisher Scientific, D12345) to solid stain
- Vortex vigorously
- Aliquot into smaller volumes
- Store at -80°C

G.3. CellTracker Green CMFDA Dye Stock Concentration Preparation

- Product #: C2925 (ThermoFisher Scientific)
- Molecular Weight: 464.8581 g/mol
- Mass: 1 mg
- Stock Concentration for experiments: 4 mM
    1. $\frac{0.001\ g}{464.8581\ g/mol} = 2.1512e^{-6}\ mol$
    2. Volume to suspend solid stain to achieve 4 mM concentration:

    $\frac{2.1512e^{-3}\ mmol}{4\ mM} = 537.8\ \mu L$
- Add calculated volume of anhydrous DMSO (ThermoFisher Scientific, D12345) to solid stain
- Vortex vigorously

- Aliquot into smaller volumes
- Store at -80°C